# Studying Laser-Induced Spin Currents Using Ultrafast Extreme Ultraviolet Light

by

**Emrah Turgut**

B.S., Middle East Technical University, 2009

A thesis submitted to the

Faculty of the Graduate School of the

University of Colorado in partial fulfillment

of the requirements for the degree of

Doctor of Philosophy

Department of Physics and JILA

2014

This thesis entitled:
Studying Laser-Induced Spin Currents Using Ultrafast Extreme Ultraviolet Light
written by Emrah Turgut
has been approved for the Department of Physics and JILA

Prof. Margaret M. Murnane

Prof. Henry C. Kapteyn

Date

The final copy of this thesis has been examined by the signatories, and we find that both the content and the form meet acceptable presentation standards of scholarly work in the above mentioned discipline.

Emrah Turgut, (Ph.D., Physics)

Studying Laser-Induced Spin Currents Using Ultrafast Extreme Ultraviolet Light

Thesis directed by Prof. Henry C Kapteyn and Prof. Margaret M. Murnane

Next-generation magnetic-memory devices and heat-assisted magnetic-recording applications will require a better understanding of magnetic multilayers and their interactions with optical-laser pulses. In this thesis, by combining the advantages of ultrabroad-band extreme-ultraviolet light including ultrafast time resolution, element selectivity and tabletop easy access, I report three findings in the study of ultrafast magnetization dynamics in itinerant ferromagnets. First, I experimentally prove that the transverse magneto-optical Kerr response with extreme-ultraviolet light has a purely magnetic origin and that our experimental technique is an artifact-free ultrafast magnetic probe. Second, I demonstrate the first ultrafast magnetization enhancement driven by ultrafast spin currents in Ni/Ru/Fe multilayers. Third, I engineer the sample system by choosing either insulating or spin-scattering spacer layers between the Ni and Fe magnetic layers and by structural ordering. Then, I control the competition between ultrafast spin-flip scattering and superdiffusive spin-current mechanisms; either of these processes may to be the dominant mechanism in ultrafast demagnetization. Finally, I report two continuing experiments that are promising for future ultrafast magnetization studies with extreme-ultraviolet sources. These experiments are resonant-magnetic small-angle-scattering and the generation of bright circularly polarized high harmonics accompanied by a demonstration of the first x-ray magnetic circular dichroism with a tabletop system.

To my wife Esma and my daughter Zeynep Semra.

## Acknowledgements

First of all, I would like to thank my advisors, Margaret Murnane and Henry Kapteyn, for not only granting me to work in their research group but also supporting, trusting, and challenging me through out graduate school. Then, I thank to Tom Silva for being my third virtual advisor who is a great source of knowledge about magnetism and a great mind for difficult problems. Next, I thank Chan La-o-Vorakiat, the former graduate student, who built the setup and taught me how the experiment works. Moreover, it was a pleasure to work with the magnetism team in Kapteyn-Murnane group including Patrik Grychtol, Ronny Knut, and Dmitry Zusin who is taking over the project bravely. I am also very grateful to our collaborators Stefan Mathias and Martin Aeschlimann from the Univeristy of Kaiserslautern; Claus Schneider, Roman Adam, and Denis Rudolf from the Research Centre Julich; Marco Battiato and Peter Oppeneer from the Uppsala University; and Justin Shaw and Hans Nembach from National Institute of Standards and Technology where we get all wonderful samples with great generosity. For very recent excitement about circularly polarized harmonics, I thank Oren Cohen and Ofer Kfir from Technion University. I am also grateful other members of Kapteyn-Murnane group for supporting and being great friends who make the graduate school life remarkable. I must mention Daniel Adams, Matt Seaberg, and Bosheng Zhang for sharing the laser and being always helpful for any technical problem.

Finally, I am very thankful to my parents and wife Esma for their great love and support.

# Contents

**Chapter**

**1** Introduction 1

**2** Magneto-Optical Effect 10

2.1 Introduction . . . 10

2.2 Light in a Magnetic Material . . . 12

2.3 Light at an Interface . . . 15

2.4 T-MOKE of Multilayer Structures . . . 24

2.5 X-ray Magnetic Circular Dichroism . . . 29

2.6 Macroscopic and Microscopic Origin of $\epsilon_{xy}$ . . . 30

2.6.1 Macroscopic Origin of $\epsilon_{xy}$ . . . 30

2.6.2 Microscopic Origin of $\epsilon_{xy}$ . . . 32

2.7 Conclusion . . . 37

**3** Experimental Setup 38

3.1 Introduction . . . 38

3.2 High Harmonic Generation–Probe . . . 40

3.2.1 Phase Matching . . . 44

3.3 Excitation-Pump . . . 45

3.4 Other Components . . . 51

3.5 Sample Spectrometer . . . 53

3.6 Conclusion . . . 58

**4** Driving Mechanisms at Ultrafast Demagnetization 59

4.1 Introduction . . . 59

4.2 Three Temperature Model . . . 62

4.3 Landau-Lifshitz-Bloch Equation–Atomistic to Thermal Macro Spin Model . . . 63

4.4 Microscopic Models . . . 66

4.4.1 Microscopic Three Temperature Model . . . 66

4.4.2 Coherent Spin-Photon Coupling . . . 68

4.4.3 Superdiffusive Spin Currents . . . 70

4.5 Conclusion . . . 74

**5** Comparison of Electronic and Magnetic Contributions in Demagnetization 76

5.1 Previous Investigations on Magneto-Optic . . . 76

5.2 Electronic and Magnetic Contribution in XUV T-MOKE . . . 81

5.3 Conclusion . . . 90

**6** Ultrafast Magnetization Enhancement in Multilayers by Spin Currents 91

6.1 Introduction . . . 91

6.1.1 Interlayer exchange . . . 92

6.2 Multilayer fabrication and characterization . . . 92

6.3 Static Magnetic Asymmetry . . . 94

6.4 Magnetization Dynamics . . . 94

6.5 Superdiffusive spin transport . . . 97

6.6 Discussion . . . 99

6.7 Conclusion . . . 99

**7** Moderation of Ultrafast Spin Current Propagation 102

7.1 Introduction . . . 102

7.2 Samples . . . . . 102
7.3 Results . . . . . 103
7.4 Conclusion . . . . . 110

**8** Outlook: Magnetic Imaging and Circularly Polarized Harmonics 111
8.1 Introduction . . . . . 111
8.2 Magnetic Imaging . . . . . 111
8.3 Bright Circularly Polarized Harmonics . . . . . 114
8.4 Conclusion . . . . . 117

**9** Conclusion 119

**Bibliography** 121

**Appendix**

**A** Magnetic Asymmetry Expansion 129

**B** Multilayer T-MOKE Simulation and Experimental Spectrum 132

**C** Intensity vs Poynting's vector 135

# Tables

**Table**

2.1 Eight different magneto-optical geometries. The Faraday effect was the first one used to understand magnetism, and it works in transmission. Later, the Kerr effect was discovered, and in contrast it works in reflection geometry. After developing x-ray sources and charge-coupled device detectors, x-ray magnetic linear and circular dichroism became popular for element-selective magnetization probing [56]. . . . . 11

3.1 Absorbed intensity in each layer in terms of percentile of the incoming pump beam by the full-matrix method. . . . . 48

3.2 Absorbed intensity in each layer in terms of percentile of the incoming pump beam for two samples by FDTD method shown in Figures 3.6 and 3.7. . . . . 51

7.1 Calculated absorption ratios of the pump beam by each layer in terms of the percentage of the incident pump beam as calculated according to [59]. . . . . 105

# Figures

**Figure**

1.1 Two important candidates for future hard-drive technologies. At the left, heat-assisted magnetic recording uses a small amount of laser heating to increase the temperature of recording spot to switch the alignment much faster. At the right, bit-patterned media uses the idea to have grains that are very small and well-organized instead of random and unorginized grains [13, 44]. . . . . 3

1.2 The fundamental relationships between the time scales and energies of magnetic forces. The formula $t = \hbar/E$ is used in quantum mechanics to describe the uncertainty principle and relate energy to the corresponding time. . . . . 4

1.3 Adapted from [49]. Schematic timeline of ultrafast photon-electron-spin-lattice interactions after an ultrafast laser excitation. During the ultrafast excitation of the electron system by a femtosecond laser pulse, ultrafast spin-photon interaction can be a source of magnetization dynamics [93, 11, 88]. On a longer femtosecond timescale, various scattering processes between electrons, phonons, and magnons, as well as superdiffusive spin-currents [6, 65, 50, 5] determine the dynamic response of the material. The strongly excited electron system thermalizes by predominantly electron-electron scattering to a Fermi-Dirac distribution. Spin-flip, electron-electron [43, 80], electron-phonon [21, 39, 17, 69, 79, 27], and electron-magnon [69, 15] scattering processes, together with superdiffusive spin currents mediate the magnetization dynamics. Electron-phonon scattering transfers the energy from the excited electron gas to the lattice, and thermal equilibrium is typically reached on picosecond timescales. Finally, on nanosecond timescales, the material cools by thermal diffusion. The different contributions of the above-mentioned processes to the ultrafast magnetic dynamics are widely debated. elements. . . . . 6

2.1 Three commonly used geometries, transverse, polar and longitudinal, for the magneto-optical Kerr effect (MOKE). When the magnetization is perpendicular to the plane of incidence, the geometry is a transverse MOKE, which I employ in our experiments. In contrast, in the polar and longitudinal geometries, the magnetization is in the plane of incidence, but the magnetization is in $x$ and $y$ directions, respectively. 14

2.2 Interface of two magnetic media. The first medium is $j$, and the second one is $j+1$. The incoming light is p-polarized, and the angle of incidence is $\theta_j$. The amplitude of the incoming electric field is $E^k_{p,j}$, where $k$ means the direction of propagation. The reflected electric field is $E^{-k}_{p,j}$. In the second medium, the propagation direction has an angle $\theta_{j+1}$ with the normal, and the electric field is $E^k_{p,j+1}$. In the text, I explain boundary conditions and their relationship between these fields. . . . . 17

2.3 (Top) Reflected intensities of s- and p-polarized lights from semi-infinite Ni surface at the $M_{2,3}$ absorption edge of 67 eV. The minimum reflection is at a Brewster angle near 45° where the magnetic asymmetry peaks. Note that the reflectivity almost goes to zero with p-polarized incident light at the Brewster angle which makes experiment challenging. (Bottom) The neglected term in Equation 2.21. This approximation in Equation 2.21 is not valid for all angles and the error is approximately 23% at angle of incidence 45°. . . . . 20

2.4 Asymmetries vs. angle plots for two different $\epsilon_{xy}$. (Top) Asymmetry with and without the assumption as in Equation 2.21 for $\epsilon_{xy} = -0.0052 + i0.0079$. The maximum asymmetry is at 46.2°. (Bottom) Same as above with $\epsilon_{xy} = -0.007 - i0.0066$. Here, the maximum shifts to the 43°, and the shape of the curve is reversed. The amplitude of $\epsilon_{xy}$ does not affect the asymmetry; however, the asymmetry is very sensitive to the phase of $\epsilon_{xy}$. . . . . 21

2.5 Comparison of the proportionality of the asymmetry to the MO constant. I introduce an ultrafast demagnetization to the MO constant as a function of $t$ $[1 - 0.5(1 - e^{-t/0.2}e^{-t/5})]$ shown by the black curve. Then I calculate the asymmetry parameter as a function of time for different angles. Surprisingly, the transient dynamics of asymmetry at 45° do not represent the MO constant proportionally. This is not an artifact, but a pure magnetic signal. The difference $\delta$ is about 0.08, which means that the asymmetry is not linearly proportional to the MO constant. . . . . 23

2.6 Representation of the forward- and backward-propagating waves and their reflected and transmitted waves. It is essential for matrix formalism to identify coefficients at interfaces. (Left) I show four waves: two are incoming, and two are leaving the interface. I represent the leaving waves in terms of incoming waves $E_1$ and $E_2$ by using the reflection and transmission coefficients. The leaving wave in the medium $j$ is $rE_1 + \overline{t}E_2$ and the leaving one in the medium $j+1$ is $\overline{r}E_2 + tE_1$. . . . . 25

2.7 Propagation of an emw in a magnetized medium. I show how the left-side electric fields depend on the right-side of electric fields because of propagation parameters. 27

2.8 Illustration of multilayer structure. The experimental system I study is composed of N layers with the $s$ substrate at the bottom. Each interface has a dynamics matrix, and each layer has a propagation matrix. The relationship of the transmitted and reflected electric fields can be found by multiplication of all the dynamics and propagation matrices. . . . . 28

2.9 Calculations of the dielectric tensor using a classical model for cobalt at the M absorption edge. (Top) $\Gamma$ and $\omega_0$ values are fit by using the tabulated values of the refractive index [32] then plotting the fitted and tabulated values of the diagonal element of $\hat{\epsilon}$. (Bottom) Then, fitted values and Equation 2.56 are used to calculate and plot the off-diagonal element of $\hat{\epsilon}$ as a function of energy . . . . . 33

2.10 Microscopic picture of MO effect. The electronic structure is shown for a typical transition metal ferromagnet with L and M core levels and a $3d$ conduction band. The magnetic moment of the material comes from the exchange splitting of spin-up and spin-down electrons that results in an unequal occupation shown in green and blue. An incoming circularly polarized x-ray photon excites an electron from the core level to an unoccupied $3d$ state. The excitation probability for spin-up and spin-down electrons is directly dependent on the chirality of the incoming x-ray. By reversing the chirality or the direction of magnetization, an asymmetry appears in the absorption known as XMCD. This phenomenon is still true for linear polarized light because the linearly polarized light is a combination of left and right circularly polarized light. Magnetic contrast is reflected or transmitted via x-ray photons. . . 35

2.11 Experimental XMCD spectra taken from [78]. Transition metals Fe, Co and Ni have a strong contrast at the L edge via 2p→3d excitation. The magnetic moment of Gd comes from 4f electrons with a different principal quantum number that shows larger but complicated, contrast at the M edge. Because spin-orbit splitting at the $L$ edge is approximately 12 eV, the XMCD spectra for $L_2$ and $L_3$ have opposite signs and different magnitudes. . . . . 36

3.1 Experimental setup for studying element-selective ultrafast magnetization dynamics. There are four main parts in the setup: the high-harmonic-generation probe arm, the infrared pump arm, grating sample spectrometer and other components. The ultrashort laser pulse is split into two. Ninety percent of the energy is focused into a hollow waveguide filled with neon gas; this is where high-harmonic generation happens. After the waveguide, an aluminium filter blocks the fundamental beam and passes through x-rays with energies between 35 and 72 eV (cutoff energy of aluminium filter at 72 eV.) This region of spectrum is called the extreme ultraviolet (EUV). Ten percent of the rest of the beam is used as a pump to excite the magnetic sample. Both the pump and probe beams are focused by a gold-capped toroidal mirror onto the sample and the CCD camera, respectively. The sample is fabricated as a grating to disperse EUV photons spectrally on the CCD camera. There are two additional Al filters after the sample to block the pump beam and ensure that we have only EUV photons at the CCD camera. Because of dispersion, each harmonics is detected by the camera as shown in inset graph. By reversing the magnetization of the sample, we can very the reflected EUV intensity, as shown by the solid and dashed green curves for a Permalloy sample (alloy of Ni and Fe). . . . . 39

3.2 Semiclassical approach to high-harmonic generation, the three-step model. Without an electric field, the atom is neutral, and the electron is behaving as usual. When we apply an ultrashort light pulse, the electric field of the pulse is very strong and modifies the Coulomb potential significantly. Then electron tunnels in the first step. Second, the electric field accelerates the electron, giving it kinetic energy. Finally, after a half cycle through the electric field, the electron recombines with its parent atom and radiates its extra kinetic energy as a x-ray photon. . . . . 41

3.3 Example trajectories of the electron in free propagation and maximum-recombined kinetic energy. (Top) The electron has zero velocity at time zero, and it accelerates with $\frac{-eE}{m}\cos(\omega t + \phi)$. The electron displacement is shown for phase values 0, $0.1\pi$, $0.2\pi$, and $0.4\pi$. The electron can return to the atom, where the black line crosses the curves, only in a certain phase range and with a specific kinetic energy for each phase. (Bottom) The gained kinetic energy is shown as a function of phase. When the electron returns to the atom, its kinetic energy strongly depends on the phase of the electric field, which means that the time when the electron tunnels away determines its kinetic energy. The maximum-returning kinetic energy is found 3.17 $U_p$, where $U_p$ is known as the pondermotive energy. Hence, the maximum-returning energy determines the cutoff energy for high harmonics as $\hbar\omega = I_p + 3.17\ U_p$, where $I_p$ is the ionization energy of the gas. . . . . 42

3.4 Extension of the cutoff energy of HHG by using longer-wavelength driving lasers. The cutoff frequency has $\propto \lambda^2$ proportionality with the wavelength. Four spectra are shown for four different laser wavelength, i.e., 0.8, 1.3, 2, and 4 $\mu m$. The graph is taken from [60]. . . . . 44

3.5 Full matrix calculation method for absorption in multilayers. I simplify the calculations by introducing a zero-thickness vacuum layer between each layer. After finding the electric fields in these vacuum layers, the absorbed intensity is nothing but the differences in the electric fields. For example, the absorbed light in the $n^{th}$ layer turns into $\frac{1}{2}(|E_{n+}|^2 - |E_{(n+1)+}|^2 + |E_{(n+1)-}|^2 - |E_{n-}|^2)$. . . . . 48

3.6 Poynting's vector-depth profile of an example multilayer structure. The multilayer structure is consist of substrate $SiO_2$/Ta(3 nm)/Fe(4 nm)/Ru(1.7 nm)/Ni(5 nm)/$Si_3N_4$(1.2 nm)/air. One can expect an exponential type of decay in layers, but the thiccknesses of layers are much smaller than the wavelength of the pump and decay of a Poynting's vector in a multilayer is more complicated than a regular exponential decay. Total reflected, transmitted and absorbed intensities are 39.6%, 10.7% and 49.8%, respectively. Furthermore, individual absorptions are 18.5%, 12.3%, 15.5% and 3.8% for Ni, Ru, Fe and Ta layers, respectively. These ratios are in very good agreement with Table 3.1 . . . . . 50

3.7 Depth profile of Poynting's vector for a grating sample. (a) In the simulation, I use 2 $\mu m$ wide magnetic layers and 1 $\mu m$ wide $Si_3N_4$ 10 nm height gratings. (b) and (c) show the 2-dimensional profile of the Poynting's vector and the negligible effect of the grating in absorption. One can see small variations at the edges of the grating; however, the individual absorptions in layers do not change. (d) The ratios become 19.4%, 11.8%, 15.9% and 4.0% for Ni, Ru, Fe, and Ta layers, respectively. . . . . 52

3.8 Picture of experimental setup. Some essential components are shown, such as the laser system, HHG hollow capillary, toroidal mirror and chamber, vacuum systems, sample chamber, aluminium filters, power supplies, iron yoke magnet, translational delay stage, and CCD camera. . . . . 54

3.9 Illustration of iron magnet yoke with sample holder. $N$ is the number of wire turns, $I$ is the current on the wire, $l_{gap}$ is the width of the gap, $L$ is the total length of the iron yoke, $A_{gap}$ and $A_{core}$ are the total area of the gap and the core respectively, and $\mu_{core}$ is the permeability of the iron core. . . . . 55

3.10 Illustration and AFM image of a grating sample. There are two types of samples we use. One type is a magnetic sample patterned as a grating on a substrate. In the second type, magnetic multilayers are patterned as thin films, and a 10-nm-thick $Si_3N_4$ grating is placed on magnetic films. Two designs give diffraction orders and work as a spectrometer. The grating spacing is 1 $\mu m$ and is limited by an optical lithography technique. To calculate the diffraction formula, I define two reflection coefficients, $r_1$ and $r_2$. The reflection angle $\beta$ defines the constructive and destructive interferences on the camera depending on the wavelength of the incident EUV photon. 56

3.11 Calculation of Equation 3.15 for $45^{th} - 15^{th}$ harmonics. I use $P = 0 - 512$, $p = 26$ $\mu m$, $d = 1$ $\mu m$, $r_1 = r_2 = 0.01$, and $h = 10$ $nm$ for the calculations. This is the typical experimental spectrum extracted by the CCD camera except the peaks are not sharp because of the defects at the grating edges. . . . . 57

4.1 The first three experimental reports on ultrafast magnetization dynamics. (a) Spin-polarized photoelectrons from Fe were detected after two ultrashort optical pulses of 20 ns and 30 ps. While the 20 ns pulse caused a decrease in magnetic moment, the 30 ps pulse was too fast to capture any demagnetization. This results suggests that the spin-lattice relaxation is much longer than 30 ps [85]. (b) The second, maybe more famous, example is from 1996 [9]. By using magneto-optical Kerr effect, the researches were able to demagnetize the Ni film in 1 ps. Here electron-electron and electron-phonon scattering initiated demagnetization much sooner than would spin-lattice relaxation. (c) By looking at long- and short-timescale magnetization dynamics in Ni by employing photoelectrons, this study was able to explain the observations in (a) and (b). In the first ps, demagnetization starts with Stoner-like excitations and continues by creating of transversal spin waves, shown by (d) in detail. 61

4.2 Phenomenological three-temperature model. The electron, spin and lattice are modeled as three heat reservoirs. Three of them have temperatures, heat capacities, and interactions between one another represented by coupling constants. An ultrashort optical pulse excites and heats the electron system rapidly. Then the three reservoirs interact and equilibrate their temperatures. From observations of the transient reflectivity and magnetization dynamics, the electron and the spin temperature can be extracted experimentally: then the rest of the unknowns can be calculated. . . . . 64

4.3 Illustration of the Landau-Lifshitz-Bloch equation with three terms. The red force along the dashed line keeps the magnetic moment precessing around $H_{eff}$. The blue force applies a transversal damping to align the magnetic moment along $H_{eff}$ without changing the magnitude of the moment. The green force is the source of demagnetization by longitudinal damping. . . . . 65

4.4 llustration of the Elliot-Yafet scattering mechanism. An electron flips its spin by creating or absorbing a phonon with $\alpha_{EY}$ probability. . . . . 67

4.5 Coherent spin-photon interaction [11]. First, the photons interact with electrons and spins because of relativistic quantum electrodynamics. These interactions initiate the demagnetization process. Then, thermalization between spins and electron occurs within 100 fs. Finally, the spins and electrons couple with the lattice and lose the magnetization further by radiating THz photons. The figure is taken from [11]. . . . 69

4.6 First observation of direct spin transport taken from [48]. Co/Pt magnetic multilayers are sandwiched with insulating NiO and conducting Ru layers. Ultrafast magnetization dynamics are probed with MOKE for parallel and antiparallel alignments. While the dynamics are the same for the insulating NiO layer; surprisingly, the Ru layer allows direct spin transport from one layer to another, resulting in more demagnetization for the antiparallel layers (black curves) then the parallel arrangement (red curves). . . . . 71

4.7 Density of states of Ni and lifetimes and velocities of electrons above the Fermi level taken from [97]. Above the Fermi level, the spin-down band has more *d*-like bands, resulting in smaller velocities and lifetimes for spin-down electrons. However, this is opposite for spin-up electrons because of s- or p-type bands above the Fermi level. These differences in lifetimes and velocities give rise to spin-dependent transport, or spin currents. . . . . 73

5.1 Previously done MO artifact investigations [38, 63, 34, 41]. a) The extracted two signal from the ellipticity and the polarization rotation show very different dynamics within the first 400 fs. b) and c) The second harmonic generation can also probe magnetization, but employing two pump pulses show very different dynamics even changing signs. d) Temperature dependent magnetization dynamics is probed by the optical setup and the initial dynamics do not show any correlation which again indicate optical artifacts at early time scales. e) and f) The optical artifact is investigated by modifying the chirp of the pulses, which results in different magnetization dynamics. g) Dependence of ultrafast demagnetization to the crystalline orientation is showed which is not originating from magnetization. . . . . 78

5.2 Illustration of the dichroic bleaching. (a) I assume that there is one possible excitation channel in the spin-down band and (b) the pump pulse excites only from the minority band and none from the majority band. (c) The modification in the real and imaginary parts of the off-diagonal elements of the dielectric tensor is shown while absence of demagnetization [41]. . . . . 80

5.3 Transient reflectivity measurements of Ni film with s-polarized XUV light. White diamonds show the lattice dynamics used off-resonance photons and the lattice dynamics are relatively slow with respect to the electrons. However, on-resonance photons shown by the green shapes allow us to probe the electronic dynamics within the first ps that could give an artifact to the magnetic asymmetry. However, the amplitude of this electronic response is 0.2% which is two orders of magnitude smaller than the real magnetic response. . . . . 83

5.4 Theoretical calculation of the relationship between s-polarized reflectivity and the refractive index. Any 0.2% change in the s-polarized reflectivity can be result from 0.1% change in the imaginary part of $n$ or very large change in the real part of the $n$. We use $\Delta\beta$ which is more related to the reflectivity. . . . . 84

5.5 Magnetization dynamics at four-different pump fluences and non-magnetic artifact in the magnetic asymmetry. The green, orange, blue, and red curves show the ultrafast demagnetization dynamics for 0.3, 0.6, 1.6, and 2.4 mJ/cm$^2$ pump fluences. We also performed the magnetic asymmetry measurements with s-polarized XUV light which gives zero signal shown by the black squares. By using the extracted change in the refractive index from the 5.3, we find the contribution in the magnetic asymmetry. The purple curve shows this negligible optical contribution in the magnetization dynamics. . . . . 85

5.6 Theoretical calculations of the reflected s-polarized and magnetic asymmetry in case of phenomenological change in the refractive index. a) Iso-reflectivity curves for angle of incidences 41$^o$ and 45$^o$ as a function of $\delta$ and $\beta$. b) An artificial asymmetry dynamics for variation of $\delta$ and $\beta$ as in (a) without changing $\epsilon_{xy}$. The comment claims that remaining constant of the s-polarized reflectivity does necessarily not mean that the electronic artifact is negligible at 45$^o$. However, this claim can be disproved by measuring magnetization dynamics at a different angle. c) Similar calculation as in (b), but for a 10-nm and 1000-nm thich Ni samples. The asymmetry behavior changes quantitatively, nonetheless the green and blue curves still qualitatively differ a lot. . . . . 87

5.7 Magnetization dynamics of Ni at an agnle of incidence 41$^o$ with different pump fluences. a) Normalized magnetization dynamics show an exponential decay after an ultrashort laser excitation. b) Maximum demagnetization is proportional to the pump fluence independent of the angle of incidence. This disproves the comment by Vodungbo et al. [87] and our conclusion of the original paper remains unaffected [47] [82]. . . . . 88

6.1 Representation off spin waves around an atom and between magnetic layers, taken from [78]. a) Polarized spin waves in an atom oscillate in space and decay at relatively long distances. This long-distance interaction explains the direct-exchange magnetization in $4f$ metals. b) This wave nature of spins also occurs in magnetic layers. For instance, thickness-varied Ru layer is sandwiched by NiFe magnetic layers and the orientation of NiFe layers measured. Hence, the relative alignment and the strength of the coupling of magnetic layers show a decaying oscillation trend as a function of thickness of Ru layer. . . . . 93

6.2 Static-magnetization profile of Fe/Ru/Ni multilayer. (Top) A superconducting quantum interference device (SQUID) magnetometer used to measure the total magnetic moment and the hysteresis of the sample. At the saturation magnetic field two layers are aligned parallel, while they are antiparallel around 20 mT magnetic field. (Bottom) These two alignments are also observed with our T-MOKE setup by magnetic asymmetry. When a strong or weak magnetic field is applied, two layers are parallel or antiparallel, shown by the violet and the orange curves, respectively. The magnetic asymmetry has opposite peaks for the parallel alignment which might mislead to antiparallel alignment. However, the magneto-optical signal of multilayer structure could be very complicated, and give unexpected static asymmetries. . . . . 95

6.3 Ultrafast magnetization curves of Ni and Fe as a function of pump-probe time delay. Surprisingly, Fe magnetization increases while Ni demagnetizes for the parallel alignment (top). On the other hand, Fe magnetization dynamic differs quite a bit when the layers are antiparallel, while Ni demagnetize as in the top. This distinct difference is a strong sign of a spin transport from the top-Ni layer into the bottom-Fe layer. . . . . 96

6.4 Calculation of spin currents between Ni and Fe layer for our experimental parameters, but neglecting a spacer layer. These magnetization dynamics agree very well with the experimental measurements. These effective 'net' spin currents result from the asymmetry in spin dependent-lifetimes in Ni as shown in Figure 4.7 . . . . . 98

6.5 Ultrafast magnetization dynamics of Fe/Ru/Ni multilayer in the case of high-pump fluence. In contrast to Figure 6.3, Fe demagnetizes after the ultrashort laser pulse. This indicates that the spin currents are not dominant anymore and the spin-flip scattering mechanisms take place more. . . . . 100

7.1 Temporal evolution of the magnetic asymmetry and the reflected XUV spectrum of a substrate/Ta(3 nm)/Fe(4 nm)/Ru(1.7 nm)/Ni(5 nm)/$Si_3N_4$(6 nm) multilayer. The solid and dashed green curves represent the reflected XUV intensities upon reversal of the external magnetic field. The light blue curve denotes the derived static (no pump) magnetic asymmetry, which is maximum at the $M_{2,3}$ absorption edges of Fe (red bar) and Ni (blue bar) and linearly proportional to the magnetization. The pink and the brown curves show the magnetic asymmetry after excitation by a laser pump pulse at a pump-probe delay of +100 fs and +700 fs, respectively. . . . . 104

7.2 Layer-selective magnetization dynamics in substrate/Ta(3 nm)/Fe(4 nm)/X/Ni(5 nm)/$Si_3N_4$(6 nm) multilayers with different spacer layers. In a), clear enhancement in the magnetization of the Fe layer is observed in the presence of good spin transport across the 1.7 nm Ru spacer layer. In b) and c), no enhancement of the magnetization of the Fe layer is observed when spin scattering spacer layers of Ta (2 nm) and W (2 nm) are used. In d), spin currents are fully suppressed by inserting a 3 nm insulating $Si_3N_4$ layer. . . . . 106

7.3 Magnetization dynamics of a substrate/Ta(3 nm)/Ni(5 nm)/Ru(1.7 nm)/Fe(4 nm)/$Si_3N_4$(6 nm) multilayer. Parallel and antiparallel alignments of the Ni and Fe layers are respectively obtained by using a strong (±40 mT) and weak (±10 mT) external magnetic field. The observed demagnetization in the Fe layer does not change as a function of the relative magnetic orientation. In contrast, demagnetization in the Ni layer increases from $\approx 38 \pm 1\%$ to $56 \pm 4\%$ for antiparallel orientation, because spin currents from the top (Fe) layer to the bottom (Ni) layer favor spin-flip scattering processes. . . . . 109

8.1 One of the earliest example of Fourier transform holography imaging of magnetic domains, taken from [24]. . . . . 113

8.2 Small angle scattering results of FeGd magnetic multilayers from HHG and a synchrotron source. The left image is recorded by our in-home HHG source with a monochrometer for 55.5 eV at M edge of Fe. The right image is obtained by DESY synchrotron facility at 713 eV L edge of Fe. While we have only the first order at the left, we are able to see the first and the third order rings because of high photon flux, although the exposure time is 1200 times less. . . . . 114

8.3 Sketch of circularly polarized harmonic generation. We combine 800 nm and 400 nm of wavelength ultrashort laser pulses with opposite hellicities. The resulting electric field looks like a flower-leaf. This electric field profile is very efficient for recombination process during HHG. . . . . 116

8.4 The raw spectrum of circularly polarized harmonics and transmitted intensities of high harmonics after a 50-nm-thick Ni foil. (top) Generated circularly polarized high-harmonics from Ar, Ne and He gases. We can cover the entire absorption edges of Fe, Co and Ni to study XMCD. (bottom) The magnetization of the foil is flipped from the up to the down in order to create a magnetic dichroic signal shown by the red and blue curves. The normalized difference of these intensities are plotted at the lower graph. The $3n$ harmonics are suppressed and the adjacent harmonics are oppositely polarized as explained in the text. Hence, the magnetic asymmetry has a sequence of '0', '+', '–'. . . . . 118

B.1 Comparison between nine experimental spectrum and theoretical calculation of magnetic asymmetries as a function of energy. Agreement between the calculation and experiment is not great because of lack information about refractive indices. . . . . 134

# Chapter 1

# Introduction

Physical forces in nature must be understood before we control them. By controlling and using these forces, people have already created advanced civilizations remarkably. For instance, our understanding of the buoyancy force has enabled us to build ships and explore the world. Learning about the gravitational force has allowed us to build space rockets and put satellites in orbit around the world. Most of the time, people measure the effects of forces to learn about them. For example, Newton measured the time required for an apple to fall, and Galileo observed the period of an object that moves through space or orbits a star. In the past, people were amazed by the vastness of the universe and by looking up in the sky. However, today we are amazed more by the smallness of atoms, or even quarks in our quest to understand nature.

As we are interested in small things, the time resolution required to capture the physics also decreases significantly. For instance, while a slow chemical reaction requires less than a picosecond time resolution, one has to have an atto- even zeptosecond time resolution for nuclear reactions. Consequently, revealing the physical mechanisms responsible for chemical reactions is very common with femtosecond ultrafast lasers, but nobody has been able to probe nuclear reactions in realtime yet.

Indeed, magnetism is another interesting phenomenon that played an important role today's technology as well as in the early advancement of civilization. For instance, the Chinese invented the compass to find their way in 634 BC. Today we can generate hundreds of thousands of terawatt-hours of electrical energy and save all the information gathered by humankind into a hard drive with

the help of magnetism. Of course, it is not possible to mention all the people and accomplishments leading to today's advancing, but I will discuss some recent inventions used to store information in computers.

In 1988, Albert Fert et al. and Peter Grünberg et al. independently discovered the giant magneto-resistance (GMR), which is the spin-dependent scattering of electrons during the flow of a current [78]. The idea behind GMR effect actually was simple, but, in terms of technical implementation, it was extremely challenging. The striking question was that when two magnetic layers carry a current, how does the resistance of the system depend on the alignment of magnetic layers? At room temperature the researchers could not see any effect, but when the system was cooled, they saw a giant change in the resistance as the alignment of layers reversed from parallel to antiparallel. The challenge they faced with was manufacturing the magnetic multilayer, because the multilayer had an approximately one-nm-thick layers. Today, the GMR effect is widely used in hard-drive storage technologies that have created a $50 billion industry [78].

More recently, Slonczewski et al. and Berger et al. proposed an angular-momentum transport between ferromagnets via a spin-polarized electron current [78]. The idea was to excite spin waves in one ferromagnet to switch the other one. This proposal was experimentally demonstrated as well. It attracted much attention because it included some applications in magnetic random-access memory and some fundamental scientific questions about the exchange couplings and interfaces of ferromagnets [78].

Today, both engineers of storage-device technologies and scientists in magnetism research focus on understanding the fundamental limits in the speed of magnetization dynamics and the amount of information stored in a certain area. Two candidates are promising for faster and higher capacity hard-drives in the future, as shown in Figure 1.1. One of them is a heat-assisted magnetic recording (HAMR). The fast-heating effect of a laser pulse facilitates in the HAMR to switch a bit faster [13]. As shown in the left of Figure 1.1 in the HAMR, the laser pulse heats the bit close to the Curie temperature where the magnetization can switch its sign much faster. At this point, magneto-optical effects become very important for understanding and controling the interaction

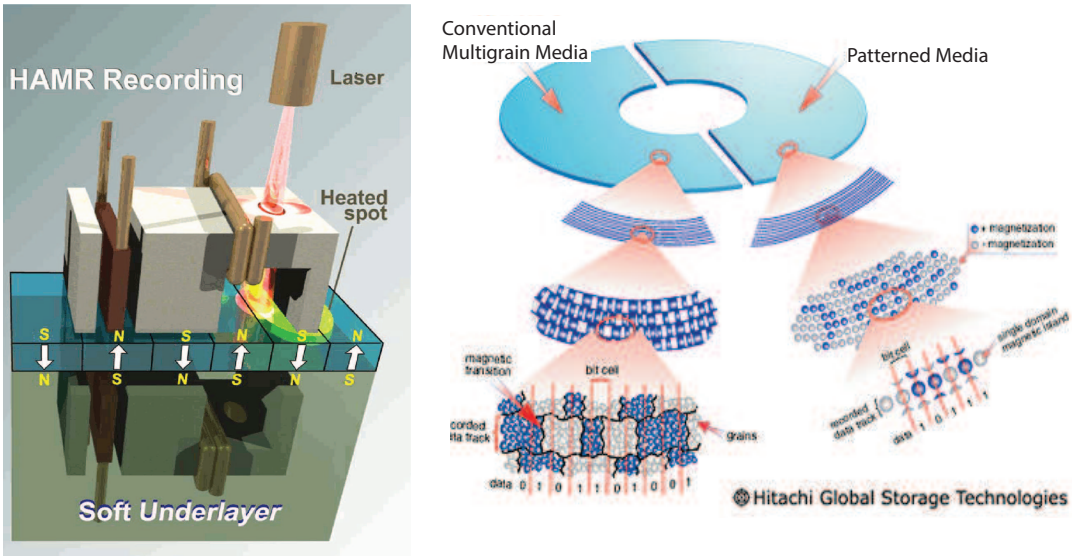


Figure 1.1: Two important candidates for future hard-drive technologies. At the left, heat-assisted magnetic recording uses a small amount of laser heating to increase the temperature of recording spot to switch the alignment much faster. At the right, bit-patterned media uses the idea to have grains that are very small and well-organized instead of random and unorginized grains [13, 44].

between a laser pulse and a magnetic material. Furthermore, as shown in the right of Figure 1.1, the second candidate is bit-patterned media [44]. A current hard drive has random and unorganized grains that create bits to store 1's or 0's. These grains can have very different sizes and shapes, which makes writing and reading processes slow and complicated. The goal with a new design is to create very uniform and organized grains, or bits, to make reading and writing processes much more efficient. Clearly, future technologies will require an understanding of the magnetization dynamics at ultrafast time scales and resolving of the magnetization properties of few-nm size magnetic grains [78].

Scientists are interested not only in developing hard-drives but also in the fundamental physics of magnetic materials and their interactions on ultrafast time scales. In these interactions, the physical forces are directly related to their time scales and energies that requires to overcome the force [76]. The uncertainty principle in quantum mechanics illustrates this relationship between time and energy on large-range of magnetic interactions, as shown in Figure 1.2. When one studies the magnetic anisotropy interaction that is used in today's hard drives, the magnetization can

switch on time scales longer than 1 ns. However, the spin-orbit and exchange interactions that require larger energy are more promising for faster dynamics [78].

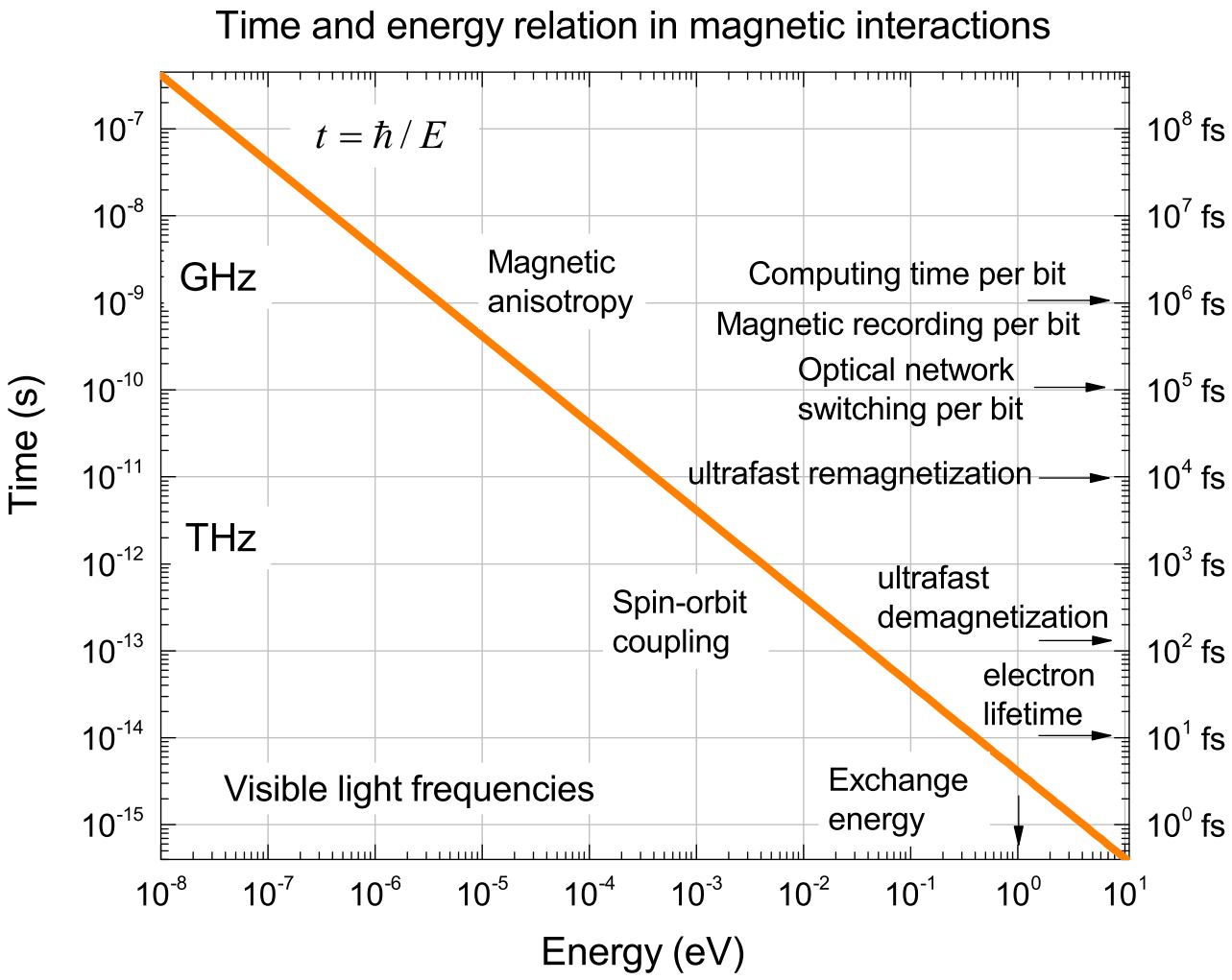


Figure 1.2: The fundamental relationships between the time scales and energies of magnetic forces. The formula $t = \hbar/E$ is used in quantum mechanics to describe the uncertainty principle and relate energy to the corresponding time.

At this point, ultrafast x-ray sources are playing a crucial role in probing magnetic interactions. Ultrafast x-ray sources offers femtosecond-temporal resolution and nanometer-spatial resolution. High temporal and spatial resolution naturally exist in the short pulse duration and

wavelength of x-rays. In last two decades, ultrafast x-rays sources have flourished. Their pulse duration has been getting shorter and shorter and is now down to attoseconds. The size of these sources has been getting smaller and smaller until now they fit on an optical table. X-ray probes also offer element specificity in magnetization-dynamics experiments. In the case of optical probing of magnetic multilayers, the magnetic signal includes the total dynamics, which does not tell anything about a specific layer or a component of the structure. However, the use of broad-band x-rays allows to tune the energy of the x-rays to the absorption edge of the elements and probe a specific element or layer to reveal the complex interactions in the system [78].

We can probe and understand the fast dynamics and small nano-magnets with ultrafast x-ray sources, but if the writing and reading processes in hard drives stay the same, there is no hope for a faster hard-drive. This fundamental challenge to bring new approach to the writing and reading processes has been studied since the first observation of ultrafast demagnetization [9, 78], called as femtomagnetism. The femtomagnetism denotes probing and manipulating magnetization of a material with ultrafast (few femtosecond) laser pulses. This phenomena has also been called all-optical switching which means using only optical pulses to control magnetization [76, 77].

Femtomagnetism has become a challenging research topic of increasing interest because of its importance for uncovering new fundamental science and for technological applications. Typically, experiments that study femtomagnetism are carried out in a pump-probe geometry. An intense femtosecond laser pulse first excites a magnetic system, and the resulting ultrafast spin dynamics in the material are then probed magneto-optically or by spin-resolved photoemission.

The dynamical response of a magnetic material to the laser excitation is governed by nonequilibrium interactions between photons, electrons, spins, and phonons (see Figure 1.3). Despite nearly two decades of research, the fundamental microscopic processes involved in femtomagnetism are not well understood and are still a topic of intense debate [36, 21, 39, 43, 93, 11, 6, 69, 81, 53, 1]. One of the key challenges is the careful disentangle the various dynamical processes shown in Figure 1.3. The goal is to establish how each process contributes to the behavior of a complex magnetic system far from equilibrium.

This quest demands the development of new experimental capabilities. For example, the investigation of coherent magnetization dynamics in the time domain requires extremely high time resolution ( 20 fs), while the influence of exchange coupling on magnetization dynamics requires element specificity. Finally, to capture superdiffusive spin transport in magnetic multilayer stacks, we require ultrafast element-specific, layer-selective probes of the magnetization state [46, 47, 65, 82, 83, 49].

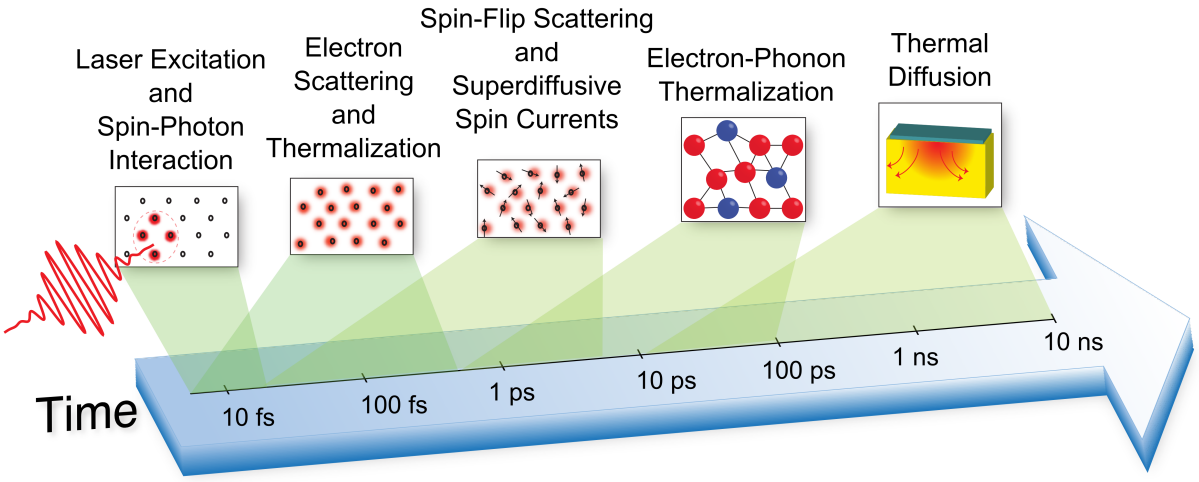


Figure 1.3: Adapted from [49]. Schematic timeline of ultrafast photon-electron-spin-lattice interactions after an ultrafast laser excitation. During the ultrafast excitation of the electron system by a femtosecond laser pulse, ultrafast spin-photon interaction can be a source of magnetization dynamics [93, 11, 88]. On a longer femtosecond timescale, various scattering processes between electrons, phonons, and magnons, as well as superdiffusive spin-currents [6, 65, 50, 5] determine the dynamic response of the material. The strongly excited electron system thermalizes by predominantly electron-electron scattering to a Fermi-Dirac distribution. Spin-flip, electron-electron [43, 80], electron-phonon [21, 39, 17, 69, 79, 27], and electron-magnon [69, 15] scattering processes, together with superdiffusive spin currents mediate the magnetization dynamics. Electron-phonon scattering transfers the energy from the excited electron gas to the lattice, and thermal equilibrium is typically reached on picosecond timescales. Finally, on nanosecond timescales, the material cools by thermal diffusion. The different contributions of the above-mentioned processes to the ultrafast magnetic dynamics are widely debated. elements.

The ideal experimental technique therefore combines sensitivity to the magnetization state with femtosecond-to-attosecond time resolution. It should also be able to distinguish the signal

from different elements in an alloy or multilayer system and image with nanometer spatial resolution. This is a challenging task, but one that can be achieved by the use of a femtosecond slicing technique [62, 75], the newly developed large-scale x-ray free-electron lasers (XFELs) [58, 90], and tabletop-scale high-harmonic-generation (HHG) light sources [46, 47, 65, 82, 49, 83]. Comparing the magnetic dynamics probed by HHG, femtosecond slicing sources, or XFELs, it is becoming clear that all of these techniques are complementary and have unique advantages. Synchrotrons and XFELs can probe dynamics at the higher-energy L-shell absorption edges, allowing spin and orbital contributions to be extracted and enabling higher spatial resolution imaging. Furthermore, high harmonic probes at the M absorption edges have the advantage of probing the magnetic state of multiple elements simultaneously, allowing the fastest coupled dynamics to be uncovered with very high precision. This source is also compact and accessible.

In this thesis, by using high-harmonics generation (HHG) I report on a experimental study of ultrafast magnetization dynamics in magnetic multilayers. I employ an element-selective ultrafast-extreme-ultraviolet light. In our experimental setup, I use HHG to produce extreme-ultraviolet photons that cover the entire M-edge of Fe, Co, and Ni. In magnetic multilayers, we convert element specificity into layer specificity and observe some important characteristics of ultrafast magnetization dynamics. These include:

- Proving that probing ultrafast magnetization dynamics with HHG is a perfect tool on a tabletop, producing no electronic artifact.
- Probing the exchange interaction between Fe and Ni in Ni-Fe alloys and controlling this exchange energy by diluting the alloys via Cu.
- Demonstrating for the first time of ultrafast magnetization enhancement in magnetic multilayers with superdiffusive spin currents.
- Controlling the contributions of spin-flip scattering and superdiffusive spin currents during ultrafast magnetization dynamics in magnetic multilayers.

- Generating for the first time bright circularly polarized high-harmonics on a tabletop and demonstrating x-ray magnetic circular dichroism on a tabletop.

- Magnetic resonant-imaging by coherent diffraction imaging and small-angle scattering.

This thesis describes these results in detail as follows,

*Chapter 2*: I discuss and give background on magneto-optical effects in the extreme ultraviolet range, and extend these theoretical descriptions into magnetic multilayers for the transverse magneto-optical Kerr effect. I also discuss the physical origin of the magneto-optical effect by linking it to the dielectric tensor.

*Chapter 3*: I give a detailed explanation of our experimental setup. First, I provide background information on HHG that allows us to use x-rays in time-resolved dynamics. Second, I explain how the excitation that is an absorption of our pump pulse happens in magnetic multilayers. Third, I describe other crucial parts in the experiment, such as the camera, the toroidal mirror, and the iron-yoke magnet.

*Chapter 4*: I review the physical mechanisms responsible for ultrafast demagnetization following an ultrafast excitation. There are five mechanisms mentioned: (1) The three-temperature model, (2) the Landau-Lifshitz-Bloch equation, (3) microscopic three-temperature model, (4) coherent spin-photon coupling, (5) superdiffusive spin currents.

*Chapter 5*: I discuss optical artifacts in magneto-optical effects. First, I review past studies on optical pump-probe experiments. Then, I experimentally investigate our magneto-optical response from the HHG-transverse magneto-optical Kerr effect if there is any nonmagnetic artifacts. I reach a conclusion that our technique is artifact free.

*Chapter 6*: I discuss the demonstration for the first of ultrafast magnetization enhancement driven by superdiffusive spin currents in Ni/Ru/Fe magnetic multilayers following an ultrafast laser-pulse excitation.

*Chapter 7*: I further investigate the characteristics of ultrafast spin currents by engineering our samples. Instead of a conducting Ru layer, I use an insulating $Si_3N_4$ and a spin-scattering Ta

and W spacer layer to suppress the spin currents. Then, I reverse the Fe and Ni magnetic layers structurally and observe that spin-flip-scattering mechanisms and ultrafast spin currents contribute approximately equal in demagnetization processes.

*Chapter 8*: I report very recent and continuing experiments on circularly polarized harmonics and magnetic imaging. X-ray magnetic circular dichroism on a tabletop is demonstrated for the first time by using very bright circularly polarized extreme ultraviolet photons produced by HHG. I also show small-angle-scattering imaging from FeGd magnetic samples by using resonant photons at the Fe M-edge to learn more about magnetic-domain structures.

I conclude the thesis in the last chapter.

# Chapter 2

# Magneto-Optical Effect

## 2.1 Introduction

Magnetization has been a curiosity for centuries to humankind, and magneto-optical effects have been used to investigate it since $18^{th}$ century. Magneto-optic effects comprise that any type of interaction between an electromagnetic wave and a magnetized material that changes the properties of the material. Magneto-optics is such a useful effect that one can probe the magnetic properties of materials and, more importantly, manipulate magnetization with light. Because of this usefulness, magneto-optics have been explored in many different geometries, eight of which are shown with their properties in Table 2.1 [56].

In this chapter, I formulate the responses of a magnetized material to optical radiation via Maxwell's equations and introduce the different type of magneto-optical effects for different geometries. First, I start with light propagation in a magnetized material and show how the effects depend on the polarization of the light and the direction of magnetization. Second, I investigate reflection and transmission phenomena at the interface of a magnetic material. Finally, which is more related to scope of this thesis, I discuss the transverse magneto-optical Kerr effect in magnetic multilayers which is more related to the scope of this thesis.

Table 2.1: Eight different magneto-optical geometries. The Faraday effect was the first one used to understand magnetism, and it works in transmission. Later, the Kerr effect was discovered, and in contrast it works in reflection geometry. After developing x-ray sources and charge-coupled device detectors, x-ray magnetic linear and circular dichroism became popular for element-selective magnetization probing [56].

| Magneto-optical Effect | Geometry | Detection | Polarization of light | Order of Effect |
|---|---|---|---|---|
| **Transverse MOKE** | Reflection | Intensity | C & L | Odd |
| **Polar MOKE** | Reflection | Polarization | L | Odd |
| **Longitudinal MOKE** | Reflection | Polarization | L | Odd |
| **Faraday Effect** | Transmission | Polarization | L | Odd |
| **Magnetic Circular Dichroism** | Transmission & Reflection | Intensity | C | Odd |
| **RMS scattering** | Reflection | Intensity | L | Odd |
| **Voigt Effect** | Transmission & Reflection | Polarization | L | Even |
| **Magnetic Linear Dichroism** | Transmission & Reflection | Intensity | L | Even |

## 2.2 Light in a Magnetic Material

First, I introduce the plane wave propagation of the electric field of a monochromatic electromagnetic wave (emw) as

$$\mathbf{E} = \mathbf{E}_0 e^{i(\omega t - \mathbf{k}\cdot\mathbf{r})}. \tag{2.1}$$

Any interaction between this emw and a material is represented by the refractive index. This interaction is included in the term of $\mathbf{k}\cdot\mathbf{r}$ in Equation 2.1, and depends on the frequency of the emw (or wavelength). As the frequency of the emw increases, this interaction weakens and the refractive index approaches unity for the extreme ultraviolet and x-ray regions of the electromagnetic spectrum. In this case, the refractive index is represented

$$n(\omega) = 1 - \delta(\omega) - i\beta(\omega), \tag{2.2}$$

where $\delta$ is responsible for refraction and dispersion and $\beta$ is due to the absorption of the emw, and both depend on the frequency of the emw. Because of the different electronic properties of materials for different crystalline directions in space by breaking spatial and structural symmetries, the refractive index of a material depends on the propagation direction and the polarization of the emw, which are called anisotropy (or birefringence) and dichroism, respectively. In addition to the broken symmetries, an existing magnetic field in a material also breaks time-reversal symmetry and introduce anisotropy that depends on the direction of the magnetic field. As a result of complex anisotropic materials, the refractive index does not have one value. Consequently, this anisotropy is usually expressed in terms of the dielectric tensor $\widehat{\epsilon} = n \cdot n$ of the material. For a magnetized material, the dielectric tensor $\widehat{\epsilon}$ is expressed as

$$\widehat{\epsilon} = \begin{pmatrix} \epsilon_{xx} & \epsilon_{xy} & \epsilon_{xz} \\ \epsilon_{yx} & \epsilon_{yy} & \epsilon_{yz} \\ \epsilon_{zx} & \epsilon_{zy} & \epsilon_{zz} \end{pmatrix} = \epsilon_q \begin{pmatrix} 1 & -iQm_z & iQm_y \\ iQm_z & 1 & -iQm_x \\ -iQm_y & iQm_x & 1 \end{pmatrix}, \tag{2.3}$$

where $\epsilon_q$ is the diagonal element of the dielectric tensor, $Q$ is the magneto-optical (MO) constant, and $\{m_x, m_y, m_z\}$ are the magnetization amplitudes, that are between 0 and 1, in the $\{x, y, z\}$ directions, respectively [91].

Next, I use the dielectric tensor and Maxwell's equations to derive the propagation of an emw in a magnetized material. These Maxwell's equations are

$$\nabla \times \mathbf{H} = \frac{\partial \mathbf{D}}{\partial t} = \frac{\partial}{\partial t}(\hat{\epsilon} \cdot \mathbf{E}), \tag{2.4}$$

$$\nabla \times \mathbf{E} = -\frac{\partial \mathbf{B}}{\partial t} = -\frac{\partial}{\partial t}(\hat{\mu} \cdot \mathbf{H}). \tag{2.5}$$

I apply the $\nabla\times$ operator to Equation 2.5 and combine it with Equation 2.4. After assuming $\mu$ is 1, and applying vector operations, Equation 2.5 becomes

$$-\mathbf{k}(\mathbf{k} \cdot \mathbf{E}) + (\mathbf{k} \cdot \mathbf{k})\mathbf{E} = \frac{k_0^2}{\epsilon_0}\hat{\epsilon} \cdot \mathbf{E}, \tag{2.6}$$

where $k_0 = \omega^2/c^2$.

Now I turn Equation 2.6 into an eigen problem by plugging in Equations 2.1 and 2.3 and thus find the corresponding eigenvalues and eigenvectors:

$$\begin{pmatrix} \epsilon_{xx}k_0^2 + k_y^2 + k_z^2 & -(\epsilon_{xy}k_0^2 + k_xk_y) & -(\epsilon_{xz}k_0^2 + k_xk_z) \\ -\epsilon_{yx}k_0^2 + k_xk_y) & -\epsilon_{yy}k_0^2 + k_x^2 + k_z^2 & -(\epsilon_{yz}k_0^2 + k_yk_z) \\ -(\epsilon_{zx}k_0^2 + k_xk_z) & -(\epsilon_{zy}k_0^2 + k_yk_z) & -\epsilon_{zz}k_0^2 + k_x^2 + k_y^2 \end{pmatrix} \begin{pmatrix} E_x \\ E_y \\ E_z \end{pmatrix} = 0. \tag{2.7}$$

Rather than finding a general solution, I split the magneto-optical effect into three parts based on their geometries and find simplified solutions [56]. As described in the Table 2.1, the MO effect can be studied in many different geometries. It is called the magneto-optical Kerr effect (MOKE) when a modulation in reflected light from a magnetized surface is present. MOKE appears in three different geometries: transverse, polar, and longitudinal. I show these geometries in Figure 2.1.

Next, I define the plane of incidence that is on the $xy$ plane, and will be same through the thesis. For the transverse geometry, the magnetization is in the $z$ direction and perpendicular to the plane of incidence. In contrast, the magnetization is parallel to the plane of incidence for polar and longitudinal MOKE, but perpendicular to the surface plane of the sample ($zy$) in a polar geometry.

After defining the axis geometry, I simplify Equation 2.3 for these three geometries by using the magnetization and the light-propagation directions. Then, the dielectric tensor $\hat{\epsilon}$ and the propagation vector $\mathbf{k}$ become:

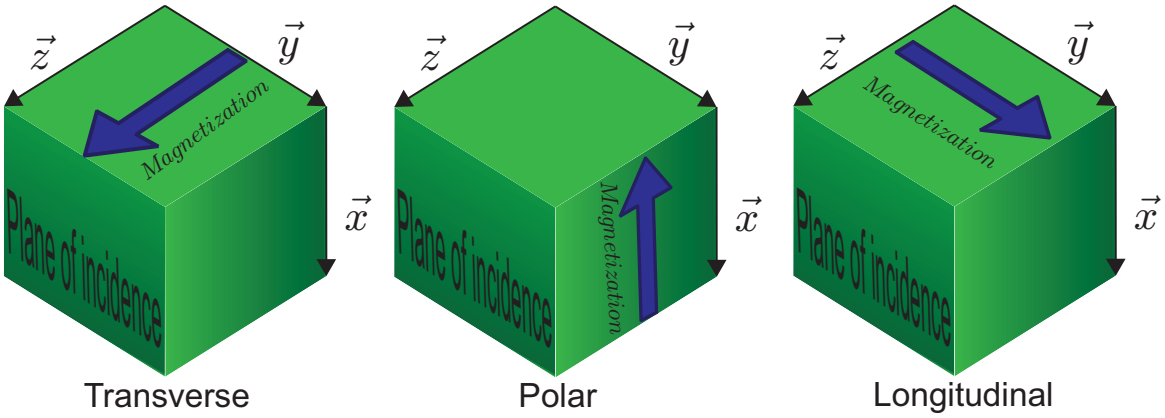


Figure 2.1: Three commonly used geometries, transverse, polar and longitudinal, for the magneto-optical Kerr effect (MOKE). When the magnetization is perpendicular to the plane of incidence, the geometry is a transverse MOKE, which I employ in our experiments. In contrast, in the polar and longitudinal geometries, the magnetization is in the plane of incidence, but the magnetization is in $x$ and $y$ directions, respectively.

For Transverse magneto-optical Kerr effect (T-MOKE)

$$\hat{\epsilon} = \epsilon_q \begin{pmatrix} 1 & -iQ & 0 \\ iQ & 1 & 0 \\ 0 & 0 & 1 \end{pmatrix}; \mathbf{k} = n(k_0 \cos\theta, k_0 \sin\theta, 0).$$

For the polar magneto-optical Kerr effect (P-MOKE)

$$\hat{\epsilon} = \epsilon_q \begin{pmatrix} 1 & 0 & 0 \\ 0 & 1 & -iQ \\ 0 & iQ & 1 \end{pmatrix}; \mathbf{k} = n(k_0 \cos\theta, k_0 \sin\theta, 0).$$

Finally for longitudinal magneto-optical Kerr effect (L-MOKE)

$$\hat{\epsilon} = \epsilon_q \begin{pmatrix} 1 & 0 & iQ \\ 0 & 1 & 0 \\ -iQ & 0 & 1 \end{pmatrix}; \mathbf{k} = n(k_0 \cos\theta, k_0 \sin\theta, 0),$$

where $\theta$ is the angle of incidence.

Next, I plug these values in Equation 2.7 one by one and solve for the corresponding eigen

values of the refractive index $n$:

$$\begin{aligned} \textit{T-MOKE} &: \left(n_s \to \sqrt{\epsilon},\ n_p \to \sqrt{\epsilon(1-Q^2)}\right), \\ \textit{P-MOKE} &: \left(n_\pm \to \sqrt{\epsilon(1 \pm Q\cos\theta)}\right), \textit{and} \\ \textit{L-MOKE} &: \left(n_\pm \to \sqrt{\epsilon(1 \pm Q\sin\theta)}\right). \end{aligned} \tag{2.8}$$

Equation 2.8 indicates that only the p-polarized incident light is sensitive to magnetization, which is a variation in the intensity of reflected light in the T-MOKE geometry [56]. But the s-polarized light is not affected by the magnetic field. This is an advantage to probe only the charge and the lattice dynamics without interruption from magnetization. I focus only the T-MOKE geometry that is directly related to my thesis, but interested readers can find more detailed explanations for other geometries in Ref. [56].

Imagine a simple T-MOKE geometry with the propagation vector $\mathbf{k} = (k, 0, 0)$ and the electric field $\mathbf{E} = (0, E, 0)$. Then, the displacement vector $\mathbf{D} = \hat{\epsilon} \times \mathbf{E}$ becomes

$$\mathbf{D} = (iQE, E, 0). \tag{2.9}$$

The displacement vector $\mathbf{D}$ shows that the transverse magnetization introduces a displacement vector in the propagation direction with the magnitude $iQ\mathbf{E}$. By using this information, I now move to understanding the properties of reflection and transmission emw at interfaces of magnetized materials.

## 2.3 Light at an Interface

In the previous section, I showed the propagation characteristics of an emw in a magnetized material. Here I explain more practically how an emw behaves at interfaces, e.g., reflection and transmission. I show an example of an interface of two magnetic materials, medium $j$ and $j+1$, in Figure 2.2. The emw approaches the surface with an angle of $\theta_j$ and an amplitude of $E^k_{p,j}$. The reflected field has the same angle but an amplitude of $E^{-k}_{p,j}$. The transmitted emw in the second

medium has an angle of $\theta_{j+1}$ and an amplitude of $E^k_{p,j+1}$. The other three electric fields due to the MO effect are shown with the purple arrows; they have the coefficients $Q_j$ and $Q_{j+1}$.

I revisit Maxwell's equations and write the boundary conditions for an absence of a charge and a current at the interface as

$$\nabla \cdot \mathbf{E} = 0 \;\; ; \;\; \nabla \cdot \mathbf{B} = 0. \tag{2.10}$$

Equation 2.10 means that the total electric field in the $y$ axes and the total magnetic field in the $z$ axis should be both zero:

$$\sum E_y = 0 \;\; ; \;\; \sum H_z = 0. \tag{2.11}$$

Next, I use Equation 2.5 to find $H_z$ and the boundary conditions as follows

$$\begin{aligned} -E^k_{p,j}\cos\theta_j + iQ_jE^k_{p,j}\sin\theta_j + E^{-k}_{p,j}\cos\theta_j + iQ_jE^{-k}_{p,j}\sin\theta_j + \\ E^k_{p,j+1}\cos\theta_{j+1} - iQ_{j+1}E^k_{p,j+1}\sin\theta_{j+1} = 0, \text{ and} \end{aligned} \tag{2.12}$$

$$n_j\left(E^k_{p,j} + E^{-k}_{p,j}\right) - n_{j+1}E^k_{p,j+1} = 0. \tag{2.13}$$

After couple of lines of algebra [12], the reflection and transmission coefficients are found to be

$$\begin{aligned} r_{pp} &= \frac{E^{-k}_{p,j}}{E^k_{p,j}} = (r^k_{pp})^0 + (r^k_{pp})^1, \\ (r^k_{pp})^0 &= \frac{n_{j+1}\cos\theta_j - n_j\cos\theta_{j+1}}{n_{j+1}\cos\theta_j + n_j\cos\theta_{j+1}}, \qquad (2.14) \\ (r^k_{pp})^1 &= \frac{2in_{j+1}\cos\theta_j\left[n_jQ_{j+1}\sin\theta_{j+1} - n_{j+1}Q_j\sin\theta_{j+1}\right]}{\left(n_{j+1}\cos\theta_j + n_j\cos\theta_{j+1}\right)^2}, \qquad (2.15) \\ t_{pp} &= \frac{E^k_{p,j+1}}{E^k_{p,j}} = (t^k_{pp})^0 + (t^k_{pp})^1, \\ (t^k_{pp})^0 &= \frac{n_j}{n_{j+1}}\left[1 + (r^k_{pp})^0\right] = \frac{2n_j\cos\theta_j}{n_{j+1}\cos\theta_j + n_j\cos\theta_{j+1}}, \text{ and} \qquad (2.16) \\ (t^k_{pp})^1 &= \frac{n_j}{n_{j+1}}(r^k_{pp})^0 = \frac{2in_j\cos\theta_j\left[n_jQ_{j+1}\sin\theta_{j+1} - n_{j+1}Q_j\sin\theta_{j+1}\right]}{\left(n_{j+1}\cos\theta_j + n_j\cos\theta_{j+1}\right)^2}, \qquad (2.17) \end{aligned}$$

where Equations 2.14 and 2.16 are commonly used Fresnel reflection and transmission coefficients for nonmagnetic materials. In addition, Equations 2.15 and 2.17 are the magnetic contribution in

the reflected and transmitted fields obtained by expanding only the first order of the magneto-optic constant $Q$, because this constant for all magnetic materials is $Q << 1$.

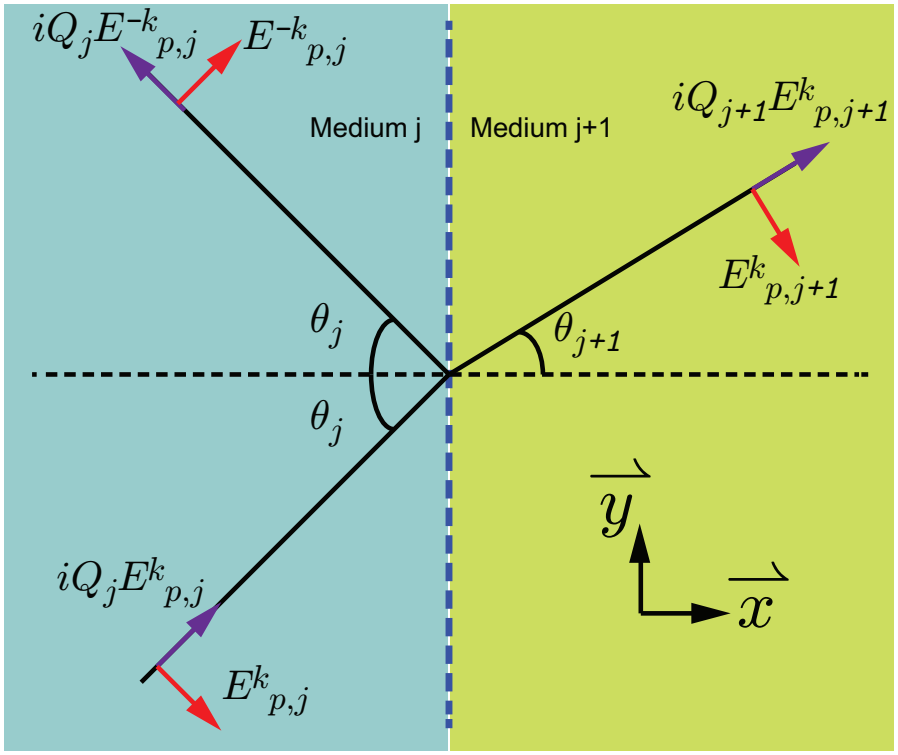


Figure 2.2: Interface of two magnetic media. The first medium is $j$, and the second one is $j+1$. The incoming light is p-polarized, and the angle of incidence is $\theta_j$. The amplitude of the incoming electric field is $E^k_{p,j}$, where $k$ means the direction of propagation. The reflected electric field is $E^{-k}_{p,j}$. In the second medium, the propagation direction has an angle $\theta_{j+1}$ with the normal, and the electric field is $E^k_{p,j+1}$. In the text, I explain boundary conditions and their relationship between these fields.

The reflection and transmission coefficients in Equations 2.14, 2.15, 2.16, and 2.17 are derived for general cases. For usual experimental conditions, there is only one semi-infinite magnetic layer in air. In this simpler geometry, $Q_j = 0$, and $n_j = 1$. Then, the reflected intensities for the s- and p-polarized light become

$$I_s = I_0 \left| \frac{\cos\theta_j - n\cos\theta_{j+1}}{\cos\theta_j + n\cos\theta_{j+1}} \right|^2, \ (and) \tag{2.18}$$

$$I_p^{\pm} = I_0 \left| \frac{n\cos\theta_j - \cos\theta_{j+1}}{n\cos\theta_j + \cos\theta_{j+1}} \pm \frac{2iQ\sin\theta\cos\theta}{(n\cos\theta_j + \cos\theta_{j+1})^2} \right|^2. \tag{2.19}$$

Sometimes, instead of $Q$, $\epsilon_{xy}$ is used, and the relation between two is $\epsilon_{xy} = iQn^2$. Fur-

thermore, the sign ± in Equation 2.19 means that the magnetization direction can vary, and the intensity of reflected p-polarized light will be different. However, by measuring the intensity for only one direction of the magnetization does not give enough information about the magnetic state of a material since Equation 2.19 has a large contribution from the first Fresnel term. Using a simple trick by employing this ± asymmetry argument, the magnetic information can be extracted straightforwardly. The normalized difference of the reflected lights as the magnetization of the material reverses is called **magnetic asymmetry** that is proportional to magneto-optical constant $Q_{m_z}$. Thus,

$$\mathbf{A} = \frac{I_p^+ - I_p^-}{I_p^+ + I_p^-} = \frac{|r_p^0 + r_p^1|^2 - |r_p^0 - r_p^1|^2}{|r_p^0 + r_p^1|^2 + |r_p^0 - r_p^1|^2}, \tag{2.20}$$

where $r_p^0$ and $r_0^1$ are the nonmagnetic and magnetic contributions to the reflection shown in Equation 2.19. After a couple of simplifying steps, the asymmetry term becomes

$$\begin{aligned} A &\cong 2\mathsf{Re}\left[\frac{r_p^1}{r_p^0}\right]\overbrace{\left(1 - \frac{|r_p^1|^2}{|r_p^0|^2}\right)}^{1} \\ &= 2\mathsf{Re}\left[\frac{\sin 2\theta \epsilon_{xy}}{n^4\cos^2\theta - n^2 + \sin^2\theta}\right]. \end{aligned} \tag{2.21}$$

Because of $|r_p^1| << |r_p^0|$, the term in parenthesis is usually assumed one, and the simplified version of the asymmetry is used. However, the neglected term is not small in some cases, as shown in Figure 2.3b. Actually, it can result in a 23% error in the magnetization of a material at angle of incidence 45°.

So far, I have elaborated the T-MOKE for general materials but the effect of the refractive index has not been discussed. As mentioned earlier the refractive indices of materials in the extreme ultraviolet and x-ray wavelengths approach unity. This brings us to the magnetic asymmetry described by Equation 2.21. The magnetic asymmetry is at a maximum when the denominator approaches zero at the Brewster angle of incidence, i.e.,

$$\sin\theta_B = \frac{n^2}{n^2 + 1}. \tag{2.22}$$

$\theta_B$ is 45° when $n$ approaches to 1 for x-rays. Next, I take a closer look at the asymmetry parameter with the tabulated values of the refractive index and MO constants. For example, for Ni near the

M-absorption edge at 67 eV the refractive index $n$ is $1 - 0.01066 - i0.1003$ and MO constant $\epsilon_{xy}$ is $-0.007 - i0.0066$ or $-0.0052 + i0.0079$ from two different sources [32, 84].

By using tabulated values above, I calculate the angle-dependence of the reflected intensities of s- and p-polarized incident lights and the neglected term in Equation 2.21, in Figure 2.3. The blue curves indicate that the Brewster angle is near 45° but may not be exactly at 45° because of a certain magneto-optical effect. One can also see that the p-polarized reflectivity of light is two orders of magnitude smaller than the s-polarized reflectivity of light. As a result, performing experiments with p-polarized light requires long measurement times to get good statistics. In addition, I plot the neglected term as a function of angle in Figure 2.3. One can immediately see that the error in the assumption is approximately 23% at 45° and the simplified version of asymmetry in 2.21 is also not fully correct in the 45° ±5° angle range.

The normalized difference between the dashed-blue and light-blue lines gives the full asymmetry shown in Figure 2.4. I calculate and plot asymmetry vs. angle for two different values of the magneto-optical (MO) constant $\epsilon_{xy}$. The first distinct feature is the plots are reversed for two different MO constants, $\epsilon_{xy} = -0.0052 + i0.0079$ and $\epsilon_{xy} = -0.007 - i0.0066$. The phase of MO constant is responsible for this distinct behavior rather than the amplitude. Thus, there are two different angles that maximize the asymmetry, at 46.2° and 43°. I also plot the full asymmetry with and without the approximation that again reminds us of the discrepancy around 45°.

The question is whether the asymmetry parameter is really a representation of magnetization dynamics in the case of any magnitude change in the magnetization. The answer is: not always. The MO effect needs to be investigated carefully to claim pure magnetization probing and I report such an investigation in Figure 2.5. First, I assume that the system is excited and the magnetization exponentially drops and recovers back with a function of $(1 - 0.5[1 - e^{-t/0.2}e^{-t/5}])$ as will discussed in Chapters 5-7. The MO constant is proportional to the magnetization, so that I can change the MO constant at the same rate and calculate the asymmetry parameter in the same timescales. Surprisingly, the asymmetry does not fully represent the dynamics of MO constant at 45°, as shown in Figure 2.5. Actually, it is 8% less than it is supposed to be. This does not mean there is some

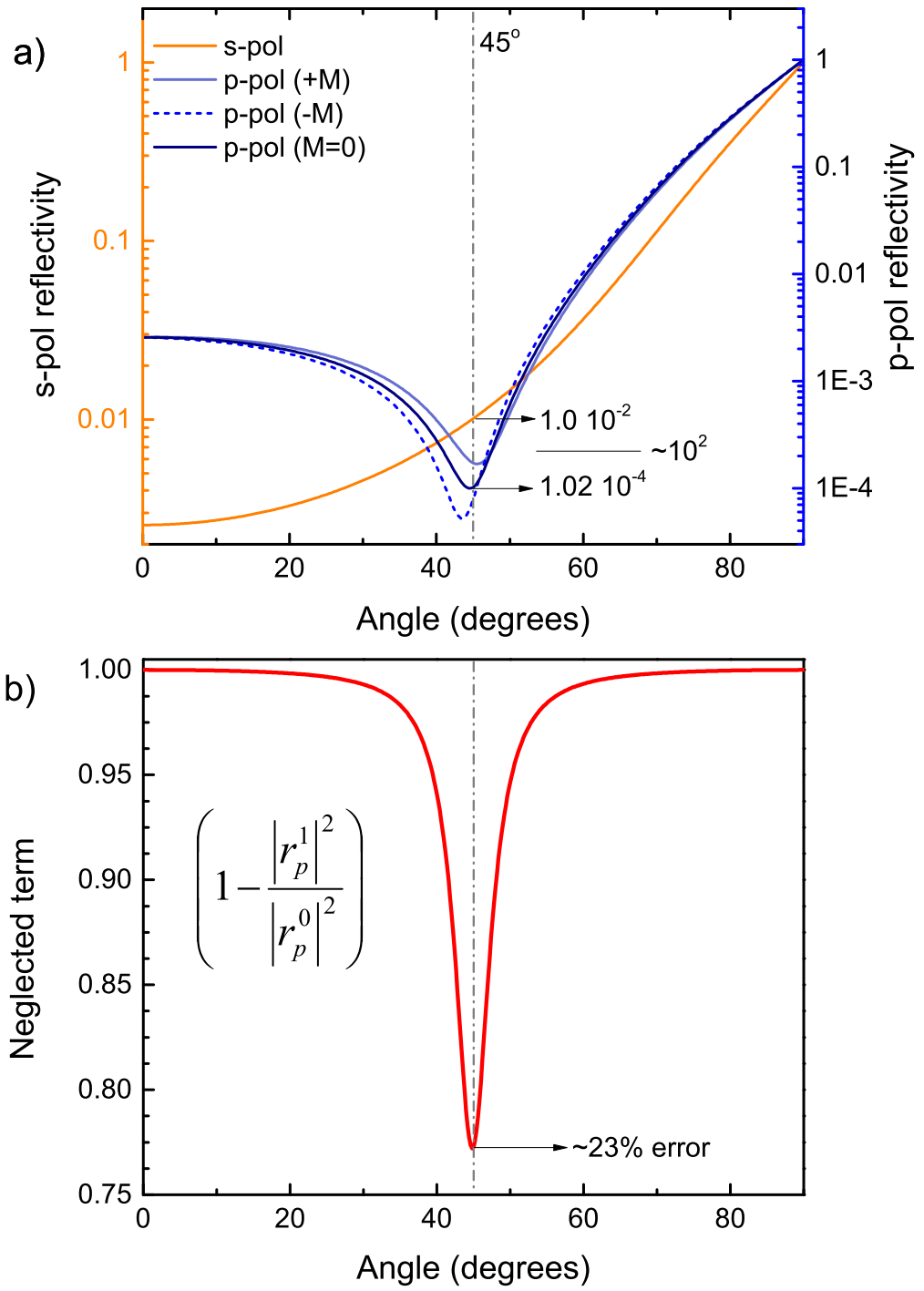


Figure 2.3: (Top) Reflected intensities of s- and p-polarized lights from semi-infinite Ni surface at the $M_{2,3}$ absorption edge of 67 eV. The minimum reflection is at a Brewster angle near 45° where the magnetic asymmetry peaks. Note that the reflectivity almost goes to zero with p-polarized incident light at the Brewster angle which makes experiment challenging. (Bottom) The neglected term in Equation 2.21. This approximation in Equation 2.21 is not valid for all angles and the error is approximately 23% at angle of incidence 45°.

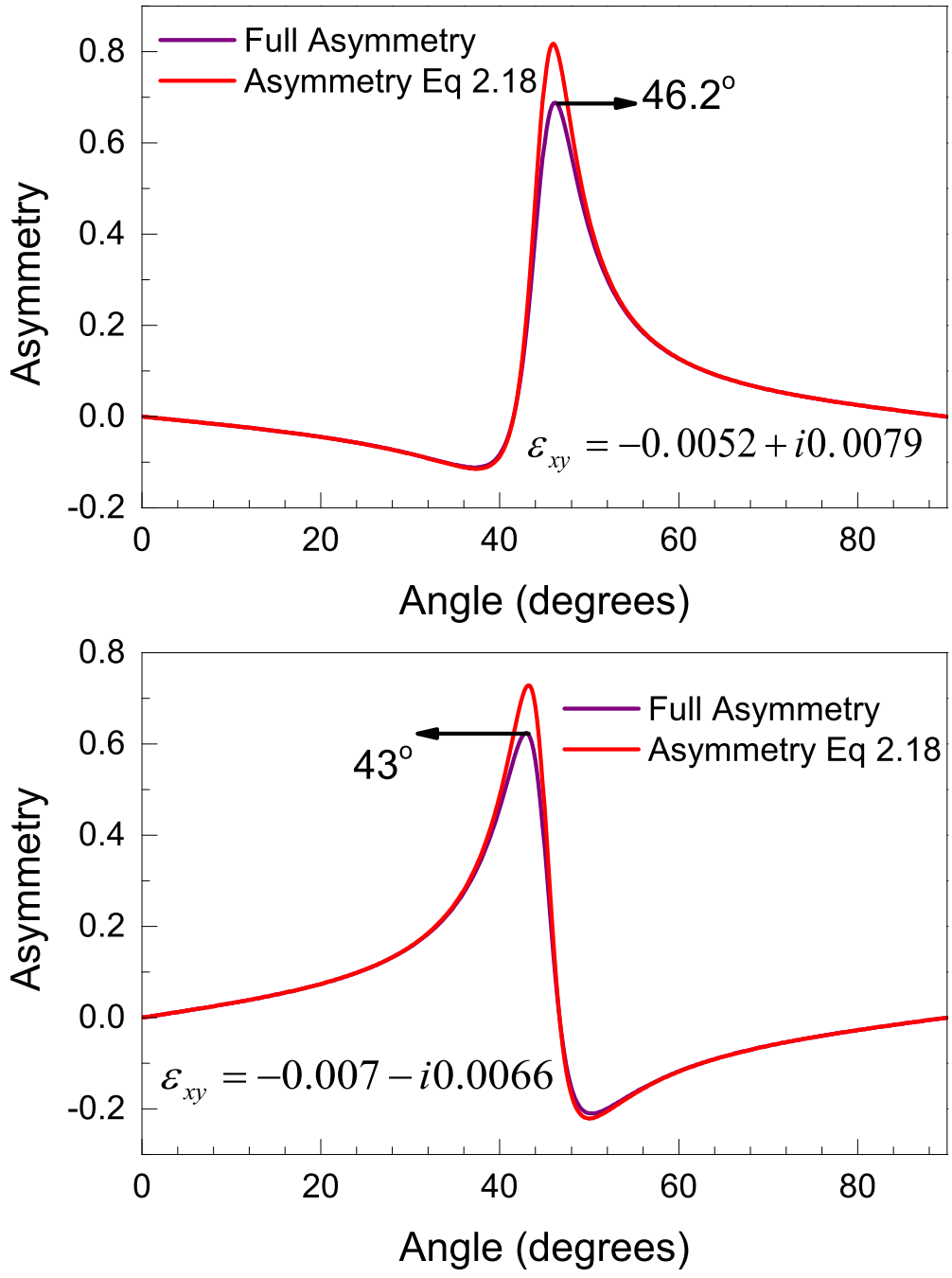


Figure 2.4: Asymmetries vs. angle plots for two different $\epsilon_{xy}$. (Top) Asymmetry with and without the assumption as in Equation 2.21 for $\epsilon_{xy} = -0.0052 + i0.0079$. The maximum asymmetry is at 46.2°. (Bottom) Same as above with $\epsilon_{xy} = -0.007 - i0.0066$. Here, the maximum shifts to the 43°, and the shape of the curve is reversed. The amplitude of $\epsilon_{xy}$ does not affect the asymmetry; however, the asymmetry is very sensitive to the phase of $\epsilon_{xy}$.

artifact in the experiment. Rather the asymmetry is not linearly proportional to the MO constant at 45°, as shown in Figure 2.3b.

My goal in these investigations is to point out that;

- The asymmetry does not necessarily maximize at 45°.
- One should be careful with the angle of incidence when using Equation 2.21.
- The phase of the MO constant is the most important parameter for determining the behavior of the asymmetry.
- At angle of incidence 45°, the asymmetry is not linearly proportional to the MO constant which means that being slightly off from 45° can give better asymmetry and represent more accurate magnetization dynamics.

The asymmetry term can be more simplified, to understand physical origin and interpret easier. For example in Equation 2.21, I replace $n$ with $1-\delta-i\beta$ and perform one page simplification and assumptions by using $\delta, \beta << 1$, as shown in Appendix A. Then, the asymmetry term becomes

$$A \cong \frac{\sin 2\theta}{(1-2\cos^2\theta)}\left[\frac{\delta Re[\epsilon_{xy}]-\beta Im[\epsilon_{xy}]}{\delta^2+\beta^2}\right]. \tag{2.23}$$

This expression is not valid around 45°, but it can be very useful in linking the real and imaginary parts of the MO constant at other angles.

Interestingly, the asymmetry term becomes more handy at 45°. I plug in $\theta = 45°$ into Equation 2.21 and neglect higher order terms of $\delta$ and $\beta$, as explained more detailed in Appendix A to become

$$A \cong Re[\epsilon_{xy}]\frac{\delta^2-\beta^2+3\beta^2\delta-\delta^3}{(1-2\delta)\left(\beta^2+\delta^2\right)^2}+Im[\epsilon_{xy}]\frac{2\delta\beta-3\beta\delta^2+\beta^3}{(1-2\delta)\left(\beta^2+\delta^2\right)^2}. \tag{2.24}$$

Equation 2.24 may not look more handy, but it separates the real and imaginary parts of the MO constant in the asymmetry parameter. I further clarify Equation 2.24 more by comparing $\delta$

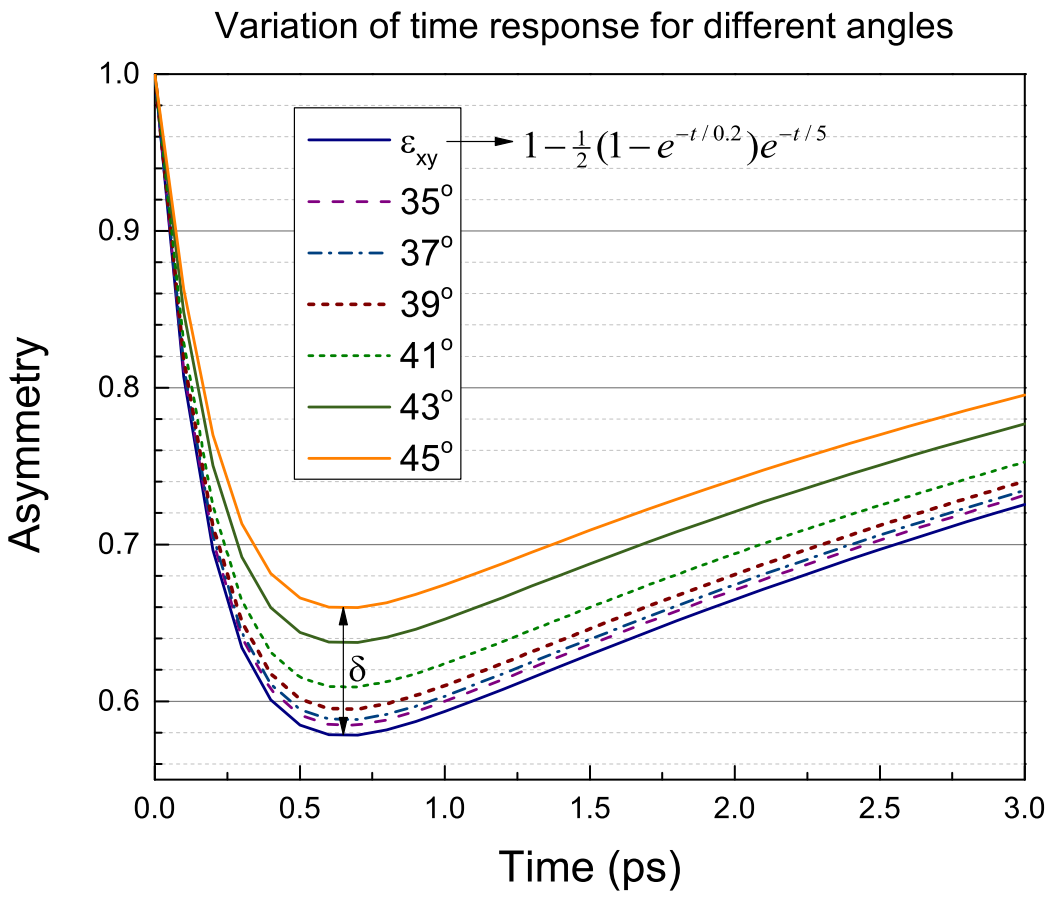


Figure 2.5: Comparison of the proportionality of the asymmetry to the MO constant. I introduce an ultrafast demagnetization to the MO constant as a function of $t$ $[1-0.5(1-e^{-t/0.2}e^{-t/5})]$ shown by the black curve. Then I calculate the asymmetry parameter as a function of time for different angles. Surprisingly, the transient dynamics of asymmetry at 45° do not represent the MO constant proportionally. This is not an artifact, but a pure magnetic signal. The difference $\delta$ is about 0.08, which means that the asymmetry is not linearly proportional to the MO constant.

and $\beta$ values in metals. For example, $\delta \sim 0.01$ and $\beta \sim 0.1$ for Ni at $\sim 67eV$, revealing that around the absorption edge $\delta << \beta$. As a result, I simplify the asymmetry even more with

$$A \cong \frac{-Re[\epsilon_{xy}]\beta^2 + Im[\epsilon_{xy}]\beta(2\delta + \beta^2)}{\beta^4} \cong -Re[\epsilon_{xy}]/\beta^2, \tag{2.25}$$

which indicates that the magnetic asymmetry is a function of the real part of the MO constant and the imaginary part of the refractive index.

Thus far I investigated the properties of the magnetic asymmetry parameter and the MO constant for semi-infinite structures. However, there are many magnetic or nonmagnetic layers to create structurally better systems or to study more complex dynamics in our experiments. Therefore, I next give more theoretical background about T-MOKE in multilayers.

## 2.4 T-MOKE of Multilayer Structures

As I showed in the last section, theoretical description of T-MOKE asymmetry for a semi-infinite sample system can be very different than expected, and one must take special care to conduct a careful analysis. This analysis become more important to understand and examine T-MOKE in magnetic multilayers [12].

In this section, I use the full matrix method to study reflections and transmissions through multilayer structures. First, I derive the reflection $r_p$ and transmission $t_p$ coefficients for the backward-propagating wave by Equations 2.14–2.17 and symmetry argument, as shown in Figure 2.6. For the backward-propagating waves, the coefficients become

$$(r_{pp}^{-k})^0 = -(r_{pp}^{k})^0 = \frac{n_j \cos\theta_{j+1} - n_{j+1}\cos\theta_j}{n_{j+1}\cos\theta_j + n_j \cos\theta_{j+1}}, \tag{2.26}$$

$$(t_{pp}^{-k})^0 = \frac{n_{j+1}}{n_j}\left[1 - (r_{pp}^{k})^0\right] = \frac{2n_{j+1}\cos\theta_{j+1}}{n_{j+1}\cos\theta_j + n_j \cos\theta_{j+1}}, \tag{2.27}$$

$$(r_{pp}^{-k})^1 = \frac{2in_j \cos\theta_{j+1}\left[n_j Q_{j+1}\sin\theta_{j+1} - n_{j+1}Q_j \sin\theta_{j+1}\right]}{\left(n_{j+1}\cos\theta_j + n_j\cos\theta_{j+1}\right)^2}, \text{ and} \tag{2.28}$$

$$(t_{pp}^{-k})^1 = \frac{n_{j+1}}{n_j}(r_{pp}^{-k})^1 = \frac{2in_{j+1}\cos\theta_{j+1}\left[n_j Q_{j+1}\sin\theta_{j+1} - n_{j+1}Q_j \sin\theta_{j+1}\right]}{\left(n_{j+1}\cos\theta_j + n_j\cos\theta_{j+1}\right)^2}. \tag{2.29}$$

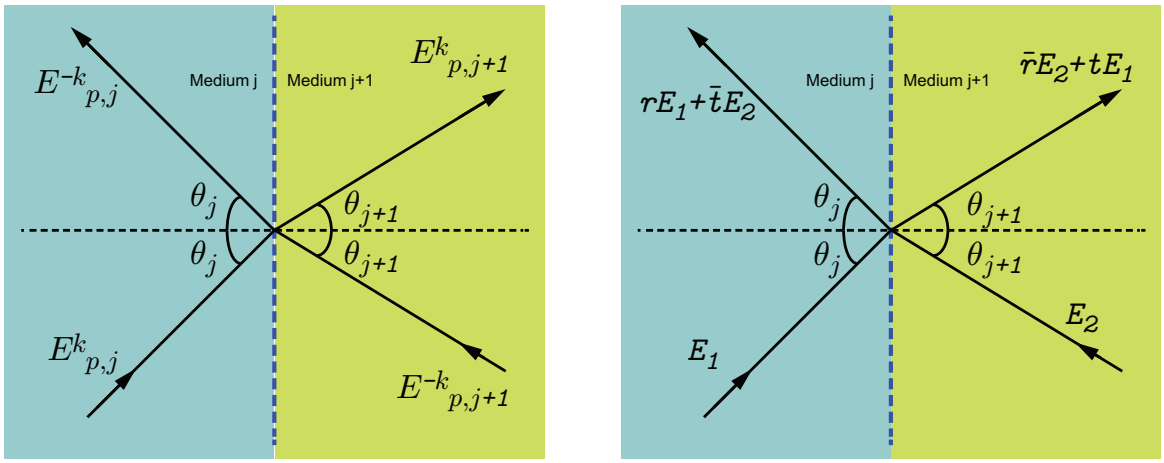


Figure 2.6: Representation of the forward- and backward-propagating waves and their reflected and transmitted waves. It is essential for matrix formalism to identify coefficients at interfaces. (Left) I show four waves: two are incoming, and two are leaving the interface. I represent the leaving waves in terms of incoming waves $E_1$ and $E_2$ by using the reflection and transmission coefficients. The leaving wave in the medium $j$ is $rE_1 + \bar{t}E_2$ and the leaving one in the medium $j+1$ is $\bar{r}E_2 + tE_1$.

The superscripts 0 and 1 represent non-magnetic Fresnel coefficient and magnetic contribution, respectively. These coefficients are long and complex to use. Instead of these long versions, I use $\bar{r}$ for the reflection $((r^{-k}_{pp})^0 + (r^{-k}_{pp})^1)$and $\bar{t}$ for the transmission $((t^{-k}_{pp})^0 + (t^{-k}_{pp})^1)$. As in Figure 2.6, $E_1$ is the forward- and $E_2$ is the backward-propagating incoming waves. The reflected and transmitted waves are shown as functions of $E_1$, $E_2$, and the Fresnel coefficients, namely $rE_1 + \bar{t}E_2$ for medium $j$ and $\bar{r}E_2 + tE_1$ for the medium $j+1$. This representation will be useful in the next step for building the matrix formalism.

At the interface where the waves propagate from one medium to the next one, I define the dynamics matrix $\widehat{D}$ as follows

$$\begin{pmatrix} E^{k}_{p,j} \\ E^{-k}_{p,j} \end{pmatrix} = \widehat{D} \begin{pmatrix} E^{k}_{p,j+1} \\ E^{-k}_{p,j+1} \end{pmatrix}, \tag{2.30}$$

which tells us that multiplication of the dynamics matrix with the electric fields in the medium $j+1$ gives the electric fields in the medium $j$. Now, to find $\widehat{D}$, I represent the electric fields in

terms of the Fresnel coefficients:

$$E_{p,j}^{-k} = rE_1 + \overline{t}E_2, \tag{2.31}$$

$$E_{p,j+1}^{k} = \overline{r}E_2 + tE_1. \tag{2.32}$$

From these two equations, I now find $E_1$ and $E_{p,j}^{-k}$ in terms of $E_2$ and $E_{p,j+1}^{k}$

$$E_1 = \frac{1}{t}E_{p,j+1}^{k} - \frac{\overline{r}}{t}E_2, \tag{2.33}$$

$$E_{p,j}^{-k} = \frac{r}{t}E_{p,j+1}^{k} + \frac{t\overline{t} - r\overline{r}}{t}E_2, \tag{2.34}$$

which allows us to build $\widehat{D}$ as in

$$\widehat{D} = \frac{1}{t}\begin{pmatrix} 1 & -\overline{r} \\ r & t\overline{t} - r\overline{r} \end{pmatrix}. \tag{2.35}$$

The next step is to drive the propagation matrix in an arbitrary medium. I assume a layer with a thickness of $d_j$, the refractive index $n_j$, and the angle of propagation vector in the medium $\theta_j$. Phase differences for the forward- and backward-propagating waves are $e^{-i\mathbf{k}\cdot\mathbf{r}} = e^{-i2\pi n_j d_j \cos\theta_j/\lambda}$ and $e^{i2\pi n_j d_j \cos\theta_j/\lambda}$, respectively. Next, I write the relations between the waves at the left and right sides of the medium as in Figure 2.7

$$E_{p,j+1}^{'k} = E_{p,j+1}^{k} e^{-i2\pi n_j d_j \cos\theta_j/\lambda},$$

$$E_{p,j+1}^{'-k} = E_{p,j+1}^{-k} e^{i2\pi n_j d_j \cos\theta_j/\lambda};$$

and the propagation matrix $\widehat{U}$ becomes

$$\begin{pmatrix} E_{p,j+1}^{k} \\ E_{p,j+1}^{-k} \end{pmatrix} = \widehat{U} \cdot \begin{pmatrix} E_{p,j+1}^{'k} \\ E_{p,j+1}^{'-k} \end{pmatrix}; \text{ where } \widehat{U} = \begin{pmatrix} e^{i\varphi_x} & 0 \\ 0 & e^{-i\varphi_x} \end{pmatrix}. \tag{2.36}$$

Finally, I combine the dynamic matrix and the propagation matrix for a multilayer that includes N layers as shown in Figure 2.8. Here $n_j$ refers to the refractive index, $d_j$ is the thickness, $\widehat{U_j}$ is the propagation matrix, and $\theta_j$ the angle of propagation with respect to the normal of the surface of $j^{th}$ medium [59, 12]. The $j^{th}$ interface is the interface of media $j$ and $j+1$, and the

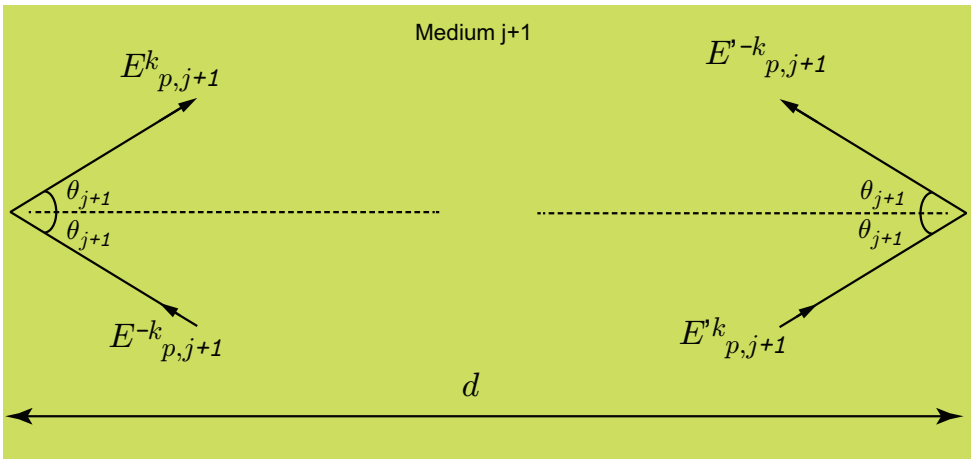


Figure 2.7: Propagation of an emw in a magnetized medium. I show how the left-side electric fields depend on the right-side of electric fields because of propagation parameters.

dynamic matrix at this interface is $\widehat{D_j}$. The bottom layer of the substrate is shown as $s$. Next, if I assume no incoming emw from the bottom of the structure, the relationship of the reflected and transmitted electric fields to the incoming electric field is

$$\begin{pmatrix} E_i \\ E_r \end{pmatrix} = D_0 \cdot U_1 \cdot D_1 \cdots D_{N-1} \cdot U_N \cdot D_N \begin{pmatrix} E_t \\ 0 \end{pmatrix}. \tag{2.37}$$

The result of all these matrix multiplications is called the $M$ *matrix*, which can be represented as

$$\begin{pmatrix} E_i \\ E_r \end{pmatrix} = \begin{pmatrix} M_{11} & M_{12} \\ M_{21} & M_{22} \end{pmatrix} \cdot \begin{pmatrix} E_t \\ 0 \end{pmatrix}. \tag{2.38}$$

The reflection and transmission coefficients of an entire multilayer stack then become

$$r = \frac{M_{21}(\theta_0, d_1, n_1, Q_1, \cdots d_N, n_N, Q_N, n_s, Q_s)}{M_{11}(\theta_0, d_1, n_1, Q_1, \cdots d_N, n_N, Q_N, n_s, Q_s)}, \tag{2.39}$$

and

$$t = \frac{1}{M_{11}(\theta_0, d_1, n_1, Q_1, \cdots d_N, n_N, Q_N, n_s, Q_s)}. \tag{2.40}$$

As in the semi-infinite T-MOKE case, one can finally reproduce the magnetic asymmetry parameter by normalized difference of the reflected intensities by reversing the required $Q$ values,

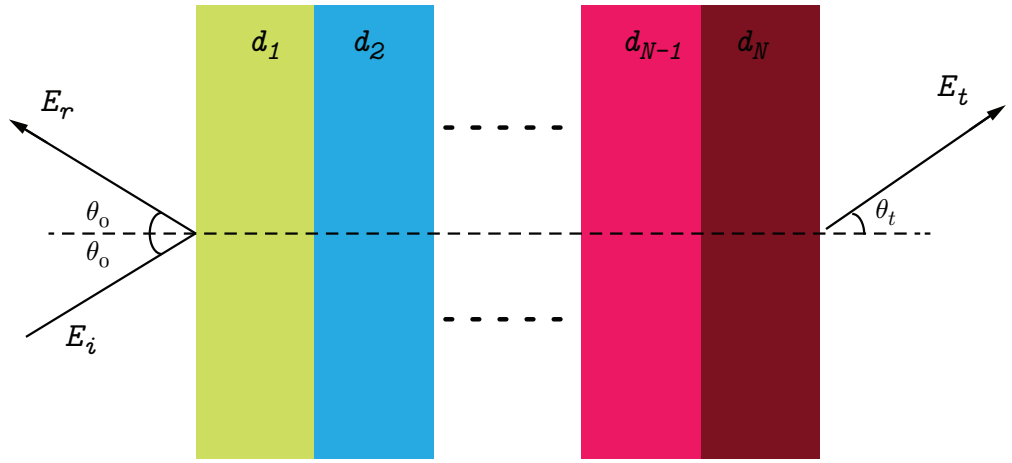


Figure 2.8: Illustration of multilayer structure. The experimental system I study is composed of N layers with the $s$ substrate at the bottom. Each interface has a dynamics matrix, and each layer has a propagation matrix. The relationship of the transmitted and reflected electric fields can be found by multiplication of all the dynamics and propagation matrices.

i.e.,

$$A_{multilayer} = \frac{|r_{mag1}|^2 - |r_{mag2}|^2}{|r_{mag1}|^2 + |r_{mag2}|^2}, \tag{2.41}$$

where $mag1$ and $mag2$ are different magnetization configurations of the layers.

To summarize multilayer T-MOKE section, I

- write boundary conditions of the electric and magnetic fields at the interface of two magnetized materials,
- calculate the reflection and the transmission coefficients,
- reproduce these coefficients for the backward-propagating waves,
- represent the dynamics matrix at an interface depending on these coefficients,
- calculate the propagation matrix that gives phase differences to the fields in the medium, and
- derive the total reflection and transmission coefficients as a function of the M matrix, which is the multiplication of all dynamics and propagation matrices.

Finally, I will compare multilayer calculations with experimental T-MOKE spectrum in Appendix B.

## 2.5 X-ray Magnetic Circular Dichroism

The final magneto-optical (MO) effect I discuss is x-ray magnetic circular dichroism (XMCD). XMCD employs circularly polarized x-rays in a transmission geometry with an out-of-plane magnetization. The theoretical framework of XMCD is similar to the P-MOKE in which the refractive index of the material has two values $n_{\pm} = \sqrt{\epsilon(1 \pm Q\cos\theta)}$. These two solution for the refractive index have two corresponding eigen vectors which are left and right circularly polarized light. Thus, the refractive index is different for the left and the right circular polarization resulting in an asymmetry in absorption [78, 56].

XMCD is generally performed at normal incidence ($\theta = 0$) to obtain the largest contrast. In this case, the refractive indices for two different polarizations become

$$n_+ \simeq n_0(1 + Q/2) \rightarrow right\ chirality; n_- \simeq n_0(1 - Q/2) \rightarrow left\ chirality. \tag{2.42}$$

If one calculates the absorption ratios of the left and right circularly polarized light for a material with a thickness $d$, as below

$$\frac{I_+}{I_-} = \frac{|E_0 e^{-ik_0 n_+ d}|^2}{|E_0 e^{-ik_0 n_- d}|^2} = \frac{e^{-2k_0 d Im(n_+)}}{e^{-2k_0 d Im(n_-)}}. \tag{2.43}$$

This ratio is usually represented by only the imaginary part of the MO constant by assuming $\delta, \beta << 1$. However, the exact definition is more complicated. I now replace $n_0$ with $1 - \delta - i\beta$ and plug $Q = Q_{re} + iQ_{im}$ into

$$Ratio \quad r = \ e^{-2k_0 d(Im(n_+) - Im(n_-))} = Exp\left[-2k_0 d\left(Q_{im} - \delta Q_{im} - \beta Q_{re}\right)\right], \tag{2.44}$$

where $Q = i\epsilon_{xy}/\epsilon_{xx}$. Experimentally, the entire absorption edge of a material should be resolved in the spectrometer to extract the full information of the magnetization states. Thus, the thicknesses of samples must be small. Hence, the term in the exponential function $2k_0 d\left(Q_{im} - \delta Q_{im} - \beta Q_{re}\right)$

become $<< 1$, and I can approximate the ratio as $1 - 2k_0 dQ_{im}$ by using $e^x = 1 + x$, if $x << 1$ and assuming $\delta, \beta << 1$. Moreover, the asymmetry term is also a useful parameter for ensuring that XMCD has a linear proportionality to the MO constant [42, 56]. Finally, the normalized difference of the transmitted left and right circularly polarized x-ray intensities becomes

$$A_{XMCD} = \frac{I_+ - I_-}{I_+ + I_-} = \frac{r-1}{r+1} \approx \ k_0 dQ_{im}, \tag{2.45}$$

which shows that the magnetic asymmetry is linearly proportional to the MO constant and the thickness of the material. One can improve the asymmetry contrast by increasing the thickness. However, increasing thickness is a drawback to seeing the absorption edge entirely.

## 2.6 Macroscopic and Microscopic Origin of $\epsilon_{xy}$

In the previous sections, I mentioned the of MO effects at different geometries. Now, I talk more about the physical origin of MO effect. First, I provide a brief summary of the macroscopic origin of the MO constant $\epsilon_{xy}$. Second, I talk about the microscopic origin of $\epsilon_{xy}$.

### 2.6.1 Macroscopic Origin of $\epsilon_{xy}$

The classical description of the dielectric constant starts with the harmonic oscillator picture of an electron. I assume that the electron is attached to the atom by a spring that has some damping. Then, an oscillating emw and a constant magnetic field or magnetization will apply a driving force to the electron. The electron's equation of motion is

$$m\ddot{\vec{r}} + m\Gamma\dot{\vec{r}} + m\omega_0^2\vec{r} = -e\vec{E} - e\dot{\vec{r}} \times \vec{B}, \tag{2.46}$$

where $m$ is the mass, and $e$ is the charge of electron, $\Gamma$ is the damping constant, $\omega_0$ is the resonance frequency, and the applied-magnetic field $\vec{B}$ is in the $z$ direction. Then, I use $\vec{r} = \vec{r}_0 e^{-i\omega t}$ for the displacement, where $\omega$ is the frequency of emw. The equation of motion becomes

$$\left(-m\omega^2 - im\omega\Gamma + m\omega_0^2\right)\vec{r} = -e\vec{E} + ie\omega\vec{r} \times \vec{B}. \tag{2.47}$$

Now, I can expand Equation 2.47 in the Cartesian coordinates with $\vec{r} = (r_x, r_y, r_z)$. Now $r_x$, $r_y$, and $r_z$ become

$$r_x = \frac{-eE_x + ie\omega r_y B}{m(\omega_0^2 - \omega^2 - i\omega\Gamma)}, \tag{2.48}$$

$$r_y = \frac{-eE_y + ie\omega r_x B}{m(\omega_0^2 - \omega^2 - i\omega\Gamma)}, \tag{2.49}$$

$$r_z = \frac{-eE_z}{m(\omega_0^2 - \omega^2 - i\omega\Gamma)}. \tag{2.50}$$

I can now find $r_x$ and $r_y$ independent of each other by plugging one in the other

$$r_x = \frac{e}{m}\,\frac{-\gamma E_x - 2i\omega\omega_L E_y}{\gamma^2 - 4\omega^2\omega_L^2}, \tag{2.51}$$

$$r_y = \frac{e}{m}\,\frac{-\gamma E_y + 2i\omega\omega_L E_x}{\gamma^2 - 4\omega^2\omega_L^2}, \tag{2.52}$$

where $\gamma = \omega_0^2 - \omega^2 - i\omega\Gamma$, and the Larmor frequency $\omega_L$ is $eB/2m$.

The macroscopic response to the electric field is called polarization $\vec{P}$. The $\vec{P}$ is a density of dipole moment that can be described as $\vec{p}N/V$, with the individual dipole moment of an electron $\vec{p}$, and a number of electrons $N$ in a volume $V$.

I now connect the macroscopic definition of the polarization with the classical picture

$$\vec{P} = \chi\epsilon_0\vec{E} = e\vec{r}N/V, \tag{2.53}$$

where $\chi$ is the electric susceptibility, also known as $\epsilon - 1$. Finally I find the elements of dielectric tensor [71].

$$\epsilon_{xx} = \epsilon_{yy} = 1 + \frac{e^2N}{\epsilon_0 m_e V}\,\frac{\gamma}{\gamma^2 - 4\omega^2\omega_L^2}, \tag{2.54}$$

$$\epsilon_{zz} = 1 + \frac{e^2N}{\epsilon_0 m_e V}\,\frac{1}{\gamma}, \tag{2.55}$$

$$\epsilon_{xy} = -\epsilon_{yx} = \frac{e^2N}{\epsilon_0 m_e V}\,\frac{-i\omega\omega_L}{\gamma^2 - 4\omega^2\omega_L^2}, \tag{2.56}$$

where $\epsilon_0$ is the vacuum permittivity. The diagonal elements $\epsilon_{xx}$, $\epsilon_{yy}$, and $\epsilon_{zz}$ of the dielectric tensor are experimentally well known. By using the tabulated real and imaginary parts of the refractive index [32], I fit the values of $\omega_0$ and $\Gamma$. Then I find the MO constant $\epsilon_{xy}$ for the XUV region of

spectrum by using the tabulated and fitted constants and the Weiss field for cobalt as an example. The electron density of Co, $n_e = N/V = 1.98 \times 10^{29}$ [4], is used to find the multiplication factor $\frac{e^2 N}{\epsilon_0 m_e V} = 6.3 \times 10^{32}$. I show the results of these calculation, in Figure 2.9 for the M absorption edge around 60 eV. $\Gamma$ and $\omega_0$ variables are fitted and found $1.8 \times 10^{16}$ and $9.3 \times 10^{16}$, respectively [32]. I compare the measured and calculated $\epsilon_{xx}$ in the top graph of Figure 2.9. I focus near the absorption edge so that discrepancies at the low and high energy sides are expected with this simple model. Then, I recalculate and plot the off-diagonal element $\epsilon_{xy}$ in the bottom graph of Figure 2.9 for $\omega_L = 7 \times 10^{14}$. Indeed, the Larmor frequency can tell us about the strength of the magnetic field inside the material by

$$\omega_L = \frac{eB}{2m_e}.$$

From above formula, the Weiss field is 1000 Tesla, which is reasonable [31]. The calculated $\epsilon_{xy}$ looks surprisingly similar to the measured experimental values of ferromagnetic materials [33] in spite of the simpleness of the classical model. Although this classical picture does not change for different elements iron, cobalt and nickel except for shifting the resonance frequency $\omega_0$, the MO effect of these elements has distinct differences in the details. These differences are due to the itinerant ferromagnetic metals being complicated and having very different band structures resulting in different magnetic properties.

### 2.6.2 Microscopic Origin of $\epsilon_{xy}$

The microscopic picture of the $\epsilon_{xy}$ can be understood by the optical transition of electrons from a core level to an unoccupied state in the conduction band that is usually $3d$ levels [25]. This optical-transition calculation, modeled by using a conductivity tensor with Kubo linear-response theory, is written as

$$\hat{\epsilon}(\omega) = \mathbf{I} + \frac{4\pi i}{\omega}\hat{\sigma}(\omega), \tag{2.57}$$

where $\omega$ is the frequency of emw, $\mathbf{I}$ is the identity matrix, and $\sigma$ is the conductivity tensor. The conductivity tensor is calculated with the Kubo formula [56], as in

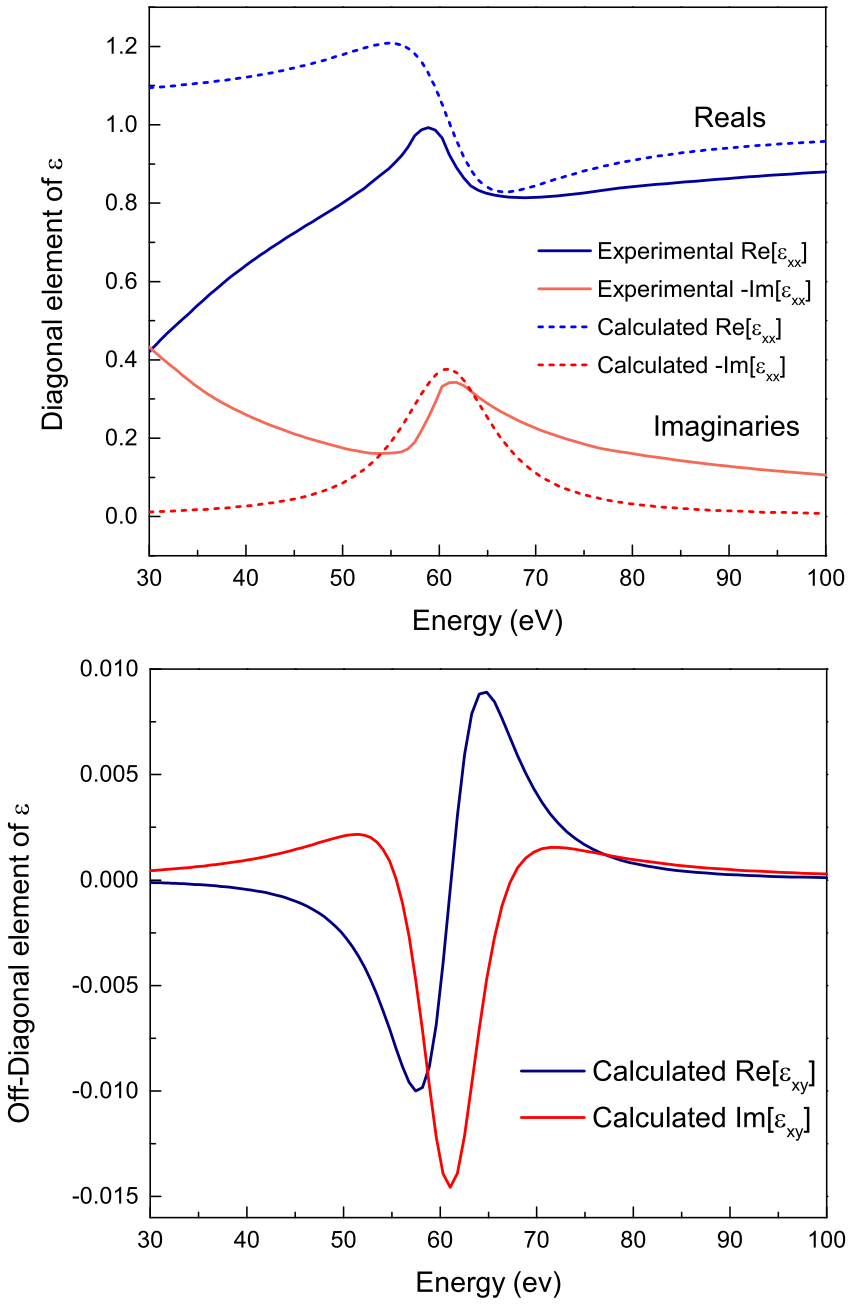


Figure 2.9: Calculations of the dielectric tensor using a classical model for cobalt at the M absorption edge. (Top) $\Gamma$ and $\omega_0$ values are fit by using the tabulated values of the refractive index [32] then plotting the fitted and tabulated values of the diagonal element of $\hat{\epsilon}$. (Bottom) Then, fitted values and Equation 2.56 are used to calculate and plot the off-diagonal element of $\hat{\epsilon}$ as a function of energy .

$$\sigma_{\alpha\beta} = -\frac{ie^2}{m^2\hbar V} \sum_{nn'} \frac{f(\epsilon_n) - f(\epsilon_{n'})}{\omega_{nn'}} \frac{\prod^{\alpha}_{n'n} \prod^{\beta}_{nn'}}{\omega - \omega_{nn'} + i/\tau}, \tag{2.58}$$

where $\alpha$ and $\beta$ are coordinates, $\hbar$ is Plank's constant, $f(\epsilon_n)$ is the Fermi function, $\omega_{nn'}$ is the energy difference between states, i.e. $\hbar\omega_{nn'} = \epsilon_{n'} - \epsilon_n$, $\tau$ is a term for the finite lifetime, and $\prod$'s are optical-transition matrix elements. These elements are complicated part of this calculation because of many possible available states in a large k-momentum space [56, 25, 10].

The conductivity tensor of a material can be calculated by the Equation 2.58 once the required properties are known; however, one has to be careful whit this calculation, making sure that

- accurate wave functions and band energies are determined with local spin-density approximation,
- the use of spin-density functional theory gives the correct description of exchange energy,
- one has relativistic spin-orbit interactions.

One important property of the conductivity tensor is the Kramers-Kronig (KK) relation. The KK relation is a useful technique for calculating the absorptive and dispersive parts of dielectric tensor or extracting the conductivity tensor at an unknown region of a spectrum. The KK relation is originating from causality principal of physics that the response of a material, i.e., the conductivity can not precede the incident impulse [56]. If I define the conductivity tensor as $\sigma_{\alpha\beta} = \sigma^{(1)}_{\alpha\beta} + i\sigma^{(2)}_{\alpha\beta}$, the relation between them is

$$\sigma^{(1)}_{\alpha\beta}(\omega) = \frac{2}{\pi}\wp \int_0^{\infty} \frac{\omega'\sigma^{(2)}_{\alpha\beta}(\omega)}{\omega'^2 - \omega^2} d\omega', \tag{2.59}$$

$$\sigma^{(2)}_{\alpha\beta}(\omega) = -\frac{2\omega}{\pi}\wp \int_0^{\infty} \frac{\sigma^{(2)}_{\alpha\beta}(\omega)}{\omega'^2 - \omega^2} d\omega', \tag{2.60}$$

where $\wp$ is the principal value.

My derivations and formalism may appear abstract. However, one can understand the microscopic picture in terms of an optical transition, as showed in Figure 2.10. A typical band structure (electron configuration) of a transition ferromagnet, such as Fe, Ni and Co is shown. At the Fermi

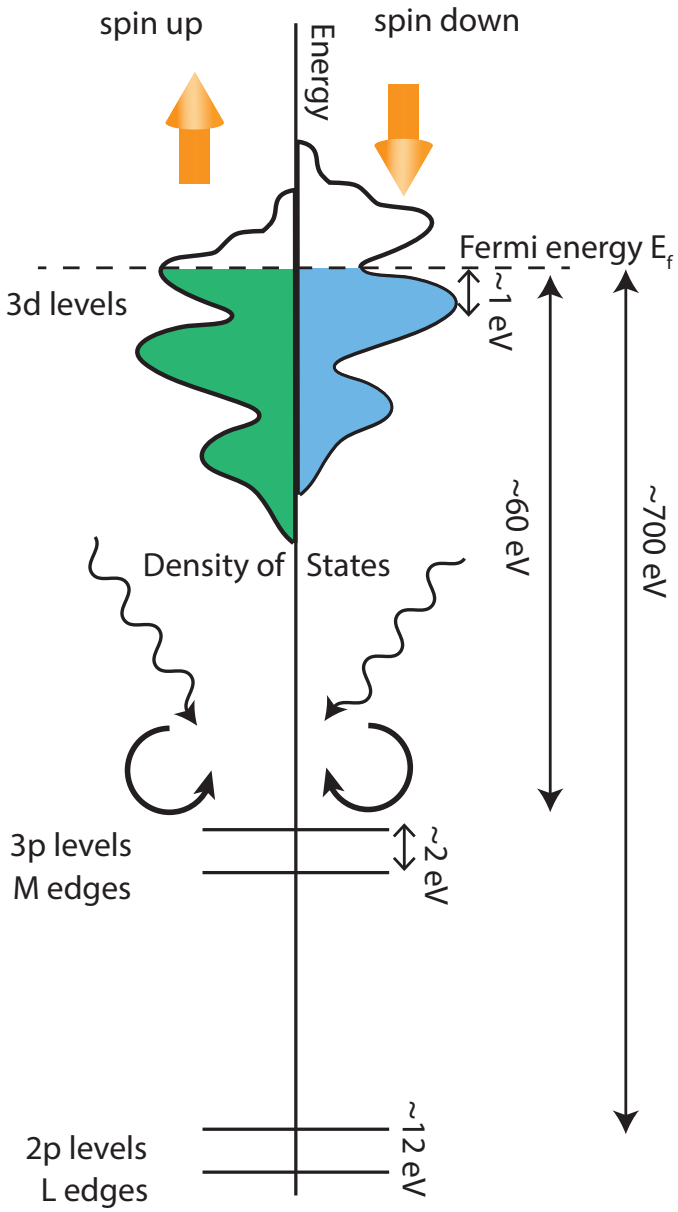


Figure 2.10: Microscopic picture of MO effect. The electronic structure is shown for a typical transition metal ferromagnet with L and M core levels and a $3d$ conduction band. The magnetic moment of the material comes from the exchange splitting of spin-up and spin-down electrons that results in an unequal occupation shown in green and blue. An incoming circularly polarized x-ray photon excites an electron from the core level to an unoccupied $3d$ state. The excitation probability for spin-up and spin-down electrons is directly dependent on the chirality of the incoming x-ray. By reversing the chirality or the direction of magnetization, an asymmetry appears in the absorption known as XMCD. This phenomenon is still true for linear polarized light because the linearly polarized light is a combination of left and right circularly polarized light. Magnetic contrast is reflected or transmitted via x-ray photons.

level, the highest energy level of an occupied electron, the spin-up and spin-down electrons are split by the exchange energy, which is approximately 1 eV. The number of electrons in the spin-up (majority) electron channel is greater than in the spin-down (minority) electron channel. The imbalance in these channel occupations results in a net magnetic moment. Furthermore, the other two core levels shown by M and L edges are more localized. However, they are also split by spin-orbit and exchange interactions. When an x-ray photon at the resonance frequency excites an electron from a core level to a 3d unoccupied state, the spin of the excited electron does not change. Hence, the absorption of an incoming x-ray excitation depends on its polarization. By reversing the magnetization or the chirality one can get an asymmetry in the absorption or transmission of an x-ray [78].

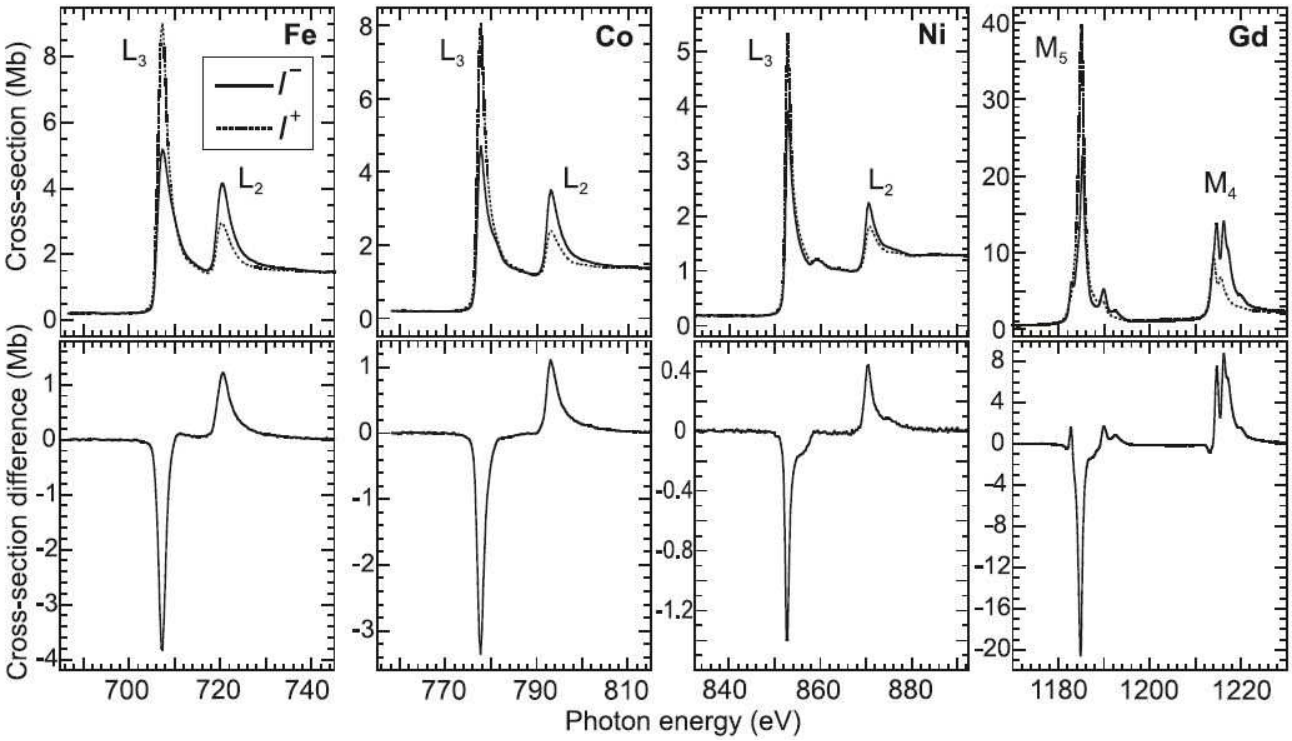


Figure 2.11: Experimental XMCD spectra taken from [78]. Transition metals Fe, Co and Ni have a strong contrast at the L edge via 2p→3d excitation. The magnetic moment of Gd comes from 4f electrons with a different principal quantum number that shows larger but complicated, contrast at the M edge. Because spin-orbit splitting at the $L$ edge is approximately 12 eV, the XMCD spectra for $L_2$ and $L_3$ have opposite signs and different magnitudes.

Next, I show some experimental XMCD spectra in Figure 2.11 [78]. For the transition metals Fe, Co, and Ni, the XMCD has two distinct peaks coming from the $L_2$ and $L_3$ edges. Because of spin-orbit splitting, the sign of the peaks are different. The energy difference between them is approximately 12 eV. The height of these peaks is related to the magnetic moment of the material. For example, Fe has the highest magnetic moment and its peak amplitudes also are the highest. While L-edge spectra is shown for Fe, Ni and Co, Gd has XMCD contrast at the M edge because its principal quantum number is different, and its magnetic moment results from exchange splitting of 4f electrons.

## 2.7 Conclusion

The magneto-optical effect is a powerful technique for understanding complicated band structures and electronic properties of magnetic materials. There are many different geometries employing the MO effect. I focus on the T-MOKE at reflection mode and the XMCD at transmission mode by starting with Maxwell's equations in a magnetic material. In addition, I explore more about the T-MOKE of multilayer systems with the Fresnel-based full-matrix method, which is more closely related to the main focus of this thesis. Then, I explain the origin of the MO effect by a classical macroscopic and quantum microscopic models by introducing the conductivity tensor. In the following chapters, I show my experimental setups and findings with T-MOKE geometry for thin-film and multilayer ferromagnets.

# Chapter 3

# Experimental Setup

## 3.1 Introduction

In this chapter, I will introduce the experimental setup for studying element-selective ultrafast magnetization dynamics. This setup shown in Figure 3.1 has four main parts: (1) high harmonic generation for probing, (2) the pump part for excitation, (3) the grating sample and spectrometer, and (4) other components. I will elaborate on each main part in following sections.

First, I will give a physical picture behind the X-ray source, which is high-harmonic generation. Second, I will explain the excitation part of the experiment, which is an infrared pump, by calculating some absorption properties of our samples. Third, I will describe some properties of the samples that also work as a spectrometer. Finally, other equipment in the setup is introduced including chamber, magnet, toroidal mirror, and camera.

To better understand all the parts of the experiment, I will briefly introduce the laser system used in our pump-probe experiments. We start with a standard modelocked Ti-Sapphire oscillator that generates ultrashort low-energy pulses at a 80 MHz repetition rate. These low energy pulses enter into standard cryo-cooled Ti-Sapphire amplifier section, reaching a 2 mJ pulse energy at a 2 kHz repetition rate. The spectral bandwidth of the pulse is around 80 nm at full-width-at-half-maximum at a 790 nm central wavelength, which gives approximately 25 fs pulse duration. We split the beam in two parts, i.e. the pump and probe parts. While the low-energy beam is used as a pump beam, shown in Figure 3.1; the high-energy beam is focused into a hollow waveguide filled with a noble gas; this is where high-harmonic generation occurs.

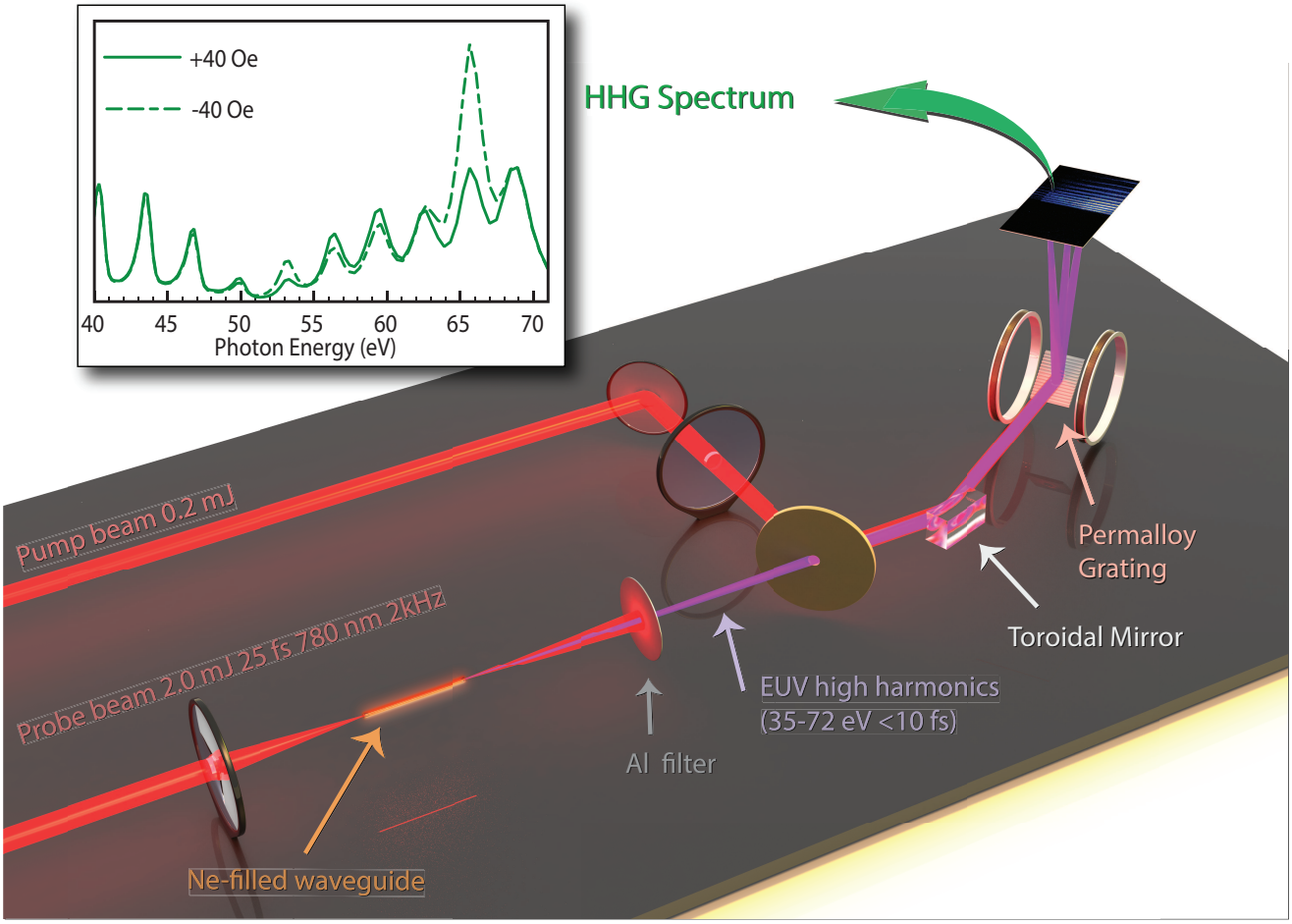


Figure 3.1: Experimental setup for studying element-selective ultrafast magnetization dynamics. There are four main parts in the setup: the high-harmonic-generation probe arm, the infrared pump arm, grating sample spectrometer and other components. The ultrashort laser pulse is split into two. Ninety percent of the energy is focused into a hollow waveguide filled with neon gas; this is where high-harmonic generation happens. After the waveguide, an aluminium filter blocks the fundamental beam and passes through x-rays with energies between 35 and 72 eV (cutoff energy of aluminium filter at 72 eV.) This region of spectrum is called the extreme ultraviolet (EUV). Ten percent of the rest of the beam is used as a pump to excite the magnetic sample. Both the pump and probe beams are focused by a gold-capped toroidal mirror onto the sample and the CCD camera, respectively. The sample is fabricated as a grating to disperse EUV photons spectrally on the CCD camera. There are two additional Al filters after the sample to block the pump beam and ensure that we have only EUV photons at the CCD camera. Because of dispersion, each harmonics is detected by the camera as shown in inset graph. By reversing the magnetization of the sample, we can very the reflected EUV intensity, as shown by the solid and dashed green curves for a Permalloy sample (alloy of Ni and Fe).

## 3.2 High Harmonic Generation–Probe

One of the most important aspects of this work is the unique experimental setup. To our knowledge, there is no working duplicate of this technique. The central feature of this technique is the source of high-harmonic generation (HHG). Using this highly nonlinear process of HHG, we can produce ultrashort pulses with photon energies spanning from the VUV to the x-ray regions of the electromagnetic spectrum [60, 20, 61]. This non-linearity is possible by focusing an ultrashort infrared pulse into a gas medium. By choosing the right parameters of the driving laser and the medium, one can reach even the $5000^{th}$ upconversion and photon energies above keV [60]. Because of this enormous non-linearity, we can not treat HHG with a perturbative method like high orders of susceptibility of the medium. Usually, a semiclassical approach of a non-perturbative three-step model is used to describe HHG (Figure 3.2). In the three step model, an electron undergoes three critical steps that are driven by the strong electric field of the pulse. Figure 3.2 briefly shows these three steps: Tunneling, acceleration-free propagation, and recombination. In the tunneling process, the strong electric field modifies the Coulomb potential, and the electron tunnels through the energy barrier via ionization. In the acceleration regime, the electric field modulates the tunneled electron, which gains significant kinetic energy. In the final recombination step, the electric field brings back the electron that then recombines with the atom, which radiates an x-ray photon to release its excess energy [79]. Next, I give more detail about these steps.

An ultrashort pulse allows us to access a strong electric field comparable to the Coulomb field inside the atom. The distortion of the potential of the atom is significant, and it creates an energy barrier. The last electron of the atom can tunnel away from this barrier, and the tunneling rate is only possible quantum mechanically as described by Ammosov-Delone-Krainov (ADK) [80]. The ionization rate increases by increasing the laser intensity, and above a threshold the gas medium becomes over-ionized, which reduces the efficiency of HHG. More detailed investigation about ionization can be found in [61, 19, 74].

After the tunneling and ionization process, the electron is assumed to have zero velocity and

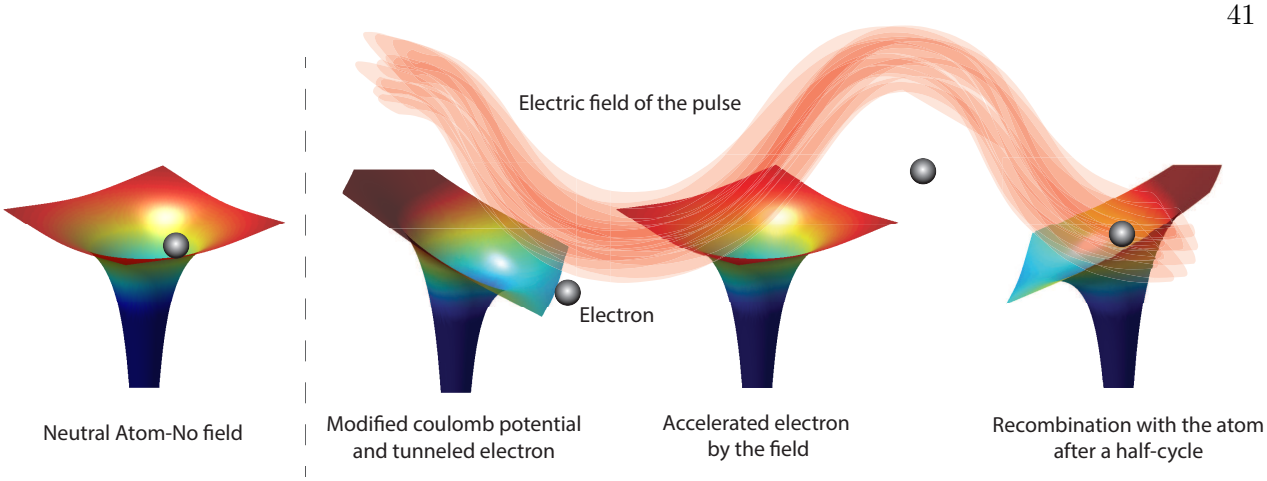


Figure 3.2: Semiclassical approach to high-harmonic generation, the three-step model. Without an electric field, the atom is neutral, and the electron is behaving as usual. When we apply an ultrashort light pulse, the electric field of the pulse is very strong and modifies the Coulomb potential significantly. Then electron tunnels in the first step. Second, the electric field accelerates the electron, giving it kinetic energy. Finally, after a half cycle through the electric field, the electron recombines with its parent atom and radiates its extra kinetic energy as a x-ray photon.

it propagates by the electric field of the pulse. This propagation is purely classical and can be described by

$$m\ddot{x} = -eE\cos(\omega t + \phi), \tag{3.1}$$

where $m$ is the mass of the electron, $x$ is the position of the electron, $\omega$ is the frequency of driving laser, and $\phi$ is the phase at the moment that is crucial for gaining energy. By using the equation of motion, one can find the displacement and the velocity of the electron as a function of time and phase by

$$x(t,\phi) = \frac{eE}{m\omega^2}\left[-\cos\phi + \cos\omega t\cos\phi + t\omega\sin\phi - \sin\omega t\sin\phi\right], \text{and} \tag{3.2}$$

$$v(t,\phi) = \frac{eE}{m\omega}\left[-\cos\phi\sin\omega t + \sin\phi - \cos\omega t\sin\phi\right]. \tag{3.3}$$

By using above equations, I show typical electron trajectories $x(t,\phi)$ and returning kinetic energy of the electron, Figure 3.3. In the top graph, I plot four different trajectories for the phases of 0, $0.1\pi$, $0.2\pi$ and $0.4\pi$. The electron returns to the atom at different times and with different velocities for each of the phases, which are determined by the moment of tunneling. Also the

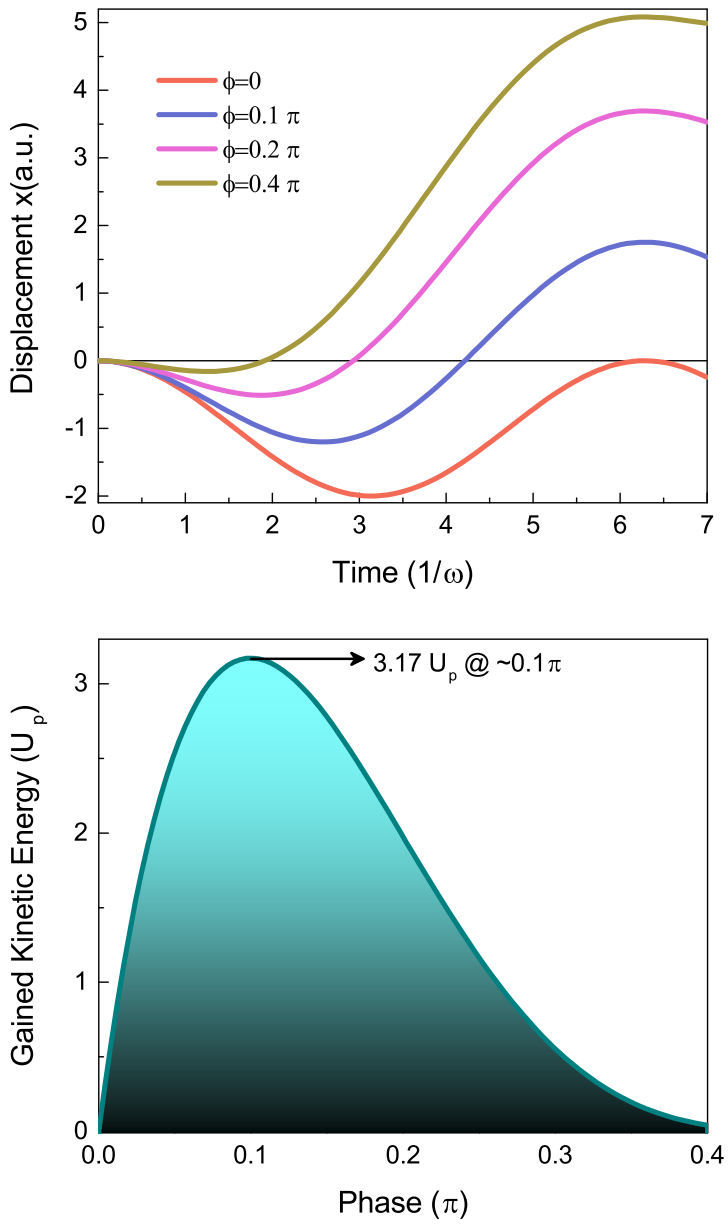


Figure 3.3: Example trajectories of the electron in free propagation and maximum-recombined kinetic energy. (Top) The electron has zero velocity at time zero, and it accelerates with $\frac{-eE}{m}\cos(\omega t + \phi)$. The electron displacement is shown for phase values 0, $0.1\pi$, $0.2\pi$, and $0.4\pi$. The electron can return to the atom, where the black line crosses the curves, only in a certain phase range and with a specific kinetic energy for each phase. (Bottom) The gained kinetic energy is shown as a function of phase. When the electron returns to the atom, its kinetic energy strongly depends on the phase of the electric field, which means that the time when the electron tunnels away determines its kinetic energy. The maximum-returning kinetic energy is found 3.17 $U_p$, where $U_p$ is known as the pondermotive energy. Hence, the maximum-returning energy determines the cutoff energy for high harmonics as $\hbar\omega = I_p + 3.17\ U_p$, where $I_p$ is the ionization energy of the gas.

electron can return to the atom only with a phase between $0 < \phi < \pi/2$; otherwise the laser filed pulls the electron completely out of the atom. The radiated photon energy is directly dependent on the returning kinetic energy of electron. To find the cutoff, or maximum, frequency of the x-rays, I first find the return time of the electron to the atom for each frequency from 0 to $0.4\pi$. Then, I calculate the kinetic energy with

$$\frac{1}{2}mv^2 \;=\; \frac{e^2E_0^2}{4m\omega^2}(2\dot{x}^2), \tag{3.4}$$

where $\frac{e^2E_0^2}{4m\omega^2}$ is known as the pondermotive energy of the field $U_p$. From the bottom graph of Figure 3.3, the maximum-gained kinetic energy becomes 3.17 $U_p$ when $\phi = 0.1\ \pi$. This gives the cutoff frequency of high-harmonics as

$$\hbar\omega_{cutoff} \;=\; I_p + 3.17\ U_p, \tag{3.5}$$

where $I_p$ is the ionization energy of the gas. The final recombination process makes the electron release its energy via x-ray radiation. Equation 3.5 reveals three important parameters in the HHG process:

- $I_p$ ionization energy: By choosing simple noble gases, such as helium or argon, the cutoff frequency can be tuned.
- $|E_0^2|$ laser intensity: Having shorter pulses and increasing the pulse power give higher cutoff energies. But, one must be careful not to over-ionize the gas medium, which decreases the HHG efficiency.
- $\omega$ laser frequency: The wavelength of the driving laser actually gives more flexibility for the cutoff energy ($\propto \lambda^2$) than above two parameters. By using longer wavelengths, one can generate soft x-rays [60].

The wavelength dependence of the cutoff frequency is being studied to push the limits of HHG. Being able to generate hard x-rays with a tabletop setup will open limitless opportunities for imaging and spectroscopy experiments with femtosecond-temporal resolution. In Figure 3.4, I show the largest coherent x-ray spectrum reached by high-harmonic generation via a 3.9 $\mu m$ laser. By using longer

wavelengths for driving HHG, one can reach the L absorption edge of transient ferromagnets and elevate our understanding of ultrafast magnetization dynamics [60].

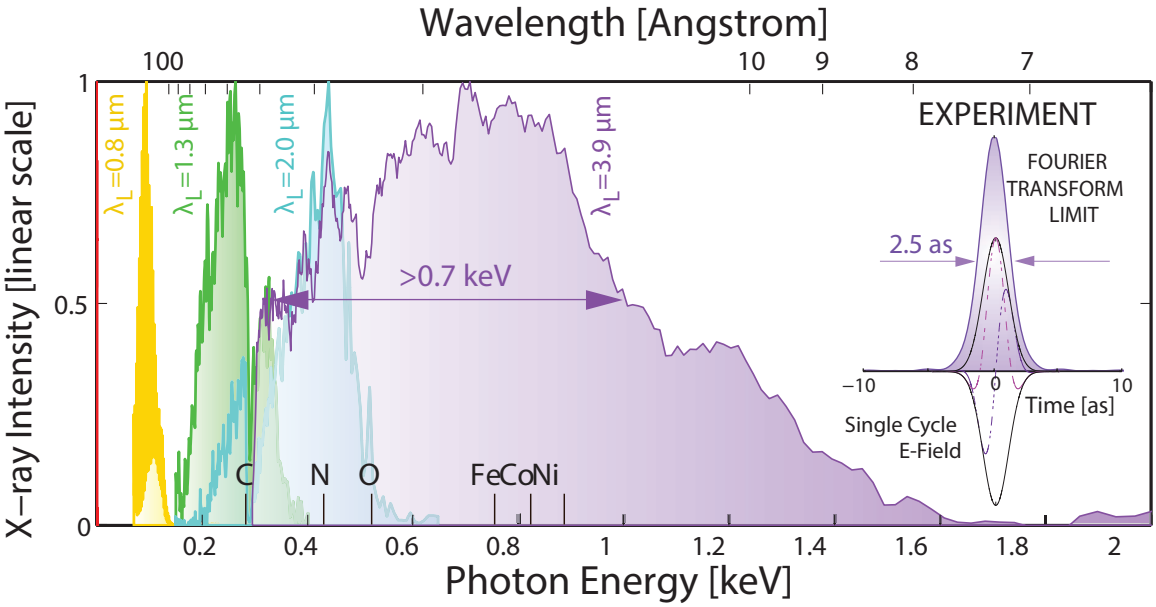


Figure 3.4: Extension of the cutoff energy of HHG by using longer-wavelength driving lasers. The cutoff frequency has $\propto \lambda^2$ proportionality with the wavelength. Four spectra are shown for four different laser wavelength, i.e., 0.8, 1.3, 2, and 4 $\mu m$. The graph is taken from [60].

### 3.2.1 Phase Matching

While pushing the cutoff energy of HHG to the hard x-ray limit, having a sufficient number of x-ray photons is important for time-resolved experiments. In order to have sufficient x-ray photons, the macroscopic picture of HHG should be understood as well. In general, there are two major techniques for performing HHG: (1) tight focusing in a gas jet, and (2) coupling into a gas-filled hollow fiber. In my research group, we are the experts on creating x-rays with the second method. Although coupling in a fiber has some complications, such as alignment and stability, the HHG process in a fiber actually can be made very efficient by matching the phases of the x-ray photons and the driving laser. This phase matching is a well-known phenomena for second or third harmonic generations in solid state media. The physics is similar: In both, the velocities of the fundamental laser light and generated high orders must be equal to ensure that high harmonics

interfere constructively [75].

This phase difference between a harmonic and the fundamental $\Delta k = k_{laser} - k_{harmonics}$ is expressed by

$$\Delta k \approx \ N \left( \frac{u_{11}^2 \lambda}{4\pi a^2} - P(1-\eta)\frac{2\pi}{\lambda}(\Delta\delta + n_2) + P\eta n_a r_e \lambda \right), \tag{3.6}$$

where N is the order of harmonics, $\lambda$ is the wavelength of the laser, $a$ is the diameter of the fiber, $u_{11}$ is the first zero of the Bessel function, $P$ is the pressure, $\eta$ is the ionization fraction, $n_2$ is the nonlinear index of refraction, $n_a$ is the number density of atoms, $r_e$ is the classical electron radius, and $\Delta\delta$ is the difference between the refractive indices of the fundamental laser and the harmonics. There are two important sources experimentally accessible for certain laser parameters: (1) the fiber geometry, and (2) the pressure of the gas. In my experiment, the diameter of the fiber is 150 $\mu m$ and the pressure at the gauge is around 700 torr. These values definitely depend on the vacuum system and the geometry of how the fiber is mounted.

To sum up HHG:

- HHG is a great tool for accessing x-ray photons on a tabletop setup.
- The three-step model is a semiclassical description of HHG that is successful at determining the cutoff frequency.
- A macroscopic understanding of HHG is as important as the microscopic understanding. The phase-matching process is critical for having sufficient x-ray photons for applications with good statistics.

## 3.3 Excitation-Pump

Most of the energy of the initial laser pulse is used for HHG, and 10% of the pulse with 0.2 mJ pulse energy is used to optically excite the magnetic systems. The length of the pulse is approximately 25 fs, and it is immediately absorbed by the electronic system in the magnetic sample. Indeed, this excitation and absorption in each layer are important to understand demagnetization

processes. Here, I to examine important parameters and physical effects in absorption by a magnetic multilayer structure.

I start with a Maxwell's equation similar to Equation 2.4.

$$\mathbf{J} \cdot \mathbf{E} \;=\; \mathbf{E} \cdot (\nabla \times \mathbf{H}) - \mathbf{E} \cdot \frac{\partial \mathbf{D}}{\partial t}. \tag{3.7}$$

By using a vector identity and rearranging, the above equation becomes

$$\frac{\partial U}{\partial t} + \nabla \cdot \mathbf{S} \;=\; -\mathbf{J} \cdot \mathbf{E}, \tag{3.8}$$

where $U$ and $\mathbf{S}$ are defined as

$$U \;=\; \frac{1}{2}(\mathbf{E} \cdot \mathbf{D} + \mathbf{B} \cdot \mathbf{H}), \tag{3.9}$$

$$\mathbf{S} \;=\; \mathbf{E} \times \mathbf{H}. \tag{3.10}$$

The scalar $U$ is stands for the energy density of the electromagnetic wave (emw), and the vector $\mathbf{S}$ is called Poynting's vector and represents energy flux. Equation 3.8 describes the conservation of energy of an emw, and it is known as Poynting's theorem. The above equations are written for any point of time. After taking the time average of a sinusoidal emw, Poynting's vector reads

$$\mathbf{S} \;=\; \frac{1}{2} Re[\mathbf{E} \times \mathbf{H}^*], \tag{3.11}$$

where $\mathbf{H}^*$ means a complex conjugate [59].

By using Equation 3.9, the intensity of an emw in a media written as

$$I = cn\epsilon_0 |E|^2/2. \tag{3.12}$$

This intensity formula is used to explain absorption in a lossy medium. For semi-infinite systems or materials with thick layers, both the intensity formula and Poynting's vector give the same result. However, they can significantly differ. For instance, the intensity formula turns invalid for thin multilayers because of strong backward-propagating waves (the explanation of this

difference and any concept confusion on intensity and Poynting's vector can be found in Appendix C.)

Next I show two different approaches to calculating the absorption of the infrared beam. The first method requires less computational technique. It uses the full matrix method to find electric fields at the interfaces and changes in the absolute values of these electric fields to determine the absorption. In the second method, I use more complex software known as the Finite Difference Time Domain (FDTD) program, and this calculation gives the whole depth profile of the Poynting's vector. Using the second method, I find the electric and magnetic fields at the every point in the sample via Maxwell's equations and boundary conditions; then to calculate Poynting's vector with Equation 3.11 for the whole sample.

In the first method, I introduce a zero-thickness vacuum layer between each layer to simplify the calculation. I find the electric fields in these pseudo vacuum layers and calculate the changes from one layer to another. Figure 3.5 illustrates this method. To calculate the absorption in the $n^{th}$ layer, for example, I need forward-propagating $E_{n+}$ and $E_{(n+1)+}$, as well as backward-propagating $E_{n-}$ and $E_{(n+1)-}$ fields. Then, intensity changes in these waves in both directions give the amount of the absorbed energy by the $n^{th}$ layer, i.e., $\frac{1}{2}(|E_{n+}|^2 - |E_{(n+1)+}|^2 + |E_{(n+1)-}|^2 - |E_{n-}|^2)$. If one uses Equation 3.12 to calculate the absorption profile as a function of the depth, then the result is not correct because of many thin layers and strong backward propagating waves. To find the correct absorption profile as a function of the depth, one must use Poynting's vector in Equation 3.11. Here, I use a trick that allows me to use the intensity formula and calculate the absorption in each layer instead of a whole depth profile.

Next, I give one example calculation of the multilayer structure studied in [83]. This multilayer structure consists of substrate/Ta(3 nm)/Fe(4 nm)/Ru(1.7 nm)/Ni(5 nm)/$Si_3N_4$(1.2 nm)/grating/air. As shown in Figure 3.1, the incidence photon has a wavelength of 800 nm and an angle of 45° with the normal of the surface. After writing all dynamics and propagation matrices for these experimental conditions, the reflected, transmitted and absorbed intensities become 39%, 11%, and 50% of the incoming s-polarized pump beam, respectively. Then, I find the electric fields

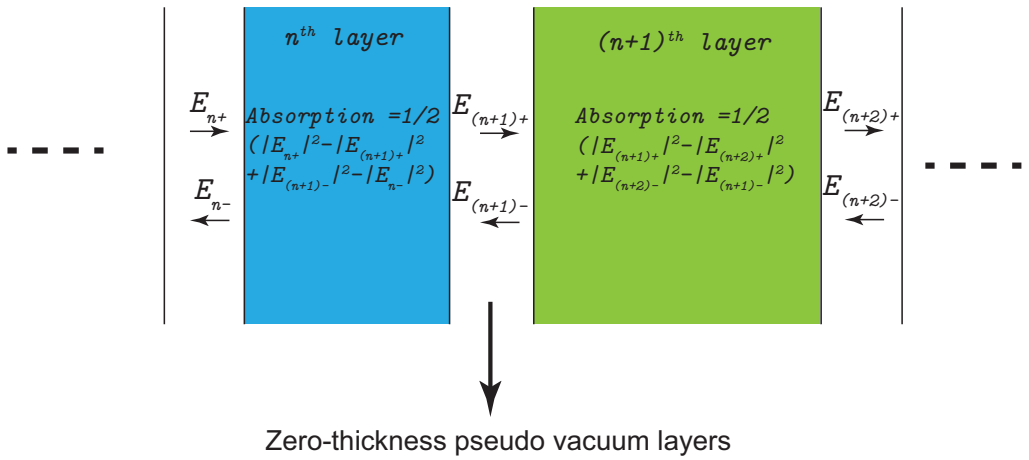


Figure 3.5: Full matrix calculation method for absorption in multilayers. I simplify the calculations by introducing a zero-thickness vacuum layer between each layer. After finding the electric fields in these vacuum layers, the absorbed intensity is nothing but the differences in the electric fields. For example, the absorbed light in the $n^{th}$ layer turns into $\frac{1}{2}(|E_{n+}|^2-|E_{(n+1)+}|^2+|E_{(n+1)-}|^2-|E_{n-}|^2)$.

in the pseudo vacuum layers, i.e., $Si_3N_4$ - Ni $\rightarrow$ Layer1, Ni - Ru $\rightarrow$ Layer2, Ru - Fe $\rightarrow$ Layer3, Fe - Ta $\rightarrow$ Layer4, Ta - $SiO_2$ $\rightarrow$ Layer5. By using these electric fields, I find the absorbed intensity in each layer as in Table 3.1.

Table 3.1: Absorbed intensity in each layer in terms of percentile of the incoming pump beam by the full-matrix method.

| Layer | Absorbed intensity % of the incoming beam | % ratio of the total absorption |
|---|---|---|
| Ni | 18.9 | 38.0 |
| Ru | 11.5 | 23.1 |
| Fe | 15.5 | 31.1 |
| Ta | 3.9 | 7.8 |

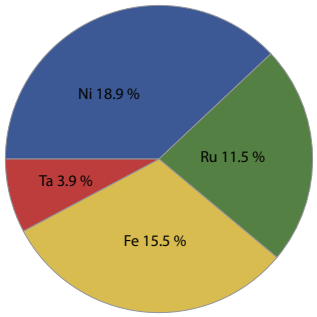

Next, I compare these absorption results with FDTD simulation results. Furthermore, I add the effect of the grating on the absorption of the pump beam with FDTD method. I show the results of two simulations for the same multilayer sample with and without the grating in Table 3.2. I first begin the sample without the grating as in the first method.

The first multilayer sample is built as shown in Figure 3.6. All fields are calculated by solving Maxwell's equations and boundary conditions. The required space for the calculation is $2 \times 1\ \mu m$. The thickness is very large compared to the sample in the $z - axis$ because of the long wavelength of pump, but very small in the $xy$-plane because of an infinite-periodic structure. After finding all fields, I calculate the Poynting's vector in $z$ direction using Equation 3.11. After normalizing by the value at the top of the sample, I show the results in Figure 3.6. The total reflected, transmitted, and absorbed intensities are found 39.6%, 10.7% and 49.8%, respectively. I also show how much the normalized Poynting's vector changes at the interfaces. Poynting's vector at the top of the sample is the sum of the absorbed and transmitted intensities; the absorbed intensities in the individual layers Ni, Ru, Fe, and Ta are found 18.5%, 12.3%,15.5% and 3.8%, respectively. As we have already seen, the results obtained with the method 2 agree very well with Table 3.1.

Next, I explore the effect of the grating in absorption calculations. I add a 10 nm-thick, 1 $\mu m$-wide $Si_3N_4$ layer on the top of the sample. I show this new sample in the top of Figure 3.7. Additionally, I plot the 2-dimensional profile of Poynting's vector of whole the structure (c) and focus on the sample (b). One can see the effect of the grating by comparing the middle region of the plot (b). Then, I average this 2-dimensional profile through the $x$-axis and show the results in (d). The total absorption is a little more than the one without grating. I use the total transmitted and absorbed intensities and find the absorption in each individual layer. These results are shown in Table 3.2 for two samples. There are no big differences between two samples because the grating thickness is relatively small compared to the pump wavelength.

Because of the negligible effect of the grating, I now discuss the relative absorption ratio of Ni and Fe layers that matter for magnetization dynamics. If I calculate the absorption per sample thickness, Fe has $15.7/4 \rightarrow 3.9\%$ and Ni has $19/5 \rightarrow 3.8$ % absorption of the incoming pump per

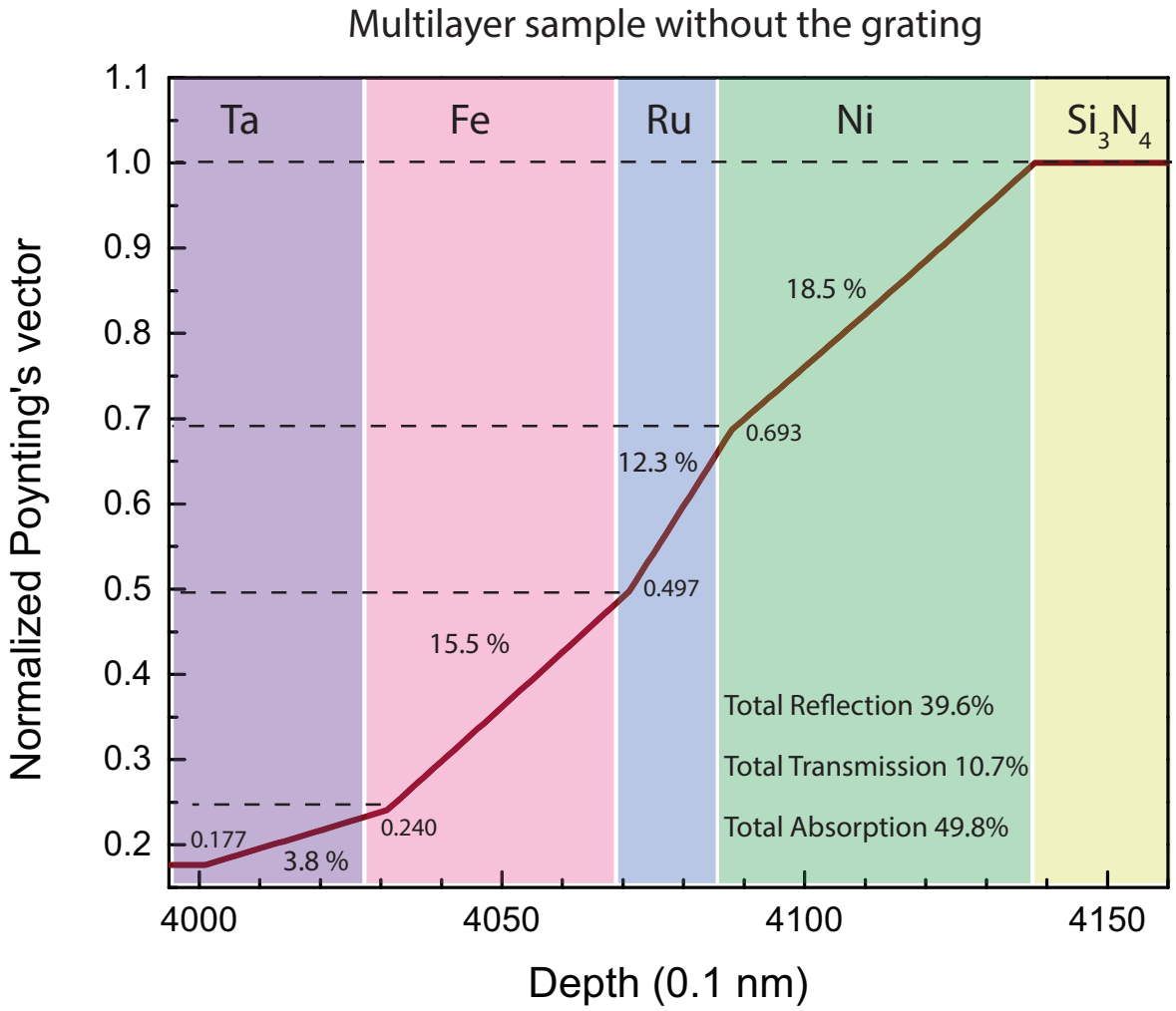


Figure 3.6: Poynting's vector-depth profile of an example multilayer structure. The multilayer structure is consist of substrate $SiO_2$/Ta(3 nm)/Fe(4 nm)/Ru(1.7 nm)/Ni(5 nm)/$Si_3N_4$(1.2 nm)/air. One can expect an exponential type of decay in layers, but the thicknesses of layers are much smaller than the wavelength of the pump and decay of a Poynting's vector in a multilayer is more complicated than a regular exponential decay. Total reflected, transmitted and absorbed intensities are 39.6%, 10.7% and 49.8%, respectively. Furthermore, individual absorptions are 18.5%, 12.3%, 15.5% and 3.8% for Ni, Ru, Fe and Ta layers, respectively. These ratios are in very good agreement with Table 3.1

nanometer. Therefore, the absorption densities are about same for the Fe and Ni layers, which means that there is no excitation gradient in the multilayer sample. This is an important fact in analyzing the demagnetization amounts or electron temperatures in individual magnetic layers.

Table 3.2: Absorbed intensity in each layer in terms of percentile of the incoming pump beam for two samples by FDTD method shown in Figures 3.6 and 3.7.

| Layer | Absorbed intensity without grating | Absorbed intensity with grating |
|---|---|---|
| Ni | 18.5 | 19.4 |
| Ru | 12.3 | 11.8 |
| Fe | 15.5 | 15.9 |
| Ta | 3.8 | 4.0 |

To conclude this section, I discuss the ultrafast laser excitation in the experiment to initiate electron dynamics in a magnetic multilayers. I review how these multilayers absorb infrared photons layer by layer. I calculate absorption ratios of the incoming pump beam by layers using an example sample via two different methods. Moreover, I find the depth profile of the Poynting's vector by FDTD-method simulations and find a negligible effect of the grating in absorption. Finally, I mention nonexisting excitation gradient in multilayer samples that helps in discussion of demagnetization dynamics in the following chapters.

## 3.4 Other Components

In this section, I introduce other essential experimental components. I show the overall picture of the setup in Figure 3.8. I have already introduced the laser system that is shown in the black box with cryogenic cooling. After the amplifier, the beam is in the box because of stability and safety considerations.

Before the HHG capillary waveguide, I focus the beam with a lens and put the beam in the vacuum system with a thin window. Meanwhile, the pump beam is delayed with an Aerotech translational stage and taken into the vacuum system with another window. The toroidal mirror focuses the pump beam on the sample and the probe EUV beam on the camera. Furthermore,

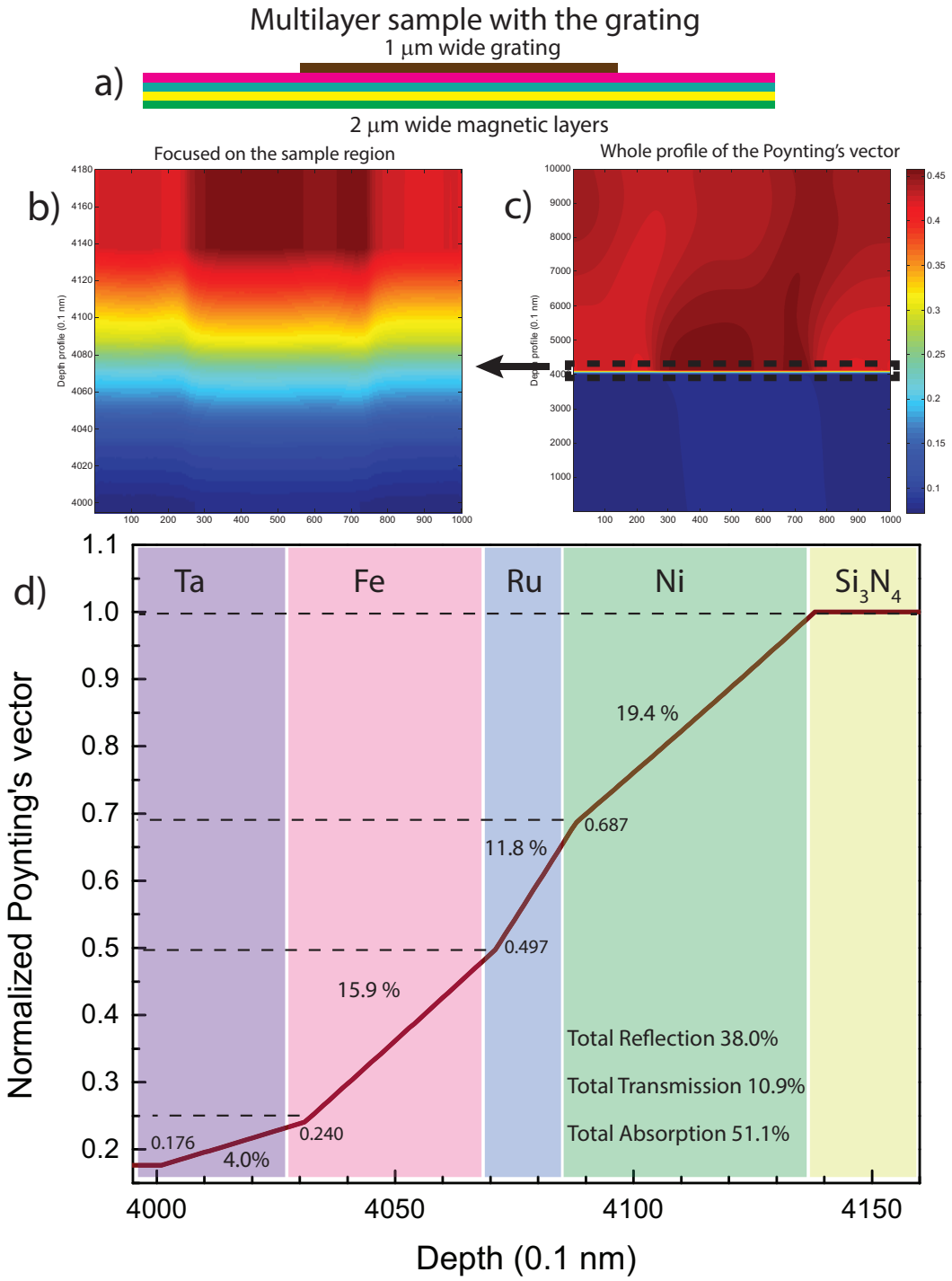


Figure 3.7: Depth profile of Poynting's vector for a grating sample. (a) In the simulation, I use 2 $\mu m$ wide magnetic layers and 1 $\mu m$ wide $Si_3N_4$ 10 nm height gratings. (b) and (c) show the 2-dimensional profile of the Poynting's vector and the negligible effect of the grating in absorption. One can see small variations at the edges of the grating; however, the individual absorptions in layers do not change. (d) The ratios become 19.4%, 11.8%, 15.9% and 4.0% for Ni, Ru, Fe, and Ta layers, respectively.

the aluminum filters block all remaining infrared beams not to destroy the signal. The iron-yoke magnet is used to manipulate the magnetic field on the sample to employ Kerr effect. The sample is in a small cube chamber at a 45° angle of incidence. Finally, an Andor EUV-charge coupled device (CCD) camera record the reflected intensities of EUV photons.

I show the illustration of the yoke in Figure 3.9 including the coil and sample holder [47, 45]. The coil has 300 Cu wire turns, and it can handle a 10-A current with water cooling. The iron-yoke carries the magnetic flux and focuses on the sample holder made of titanium. The magnetic field on the sample is given by

$$H_{gap} = \frac{NI}{l_{gap} + L\frac{A_{gap}}{A_{core}}\frac{1}{\mu_{core}}}, \tag{3.13}$$

where $N$ is the number of wire turns, $I$ is the current in the wire, $l_{gap}$ is the width of the gap, $L$ is the total length of the iron yoke, $A_{gap}$ and $A_{core}$ are the total area of the gap and the core respectively, and $\mu_{core}$ is the permeability of the iron core. Because of all the losses and disorders at the corners, the magnetic field measured at the gap is 500 Oe, instead of the theoretical predicted 3800 Oe. We introduce the iron-yoke with the sample holder into the sample chamber with $\frac{1}{2}'$ ultratorr feedthroughs.

## 3.5 Sample Spectrometer

In this section, I introduce the grating sample geometry that is used as a spectrometer. This design allows us to remove one experimental component and gives us a better signal-to-noise ratio. I show an illustration of the reflection of a light from a grating sample and an AFM image of one sample in Figure 3.10. Basically, there are two different types of samples. For simple samples, such as pure elements or alloys of two ferromagnets, we fabricate the magnetic samples as a grating on a substrate. On the other hand, for complex multilayer samples, we deposit the magnetic layers as thin films on a substrate and pattern the $Si_3N_4$ grating with a 2 $\mu m$ period. Both types work similarly to diffract the EUV photons constructively onto the CCD camera like

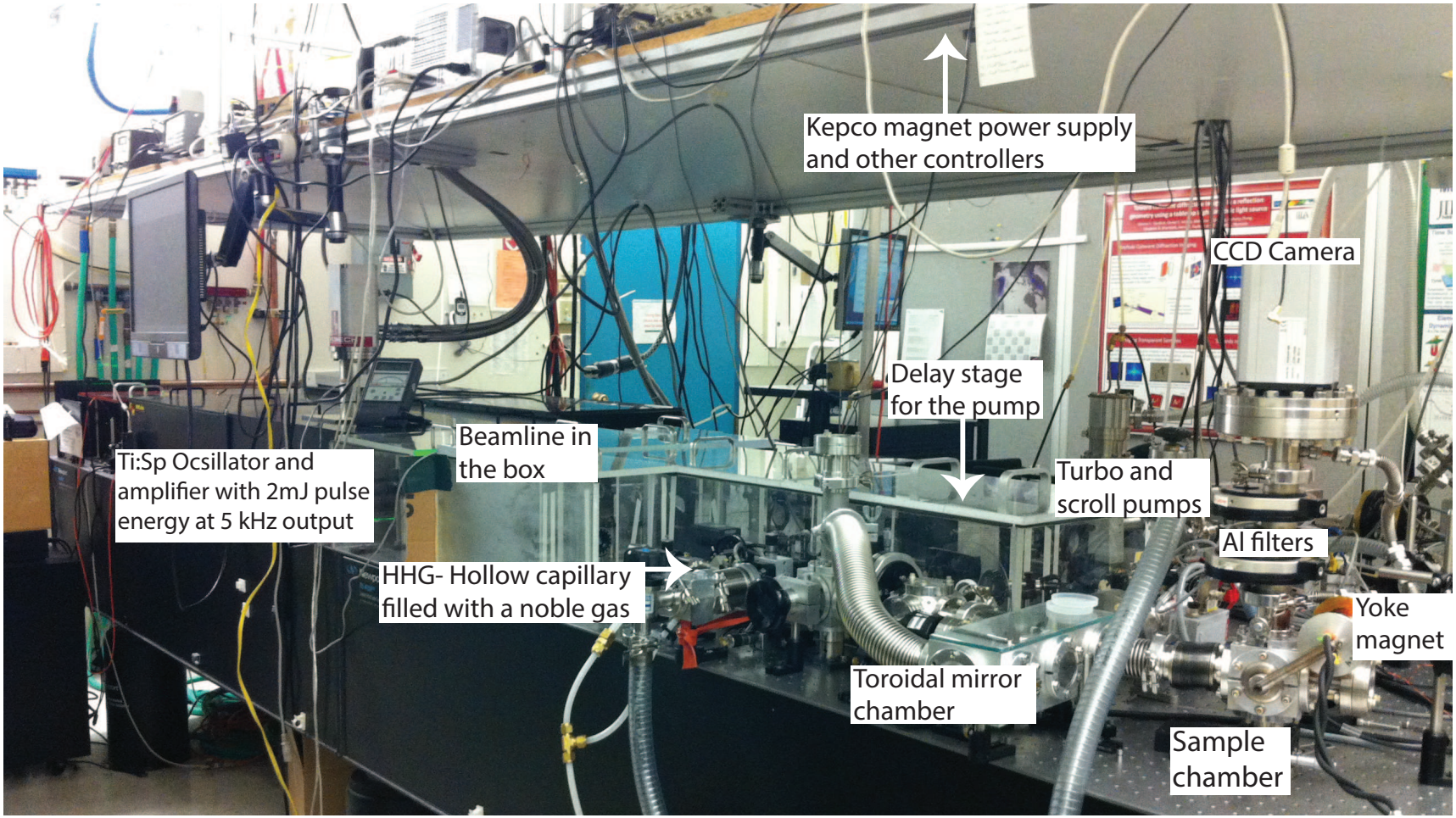


Figure 3.8: Picture of experimental setup. Some essential components are shown, such as the laser system, HHG hollow capillary, toroidal mirror and chamber, vacuum systems, sample chamber, aluminium filters, power supplies, iron yoke magnet, translational delay stage, and CCD camera.

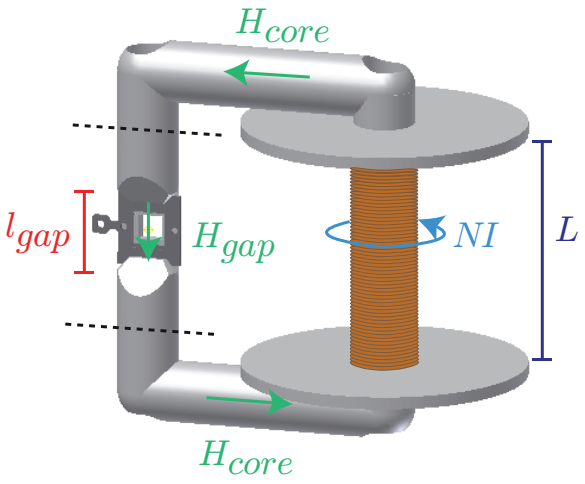


Figure 3.9: Illustration of iron magnet yoke with sample holder. $N$ is the number of wire turns, $I$ is the current on the wire, $l_{gap}$ is the width of the gap, $L$ is the total length of the iron yoke, $A_{gap}$ and $A_{core}$ are the total area of the gap and the core respectively, and $\mu_{core}$ is the permeability of the iron core.

a spectrometer. Because the determination of energies at the absorption edges of materials is important for magnetization dynamics, the calculation of the diffraction orders on the CCD camera is a crucial part of our experiment.

There are two regions on the sample, one with a grating and one without a grating. This difference results in two different reflection coefficients from surface $r_1$ and $r_2$, as shown in Figure 3.10. Since I assume that every point on the surface of the sample behaves as a source, the electric field on the CCD is the integration of all these electric fields as in

$$E_{screen}(x) = \sum E_i e^{-i\phi_i}, \tag{3.14}$$

where $\phi_i$ is the phase of the field $E_i$, $E_{screen}(x)$ is the electric field on the CCD at $x$ position.

After integration using experimental parameters, the electric field on the CCD becomes

$$\begin{aligned} E_{screen}(r_1, r_2, \lambda, \beta, N, h) &= \frac{r_1 + r_2 e^{-i2\pi\sqrt{2}h/\lambda} e^{-\frac{-i2d\pi}{\lambda}(\sin\beta - \sin\pi/4)}}{1 - e^{-\frac{-i4d\pi}{\lambda}(\sin\beta - \sin\pi/4)}} \\ &\times \left(1 - e^{\frac{-i4d\pi}{\lambda}(\sin\beta - \sin\pi/4)}\right) \times sinc\left(\frac{d\pi}{\lambda}(\sin\beta - \sin\pi/4)\right), \end{aligned} \tag{3.15}$$

where $N$ is the number of illuminated gratings, $\lambda$ is the wavelength of the EUV photon, $h$ is the

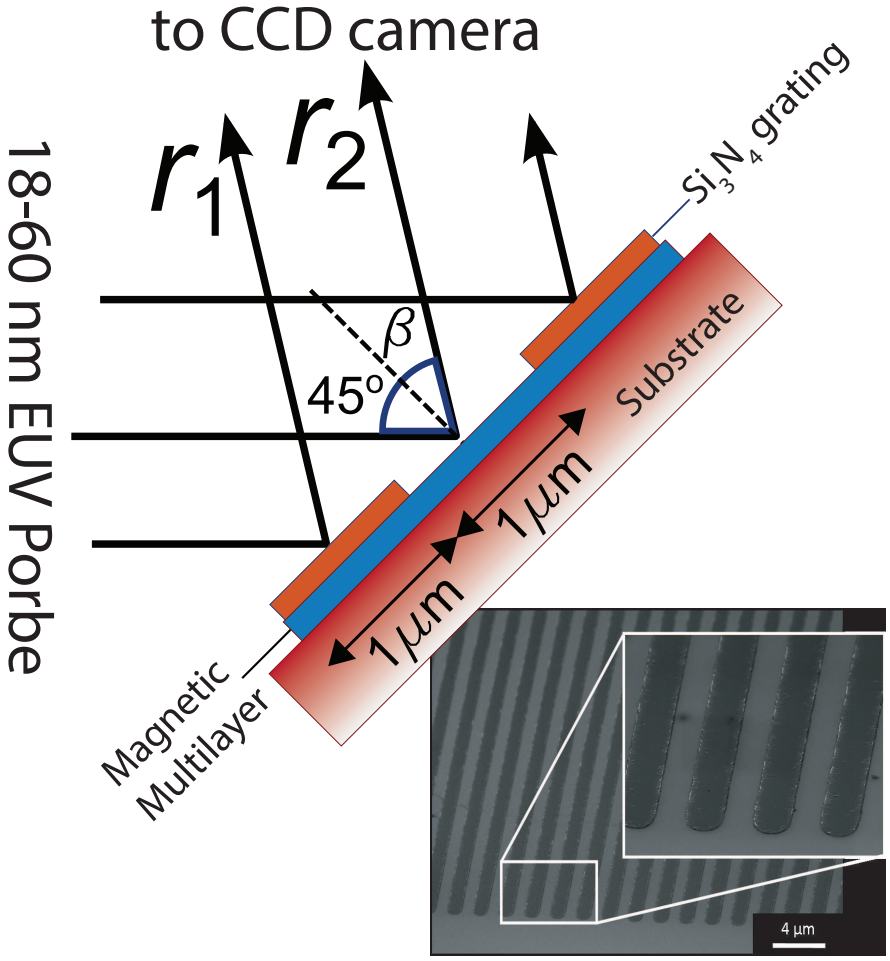


Figure 3.10: Illustration and AFM image of a grating sample. There are two types of samples we use. One type is a magnetic sample patterned as a grating on a substrate. In the second type, magnetic multilayers are patterned as thin films, and a 10-nm-thick $Si_3N_4$ grating is placed on magnetic films. Two designs give diffraction orders and work as a spectrometer. The grating spacing is 1 $\mu m$ and is limited by an optical lithography technique. To calculate the diffraction formula, I define two reflection coefficients, $r_1$ and $r_2$. The reflection angle $\beta$ defines the constructive and destructive interferences on the camera depending on the wavelength of the incident EUV photon.

height, and $d$ is the width of the grating, and $sinc(x) = \sin x/x$. The reflection angle $\beta$ can be expressed in terms of the distances as,

$$\tan\beta = \frac{Pp}{z},$$

where $p$ is the pixel size, $P$ is the number of pixel, and $z$ is the distance from the sample to the detector.

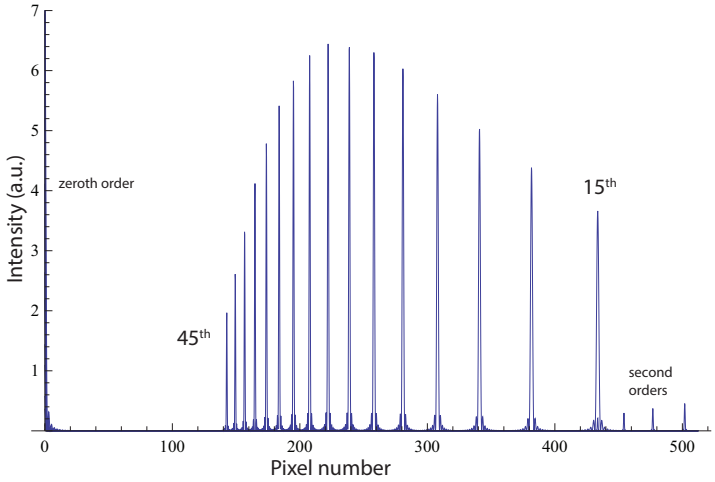


Figure 3.11: Calculation of Equation 3.15 for $45^{th} - 15^{th}$ harmonics. I use $P = 0 - 512$, $p = 26\ \mu m$, $d = 1\ \mu m$, $r_1 = r_2 = 0.01$, and $h = 10\ nm$ for the calculations. This is the typical experimental spectrum extracted by the CCD camera except the peaks are not sharp because of the defects at the grating edges.

I calculate and plot the absolute value of the electric field on the CCD from the $45^{th}$ to the $15^{th}$ harmonics using Equation 3.15, as shown in Figure 3.11. I use following parameters: $P = 0 : 512$, $p = 26\ \mu m$, $d = 1\ \mu m$, $r_1 = r_2 = 0.01$, $h = 10\ nm$. Importantly, to find the energy calibration of our spectrometer, I do not need all of Equation 3.15. The constructive interference positions are given by the denominator of Equation 3.15 as

$$0 = 1 - e^{-\frac{-i4d\pi}{\lambda}(\sin\beta - \sin\pi/4)}, \tag{3.16}$$

and the solution for $\beta$ is

$$\beta = \arcsin\left(\frac{\lambda}{2d} + \sin\pi/4\right). \tag{3.17}$$

Finally, I use Equation 3.17 for $\beta$ and find the pixel number in terms of the wavelength of the EUV photon

$$P = \frac{z}{p}\tan\left(\arcsin\left(\frac{\lambda}{2d}+\sin\pi/4\right)\right), \tag{3.18}$$

where $d$ is the width of the grating, not the period. Equation 3.18 will be used in the next chapters to calibrate HHG energies.

## 3.6 Conclusion

To conclude this chapter, I introduce the EUV T-MOKE experimental setup. First, the source part–HHG phenomena is mentioned by explaining physical background and three-step model. Second, I account for the excitation of the magnetic multilayers by calculating the absorption profiles by using Poynting's vector. Then, I briefly introduce the important experimental components. Finally, I explain how the grating sample is used as a spectrometer and find the EUV-photon-energy calibration on a CCD camera.

# Chapter 4

# Driving Mechanisms at Ultrafast Demagnetization

## 4.1 Introduction

In this chapter, I review the physical mechanisms responsible for ultrafast demagnetization dynamics following an ultrafast excitation. Although these ultrafast demagnetization dynamics have been studied with many proposed models for describing ultrafast reduction of a magnetic moment for 25 years, there is as yet no complete explanation because of complication of the problem. A magnetic material in a highly nonequilibrium state has profoundly interactive electrons, phonons and spins. These interactions are an unsolvable many-body problem for the itinerant ferromagnets (Ni, Fe, Co) because of their sophisticated electron and spin configurations. Many experimental and theoretical studies have attempted to resolve this problem to answer such important physical questions as: How does the exchange energy behave in magnetic alloys, ultrathin films, multilayers, and the nanoscale world? How fast can a magnet lose its magnetization? What kind of interactions exist among microscopic particle spins, electrons, photons, magnons and phonons? One classical way to look for the nature of a force is to investigate time scales of incidents and physical pictures. Thus, time dependent studies have been performed for three decades to understand the physics of these interactions and answer the three questions posed here.

Three early studies on ultrafast dynamics of magnetization are shown in Figure 4.1 taken from [85, 9, 70]. In 1990, Vaterlaus et al. explored spin-lattice relaxation in an Fe film. They used two ultrafast pulses with pulse lengths of 20 ns and 30 ps. The pulses excite the electrons, causing then to leave the Fe film. The photoexcited electrons are then detected by a spin-polarized analyzer.

In the case of the 30 ps pulse, the spin-polarization of electrons does not change: the polarization stays same for all photon energies, shown by the filled circles in Figure 4.1a. In contrast, the spin-polarization of the emitted electrons decreases almost to the zero with the 20 ns pulse, shown in Figure 4.1 (a) open circles [85]. This result means that the spins of the electrons remain in the initial states, no demagnetization occurs within 30 ps. However within 20 ns, a reduction in the magnetic moment is observed because of spin-lattice relaxation. In other words, spin-orbit interactions cause electrons to lose their spin-angular momentum in the lattice, and as a result, the spin polarization of the electrons disappears. These time scales were expected because of the known strength of the spin-orbit interaction in Fe. This result answered some questions for a while, but other questions soon appeared. For instance, can the electron-phonon relaxation (which is much faster than spin-lattice relaxation) affect the magnetic moment of electrons? In 1996, Beaurepaire et. al. used the magneto-optical Kerr effect (MOKE) to probe the magnetization of a Ni film after ultrashort laser excitation as shown in Figure 4.1 (b). Surprisingly, the magnetic moment of the Ni film decreased in 1 ps, a time that is much faster than spin-lattice relaxation [9]. What occurred was that the highly excited electrons scattered off other electrons and quasi particles or migrated to other sites in the material. The result was a rapid demagnetization. This unexpected result attracted much attention because until then scientist believed that the fundamental switching process for magnetic systems could not be faster than 100 ps. This supposed 'speed limit' is considered to be an obstacle for magneto-optical storage devices and spintronics applications.

After the surprise of ultrafast demagnetization, the validation of MOKE was recognized for probing magnetic behavior or an electron response. One year later, Scholl et al. probed the spin-polarization of photoelectrons after an ultrashort laser excitation and clarified two prior experiments [70]. They used ultrathin 12 and 6 ÅNi films to probe the magnetization at long (hundreds of ps) and short (one ps) time scales, as shown in Figure 4.1 (c) and (d). For the 12 ÅNi film, the magnetization dropped 20% within 1 ps, as in [9], and kept demagnetizing until zero-spin polarization occurred at approximately 1 ns. Actually there are many interesting physical phenomena hided in these results. Within first ps, the ultrashort pulse excites the electrons as in the Stoner excitation picture which is

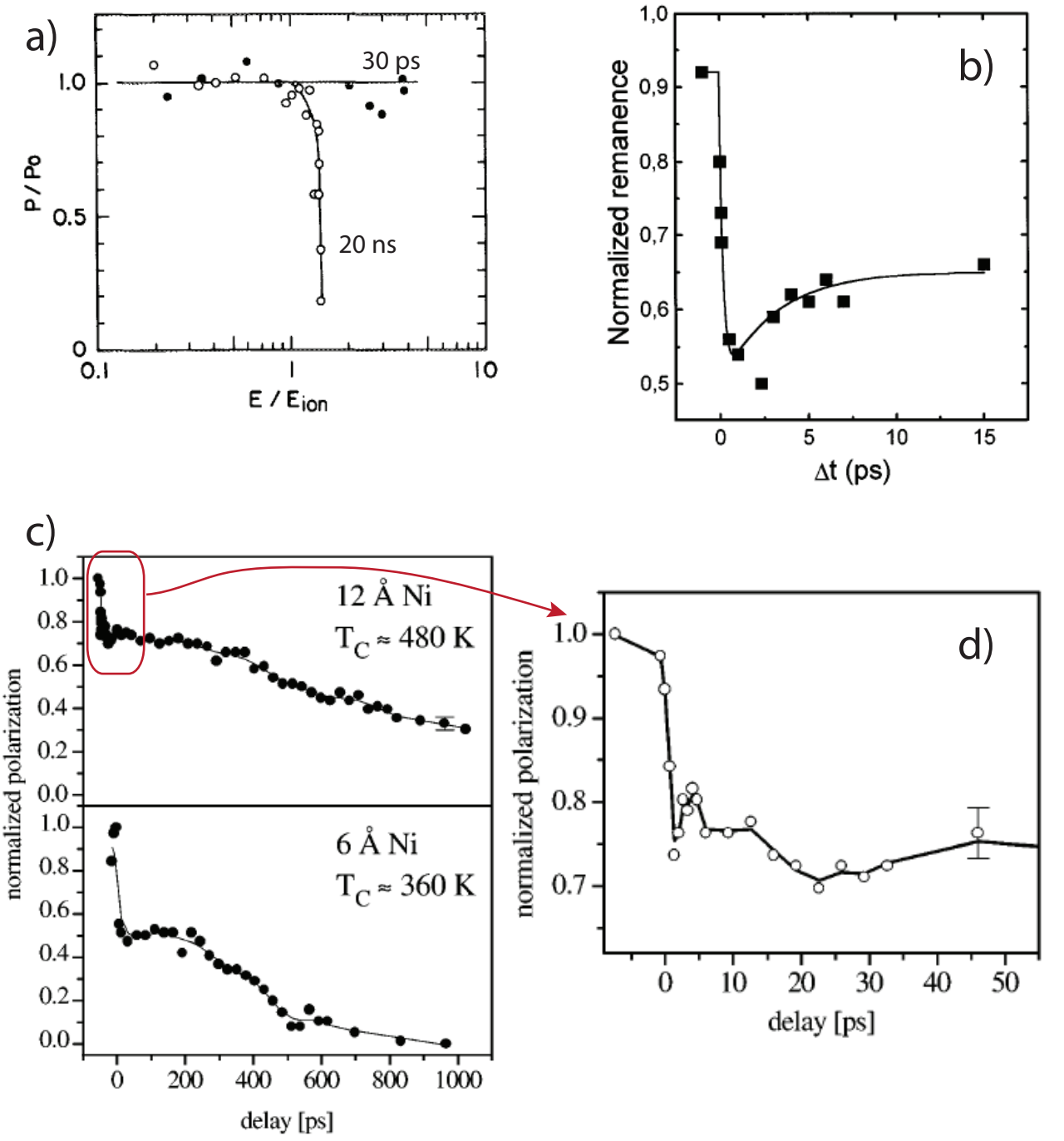


Figure 4.1: The first three experimental reports on ultrafast magnetization dynamics. (a) Spin-polarized photoelectrons from Fe were detected after two ultrashort optical pulses of 20 ns and 30 ps. While the 20 ns pulse caused a decrease in magnetic moment, the 30 ps pulse was too fast to capture any demagnetization. This results suggests that the spin-lattice relaxation is much longer than 30 ps [85]. (b) The second, maybe more famous, example is from 1996 [9]. By using magneto-optical Kerr effect, the researches were able to demagnetize the Ni film in 1 ps. Here electron-electron and electron-phonon scattering initiated demagnetization much sooner than would spin-lattice relaxation. (c) By looking at long- and short-timescale magnetization dynamics in Ni by employing photoelectrons, this study was able to explain the observations in (a) and (b). In the first ps, demagnetization starts with Stoner-like excitations and continues by creating of transversal spin waves, shown by (d) in detail.

direct excitation of electrons from their initial states into unoccupied states above the Fermi level. As a result, these excitation creates Stoner pairs. Then, these Stoner pairs create longitudinal spin fluctuations and cause demagnetization. Because high number of Stoner excitation requires so much more energy which is not the case in the experiment, the demagnetization amount is small at the beginning. After electron-phonon relaxation equilibrates the temperature of the electrons and phonons within 5 ps, the electron temperature decreases, and the magnetization recovers about 5% of its initial value. Then, the excitation of spin waves starts via transversal spin fluctuations through 1 ns. However, these scattering dynamics are still unclear in itinerant ferromagnets. Furthermore, because the intra-atomic exchange interaction exists in Fe, Co and Ni, the local magnetic moment in these ferromagnets can not be decoupled from the electron subsystem [70]. As I said ultrafast demagnetization is an important question for technological applications. Moreover, there are more questions to answer to given a fundamental understanding of the ultrafast nature of electron-photon-spin-phonon couplings in ferromagnets.

Thus far I discuss very early examples of ultrafast magnetization dynamics. I now elaborate on the proposed models explaining ultrafast magnetization dynamics. First, I introduce the phenomenological three-temperature model as a macroscopic model. Second, I discuss the macroscopic Landau-Liftshitz-Bloch equation modified with atomic-spin calculations. Finally, I explain microscopic models such as: the microscopic three-temperature model, coherent spin-photon coupling including Zhang-Hubner's and Bigot's models, and lastly the superdiffusive spin current model which has made an important contribution to the ultrafast magnetization dynamics in multilayers.

## 4.2 Three Temperature Model

Ultrafast electron dynamic studies started in noble metals before magnetic materials [28]. These dynamics usually were modeled by the two-temperature model. In the two-temperature model, one assumes that electrons and the lattice are heat reservoirs by defining the temperature of the electrons and phonons. In a magnetic system, however, the spin-degree of freedom was added as a third reservoir. As illustrated in Figure 4.2, there are three reservoirs ($electron-spin-phonon$)

with their heat capacities ($C_e - C_s - C_p$), three temperatures ($T_e - T_s - T_p$) and coupling constants ($G_{el} - G_{es} - G_{sl}$) [9]. The coupling between the three reservoirs is represented by the following differential equation

$$\begin{aligned} C_e(T_e)\frac{\partial T_e}{\partial t} &= G_{el}(T_l - T_e) + G_{es}(T_s - T_e) + P(\mathbf{r}, t), \\ C_l(T_l)\frac{\partial T_l}{\partial t} &= G_{el}(T_e - T_l) + G_{sl}(T_s - T_l) - \kappa\nabla^2 T_l(\mathbf{r}, t), \\ C_s(T_s)\frac{\partial T_s}{\partial t} &= G_{es}(T_e - T_s) + G_{sl}(T_l - T_s), \end{aligned} \tag{4.1}$$

where $P(\mathbf{r}, t)$ describes the laser heating term, and $\kappa\nabla^2 T_l(\mathbf{r}, t)$ is the heat diffusion via the lattice [22]. By assuming that the spin-heat capacity is negligible and the heat capacities of the electrons and the lattice are constant at low fluences, Equation 4.1 can be solved analytically for the spin temperature $T_s$ and the magnetization M as a function of time $t$ as

$$\frac{\Delta M}{M} = -\frac{A_2\tau_E - A_1\tau_M}{\tau_E - \tau_M}e^{-t/\tau_M} - \tau_E\frac{A_1 - A_2}{\tau_E - \tau_M}e^{-t/\tau_E} - A_3 e^{t/\tau_R}, \tag{4.2}$$

where $\tau_M$, $\tau_E$ and $\tau_M$ are the observed demagnetization, recovery, and slow recovery times, respectively. $A_1$, $A_2$ and $A_3$ are decay constants. Equation 4.2 has been used to fit experimental demagnetization curves and extract demagnetization time constants. However, one can simplify this equation to

$$M(t) = 1 - A(1 - e^{-t/\tau_M})e^{-t/\tau_R}, \tag{4.3}$$

for normalized magnetization as a function of time. I use Equation 4.3 for fitting in the following chapters of the thesis.

## 4.3 Landau-Lifshitz-Bloch Equation–Atomistic to Thermal Macro Spin Model

The Landau-Lifshitz equation is used to describe the precession dynamics of magnetic moments. In the case of damping of a magnetic moment without magnitude change, such as micromagnetic simulations, the Landau-Lifshitz-Gilbert (LLG) equation is used. However, the LLG

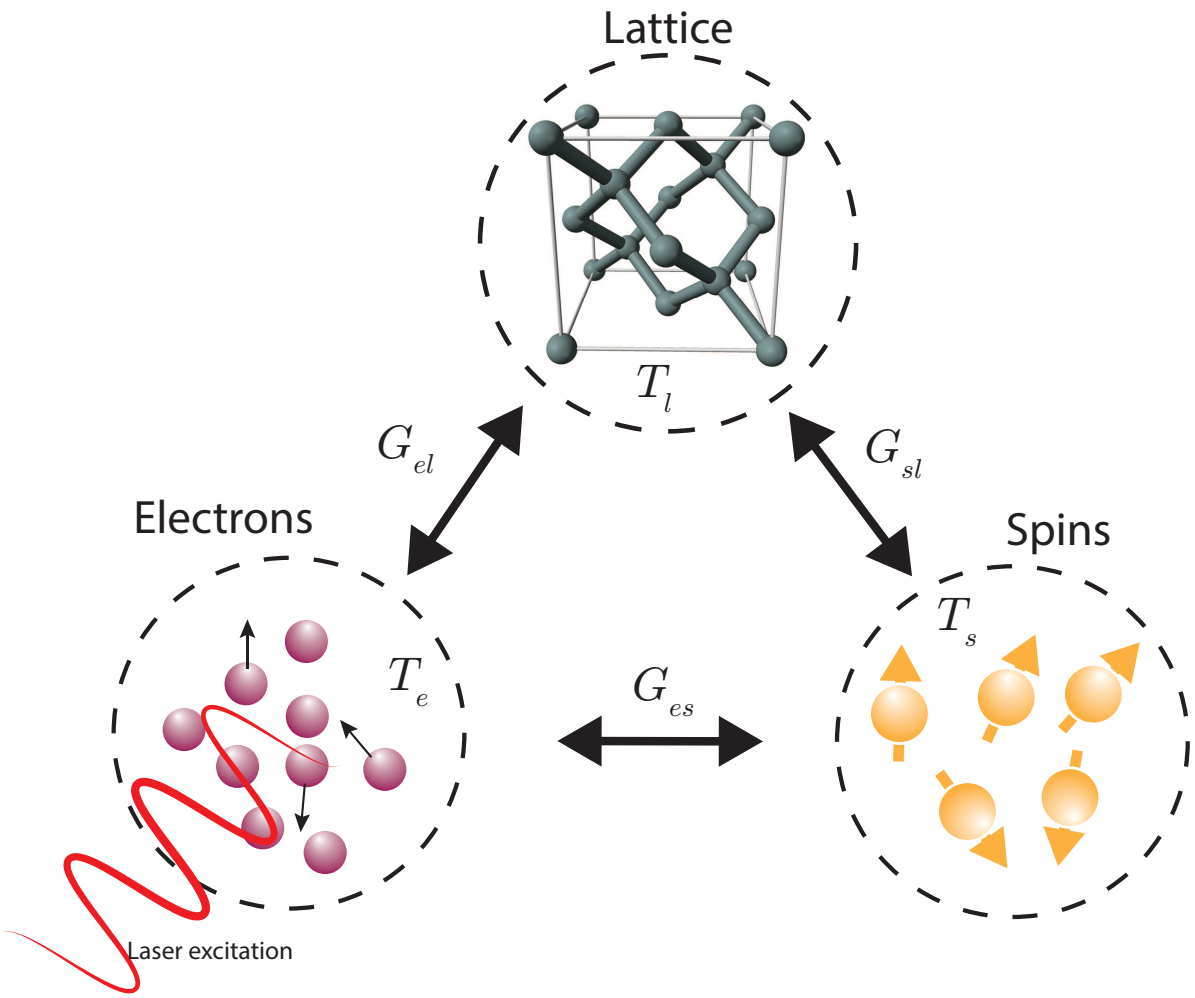


Figure 4.2: Phenomenological three-temperature model. The electron, spin and lattice are modeled as three heat reservoirs. Three of them have temperatures, heat capacities, and interactions between one another represented by coupling constants. An ultrashort optical pulse excites and heats the electron system rapidly. Then the three reservoirs interact and equilibrate their temperatures. From observations of the transient reflectivity and magnetization dynamics, the electron and the spin temperature can be extracted experimentally: then the rest of the unknowns can be calculated.

equation is valid at low temperature and does not allow a magnitude change in the magnetic moment. However, under highly nonequilibrium circumstances, one must add a longitudinal damping factor to the LLG [30], which results in following Landau-Lifshitz-Bloch (LLB) equation

$$\frac{\partial \mathbf{M}}{\partial t} = -\gamma \mathbf{M} \times \mathbf{H}_{eff} + \gamma \alpha_{\|} \frac{(\mathbf{M} \cdot \mathbf{H}_{eff})\mathbf{M}}{M^2} - \frac{\gamma \alpha_{\perp}}{M^2} \mathbf{M} \times (\mathbf{M} \times \mathbf{H}_{eff}), \tag{4.4}$$

where $\gamma$ is the gryomagnetic constant, $\mathbf{H}_eff$ is the external magnetic field, $\alpha\|$ and $\alpha_\perp$ are longitudinal and transversal damping parameters [36]. The first term on the left describes the precession around $H_{eff}$, the second term describes the transversal-damping alignment along $H_{eff}$, and the third term causes demagnetization by longitudinal damping, as illustrated in Figure 4.3.

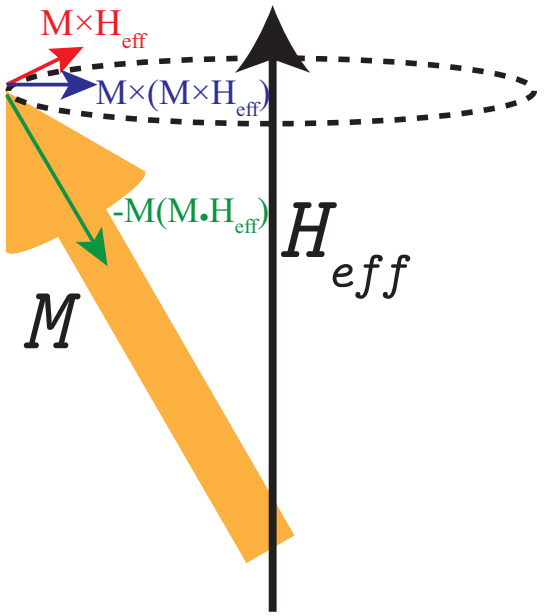


Figure 4.3: Illustration of the Landau-Lifshitz-Bloch equation with three terms. The red force along the dashed line keeps the magnetic moment precessing around $H_{eff}$. The blue force applies a transversal damping to align the magnetic moment along $H_{eff}$ without changing the magnitude of the moment. The green force is the source of demagnetization by longitudinal damping.

Clearly, the LLB equation successfully describes some demagnetization dynamics [1, 14]. The physical challenge comes from calculations of the longitudinal and transversal damping parameters $\alpha\|$ and $\alpha_\perp$ from first principle. Fortunately, these parameters can also be derived in terms of

measurable parameters of a system by [2] as below,

$$\alpha_{\parallel} = \frac{\lambda}{m_e}\frac{2T}{3T_c}\frac{2q}{\sinh 2q}; \alpha_{\perp} = \frac{\lambda}{m_e}\left(\frac{\tanh q}{q} - \frac{T}{3T_c}\right), \tag{4.5}$$

where $q = 3T_c m_e/2(S+1)T$, $T_c$ is the Curie temperature, $m_e$ is the mass of electron, and $\lambda$ is the coupling constant of the atomic spins to the heat bath. The LLB equation derived from first principles gives similar results to the microscopic three-temperature model that I will discuss in the section 4.4.1.

## 4.4 Microscopic Models

In this section, I elaborate on our microscopic understanding of and quantum nature of ultrafast demagnetization.

### 4.4.1 Microscopic Three Temperature Model

The LLB model combines microscopic atomic spins with a macroscopic thermal model. The microscopic three-temperature model (M3TM) also uses a similar approach. Koopmans et al. drives an effective Hamiltonian by introducing spin-flip scattering mediated by phonon-electron or impurities-electron Elliot-Yafet scatterings [40, 37]. A Elliot-Yafet spin-flip type of scattering mechanism occurs between an electron and a phonon by allowing an angular momentum transfer with $\alpha_{EY}$ probability. Elliot-Yafet scattering is illustrated in Figure 4.4. The electron flips its spin from up to down or down to up with $\alpha_{EY}$ probability, while it conserves its angular momentum with $1 - \alpha_{EY}$ probability.

The most debated parameter in M3TM is the probability of $\alpha_{EY}$ that determines the demagnetization time constant directly. For example, when $\alpha_{EY} \sim 0.5$, the theoretically predicted demagnetization time constants are getting close to the experimental values. However, this probability is much higher than some theoretical models and still under debate [16]. Nonetheless, the demagnetization constant calculated by M3TM model equals

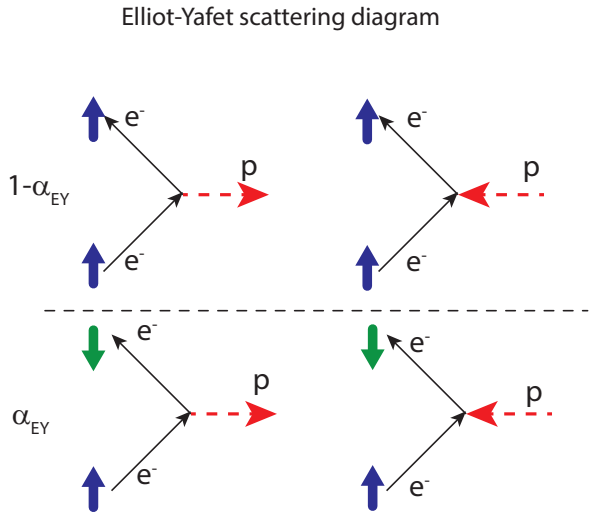


Figure 4.4: llustration of the Elliot-Yafet scattering mechanism. An electron flips its spin by creating or absorbing a phonon with $\alpha_{EY}$ probability.

$$\tau_M = F\left(\frac{T}{T_c}\right)\frac{\hbar}{4k_B T_c}\frac{1}{\alpha}, \tag{4.6}$$

where $F(T/T_c)$ is a temperature-dependent function and close to unity at low fluences, $k_B$ is the Boltzman constant, and $\alpha$ is the Gilbert's damping constant. The M3TM predicts time constants of demagnetization for pure elements and permalloy successfully. However, the rare-earth magnetic metals and alloys can not be described with M3TM because of localized band structure of $4f$ electrons in them [89]. Recently, Koopmans et al. came with two different types of M3TM for 3d itinerant and rare-earth ferromagnets. They explain the long demagnetization time constants for the rare-earth ferromagnets and ferrimagnets by introducing a fourth heat reservoir [39]. More details can be found the reference [22].

### 4.4.2 Coherent Spin-Photon Coupling

The first attempt to describe coherent coupling between spin and a photon was performed by Zhang-Hubner [93, 95]. This theory used a monolayer Ni system and a Hubbard-like Hamiltonian that includes spin-orbit coupling and band structure. In addition, Zhang and Hubner included the strong electron correlation without any perturbative treatment. Next, they calculated the susceptibilities to find the linear-optical and magneto-optical responses. They found that spin-orbit coupling and the external field cooperatively induces dephasing within $\sim$ 10fs. However, the calculated demagnetization was two orders of magnitude smaller than experimental observations. Hence, coherent interactions cannot completely explain ultrafast demagnetization dynamics.

Later, Bigot et al. proposed a model combining coherent interactions with thermalization and phonon coupling [11, 88]. First, they experimentally studied magnetization dynamics by varying the pump-pulse fluence and polarization. They concluded that the origin of relativistic-quantum electrodynamics plays major roles rather than spin-orbit interaction. After the coherent interactions between charges, spins, and photons, the electrons and the spins thermalize. This thermalization keeps the demagnetization at high rates. Finally, the lattice couples with electrons and spins by radiating THz photons. I explain these processes in Figure 4.5. In addition to their experimental

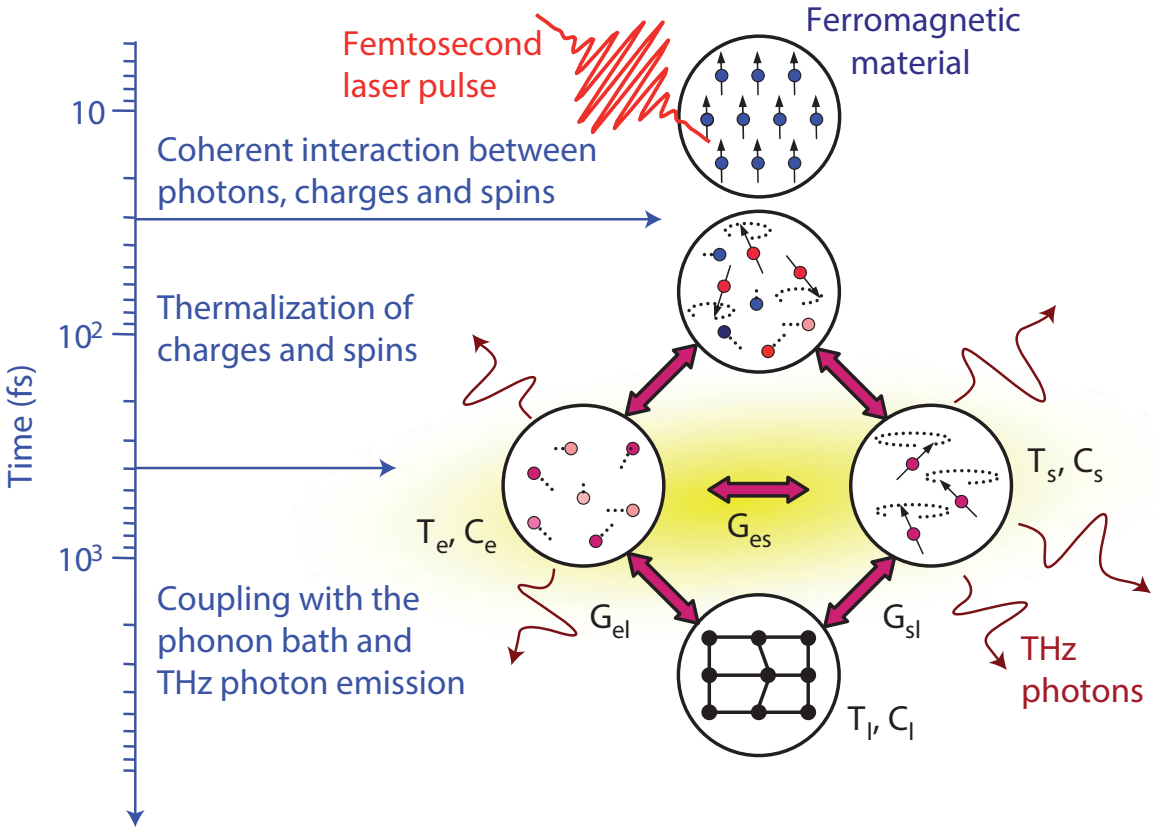


Figure 4.5: Coherent spin-photon interaction [11]. First, the photons interact with electrons and spins because of relativistic quantum electrodynamics. These interactions initiate the demagnetization process. Then, thermalization between spins and electron occurs within 100 fs. Finally, the spins and electrons couple with the lattice and lose the magnetization further by radiating THz photons. The figure is taken from [11].

study, they later performed theoretical calculations. However, they did not satisfy the observed dynamics. Indeed, because of the complexity of the problem, the simplified hydrogen-like atomic levels were used to model coherent photon-electron-spin coupling in the full relativistic-quantum electrodynamics simulations, and only 0.2% demagnetization was achieved [88].

### 4.4.3 Superdiffusive Spin Currents

Thus far, I explain localized spin-scattering and coherent interaction mechanisms in demagnetization processes. However, this localized picture of the electrons in the itinerant ferromagnets are not always true and the electrons quite mobile. This fact reminds that nonlocal mechanisms due to the displacement of the electrons should also be taken into account in analyzing demagnetization processes. Actually, spin transport phenomena is not new. At long time scales, spin transport torque and other transport geometries have been used widely, but an ultrafast approach to spin transport was new. One important question triggered by the idea of spin transport at ultrafast time scales is: where does the spin angular momentum go? The total angular momentum of the system must be conserved as

$$\mathbf{L}_{total} = \mathbf{L} + \mathbf{S} + \mathbf{L}_{phonon} + \mathbf{L}_{photon}, \tag{4.7}$$

where $L$ and $S$ are the orbital and spin angular momenta of the electron, and last two terms are the angular momenta of the lattice and photon. Angular momentum of the photon system can cause only negligible change in the magnetization. Some calculations indicate that neither Elliot-Yafet scattering rate is enough to demagnetize a sample by more than a couple of percent [17]. The only remaining possibility is that electrons lose angular momentum by moving laterally from the probing sites. The first experimental attempt to investigate ultrafast spin currents was done by Malinowski et al. [48]. Two important graphs in Figure 4.6 (form [48]) show a direct angular momentum transfer between magnetic multilayers. In the experiment, the Co/Pt multilayers were used with two different spacer layers, an insulating NiO layer and a conducting Ru layer. Depending on the magnetic field, the magnetic layers could be aligned parallel or antiparallel, as shown Figure 4.6

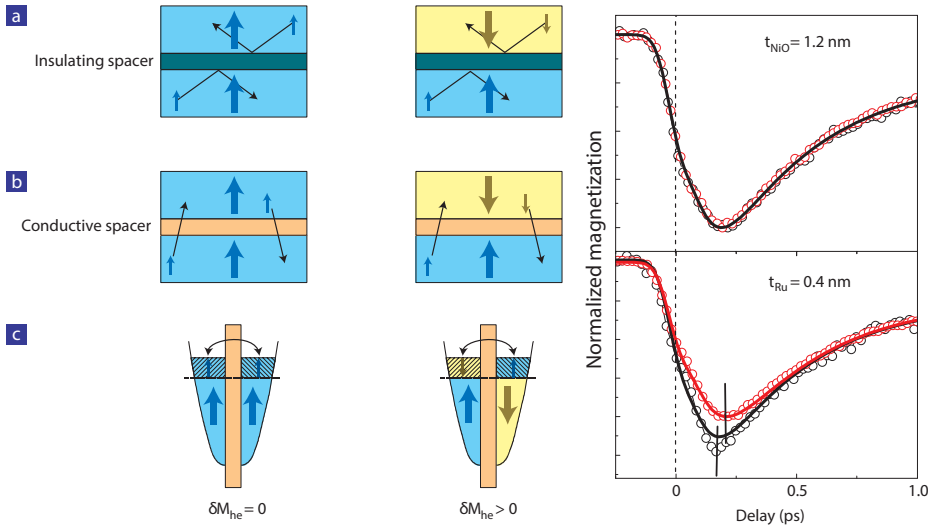


Figure 4.6: First observation of direct spin transport taken from [48]. Co/Pt magnetic multilayers are sandwiched with insulating NiO and conducting Ru layers. Ultrafast magnetization dynamics are probed with MOKE for parallel and antiparallel alignments. While the dynamics are the same for the insulating NiO layer; surprisingly, the Ru layer allows direct spin transport from one layer to another, resulting in more demagnetization for the antiparallel layers (black curves) then the parallel arrangement (red curves).

(a) and (b). The black curves are for antiparallel alignments and the red curves are for parallel alignments. Interestingly, in the case of the conducting Ru layer, the amount of demagnetization is greater when the layers are oppositely aligned. This result suggests that there exists a direct spin transfer at ultrafast time scales. The illustration at left of the Figure 4.6 explains furthermore how opposite alignment can cause an imbalance in spin-up and spin-down electrons.

An explanation of superdiffusive spin transport requires some background information about the itinerant properties of electrons. In noble metals, a conduction electron moves at a velocity $\sim$ 1 fs/nm and relaxes within 1-100 fs which is the relaxation time $\tau_R$. Nonetheless, this electron never loses its charge during collisions, because charge is conserved. However, the electron does not have to conserve its spin; the spin can flip but not necessarily during every collision. Furthermore, the spin-relaxation time is material dependent, and the spin-diffusion length can vary from 1 to 100 nm in metals. In ferromagnets different than normal metals, the lifetime of an electron depend on also the spin orientation. In other words, the majority (spin-up) and the minority (spin-down) do have

different lifetimes and velocities in the conduction band. Figure 4.7 shows electronic properties of Ni as an example. Because of exchange splitting, there is an imbalance in the number of electrons in the spin-up (dashed blue) and spin-down (solid red) bands. This imbalance results in very different the characteristics of electrons below and above the Fermi level [96, 97]. When an electron from the spin-down band (solid red) is excited to a 3d-like band, the electron becomes more localized, so its velocity and lifetime would be short. On the other hand, since there is not much room in the spin-up band, the excited spin-up electron feels like a s- or p-like band and would be more mobile. Theoretical calculations of these velocities and lifetimes are shown in Figure 4.7 (b) and (c). Clearly asymmetries in spin lifetimes and velocities offer a large contrast in transportation and can lead to a spin-dependent transportation or *spin-currents*.

The idea of using spin-dependent transport during ultrafast demagnetization was proposed developed by Battiatio et al. [6]. They derived spin-dependent lifetimes and velocities of excited electrons above the Fermi level from first principle. Then, Battiatio et al. used a classical transportation model to develop new transport regime because the electrons at excited states can move neither diffusively nor ballisticly. The intermediate regime between diffusion and ballistic transportation takes place, which is called superdiffusive [6, 7]. Fundamentally, the magnetization is written as $M = 2\mu_B(n\uparrow - n\downarrow)$, with the Bohr magnet $\mu_B$ written in terms of numbers of electrons in the spin-up and the spin-down channels. In the superdiffusive transport, the first step is to find these numbers of electrons by a continuity equation

$$\frac{\partial n(\sigma, E, z, t)}{\partial t} + \frac{n(\sigma, E, z, t)}{\tau(\sigma, E, z, )} = \left(-\frac{\partial}{\partial z}\hat{\Phi} + \hat{I}\right) \times \left(\hat{S}_n(\sigma, E, z, t) + S^{ext}(\sigma, E, z, t)\right), \tag{4.8}$$

where

- $n$ is the spin- and energy-dependent density of excited electrons,
- $\tau$ is the lifetime,
- $\hat{I}$ is the identity operator,

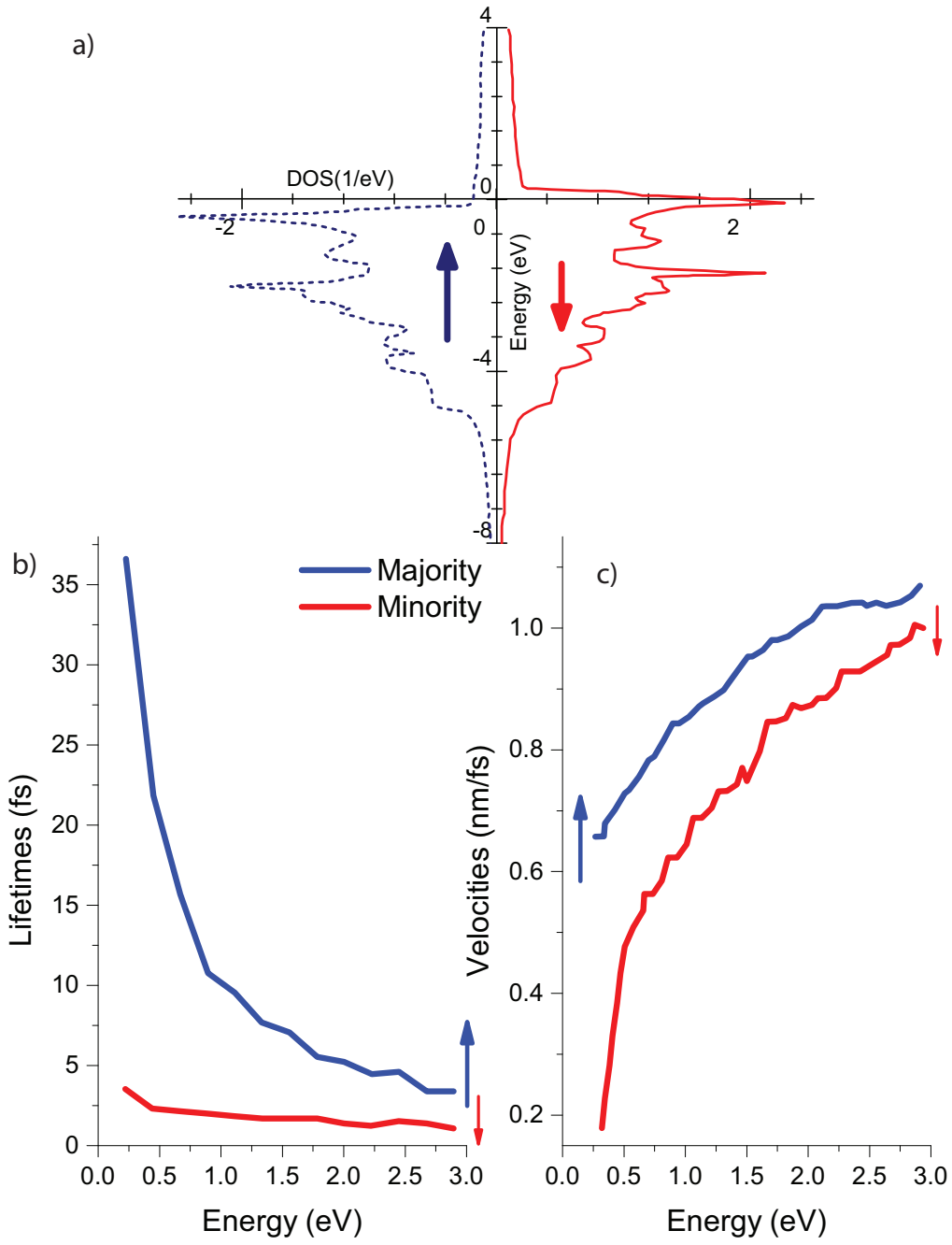


Figure 4.7: Density of states of Ni and lifetimes and velocities of electrons above the Fermi level taken from [97]. Above the Fermi level, the spin-down band has more *d*-like bands, resulting in smaller velocities and lifetimes for spin-down electrons. However, this is opposite for spin-up electrons because of s- or p-type bands above the Fermi level. These differences in lifetimes and velocities give rise to spin-dependent transport, or spin currents.

- $\hat{S}_n$ is an integral operator that computes the source term for next generated electrons by elastic, inelastic, and cascade processes,
- $S^{ext}$ is the source term containing pump excitation,
- $\hat{\Phi}$ is the electron flux term which is the devil in the details.

Solving this continuity equation for the spin-up and spin-down electrons, the total magnetization would be difference in the number of electrons in these two sates as $M = 2\mu_B(n \uparrow -n \downarrow)$. For further details on the theory of the superdiffusive transport please see [8].

One important puzzle about superdiffusive spin transport is whether this transportation is a pure spin current or a charge-plus-spin current. There is actually mass and charge transportation from site-to-site. However, the dielectric screening in metals is extremely fast, and so any imbalance in charge is compensated quickly, leaving a net spin current. We can understand this with small examples of Ni thin film on an Al substrate. As illustrated in Figure 4.7, the lifetimes of spin-up electrons are much longer which may result in eight spin-up and two spin-down electrons migration from Ni into Al substrate. Then to balance the charge, we must also have 5 spin-up and 5 spin-down electron migration from the Al substrate into Ni because of the absence of spin splitting. At the end, we observe 6 'pure spin' current while zero charge current is seen. I conclude the superdiffusive spin transportation model here by leaving experimental examples and some critics for Chapter 6.

## 4.5 Conclusion

In this chapter, I introduce physical mechanisms behind ultrafast magnetization dynamics. First, the phenomenological approach three-step model is explained. Then, I show how the Landau-Lifshitz-Bloch equation supported by atomic-spin calculations is used for ultrafast demagnetization. In the last section, I mention microscopic models. First microscopic model discussed is the microscopic three-temperature model which includes Elliot-Yafet spin-flip mechanism. Then I comment on coherent photon-electron-spin coupling. Finally I address the spin-dependent itinerant nature of spins and superdiffusive spin currents. All of the above theories help to explain ultrafast demag-

netization at similar or different timescales. However, there is no complete or combination of local and nonlocal representation of spin-charge dynamics in magnetic systems.

# Chapter 5

## Comparison of Electronic and Magnetic Contributions in Demagnetization

In the previous chapter Figure 4.1, I show that the observed demagnetization was approximately 20% in the spin-polarized photoelectrons experiments [70], while the MOKE experiments showed approximately 50% demagnetization [9]. The large amount of ultrafast demagnetization probed by MOKE experiment brought suspicion about the magneto-optical (MO) response at ultrafast time scales. So then, a couple of experiments were performed to identify non-magnetic contribution in the MO effects. These experiments revealed that the MO effect does not fully represent the genuine magnetic state of the matter. At the early stage of demagnetization until 400 fs, the MO response has a large contribution from purely charge dynamics.

In this chapter, I review previously performed investigations on the MO effect and their physical origins. Then, I readdress these artifacts for our EUV T-MOKE experiment because it is very important to claim any macroscopic and microscopic mechanisms. Finally, I convince you by theoretical and experimental works how the electronic contribution in the EUV T-MOKE signal is negligible. Thus I aim to prove that this technique provides a great advantage to study ultrafast magnetization dynamics on a tabletop source with any non-magnetic artifact.

### 5.1 Previous Investigations on Magneto-Optic

In Chapte 2, I show that one can detect only intensity variations of x-ray photons in EUV T-MOKE technique, whereas optical techniques provide a change in the polarization rotation and the ellipticity. If the optical-technique responses are purely magnetic, the magnetization $M$ must

be related to the polarization rotation $\theta$ and induced ellipticity $\epsilon$ as in

$$\frac{\Delta\theta(t)}{\theta_0} = \frac{\Delta\epsilon(t)}{\epsilon_0} = \frac{\Delta M(t)}{M_0}. \tag{5.1}$$

However, the Equation 5.1 is not true at all time scales because of severe modification of the electronic structure by an ultrafast excitation. This results in some contributions in the magnetic signal from purely electronic dynamics. I can model the entire MO response as a function of magnetization and the electronic artifact as

$$MO(t) = F(t)M(t), \tag{5.2}$$

where $F(t)$ represents the Fresnel contribution, i.e., the electronic artifact in the MO signal. Any change in MO response would be then

$$\Delta MO(t) = F(t)\Delta M(t) + M(t)\Delta F(t), \tag{5.3}$$

where $\Delta M(t)$ stands for pure magnetization change, while $\Delta F(t)$ is the artifact from Fresnel contribution which is usually unacceptable and unavoidable. Here, I show six different methods previously used to understand $\Delta F(t)$ term below also illustrated in Figure 5.1.

(1) The first example is about discrepancies in the induced ellipticity and the polarization rotation by Koopmans et al.[38]. They clearly showed that $\Delta\epsilon/\epsilon$ and $\Delta\theta/\theta$ deviate significantly in the first 400 fs. The non-equilibrium electron distribution distorts experimental measurements and gives non-genuine magnetic response, shown in Figure 5.1 (a).

(2) In the second examples, Regensburger et al. used the second-harmonic generation as MO probe. They observed that the magnetization dynamics have strange dependence on the pump-pulse fluences [63]. At high fluences, the MO signal reverses its sign, shown in Figure 5.1 (b). Furthermore, applying a second pump pulse distorts this reversed signal (c).

(3) In the third example, Kampfrath et al. investigated time resolved MOKE signal of Fe film

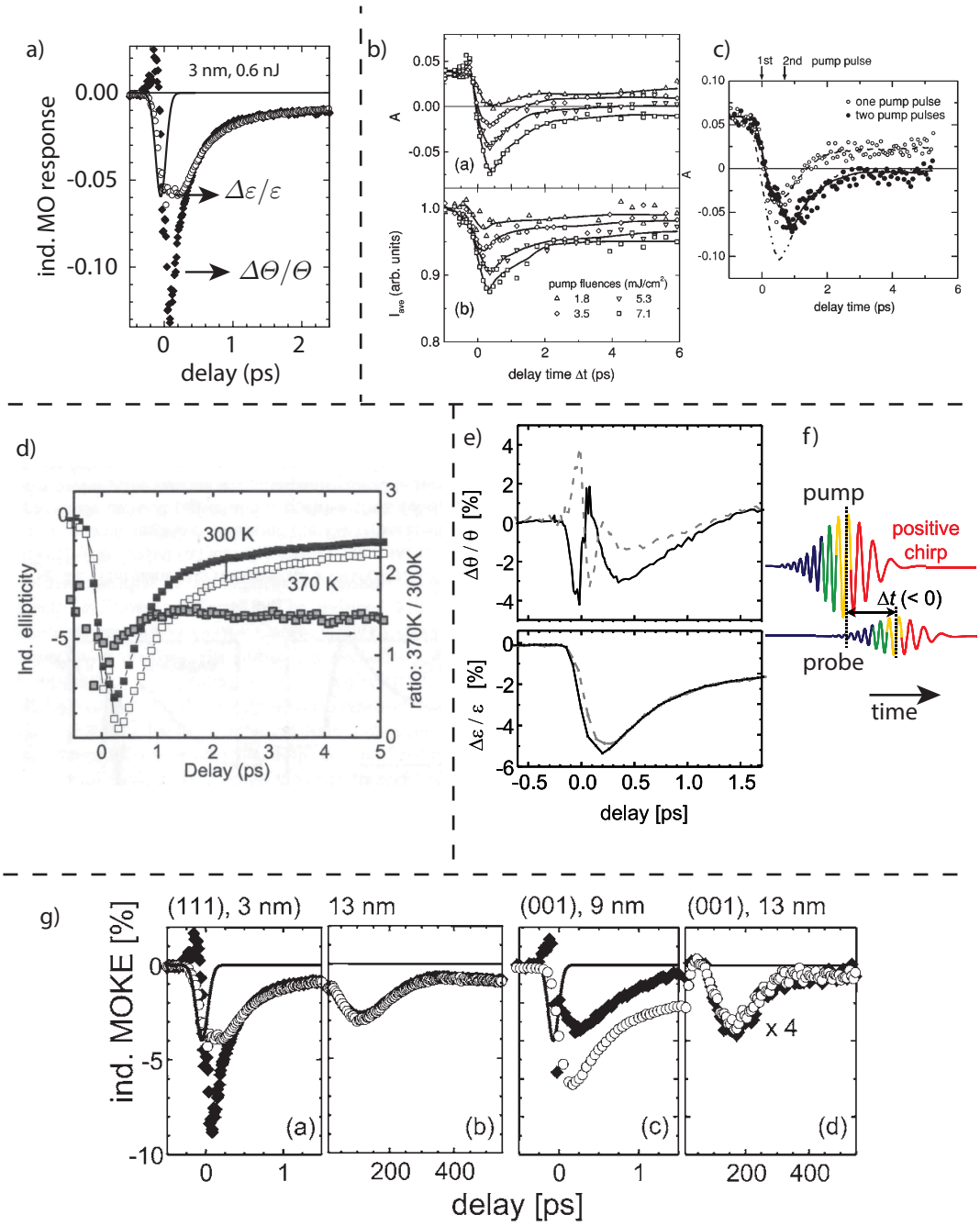


Figure 5.1: Previously done MO artifact investigations [38, 63, 34, 41]. a) The extracted two signal from the ellipticity and the polarization rotation show very different dynamics within the first 400 fs. b) and c) The second harmonic generation can also probe magnetization, but employing two pump pulses show very different dynamics even changing signs. d) Temperature dependent magnetization dynamics is probed by the optical setup and the initial dynamics do not show any correlation which again indicate optical artifacts at early time scales. e) and f) The optical artifact is investigated by modifying the chirp of the pulses, which results in different magnetization dynamics. g) Dependence of ultrafast demagnetization to the crystalline orientation is showed which is not originating from magnetization.

with two different probe wavelengths (400 nm and 800 nm) [34]. They saw a significant contrast in magnetization dynamics (not shown in Figure 5.1).

(4) The fourth example is about the ambient temperature. The ambient temperature is an important input parameter in magnetization dynamics. We can derive the Equation 5.3 for the temperature dependence as

$$\frac{\Delta\theta(t)}{\theta_0} \approx \frac{\Delta F'(t)}{F'_0} + \frac{dM/dT}{M_0}\Delta T_s(t). \tag{5.4}$$

We know the temperature dependence of the magnetization from static measurements and $F(t)$ is assumed independent from small changes in the temperature. If one performs two experiments at two different temperatures, the MO responses should be related with a simple ratio to each other. However, as shown in Figure 5.1 (d), two MO signals at 300 K and 370 K differ substantially within the first ps. After one ps, two signal behave as they are supposed to be. This result prove that the MO signal within 1 ps is highly questionable in optical pump-probe experiments [38].

(5) The fifth example is about the dichroic bleaching artifact in MO signal. The dichroic bleaching was shown by using two different chirps of the laser pulse in MO experiment. I first explain the dichroic bleaching, also known as state filling or becoming transparent of material after ultrafast excitation. I illustrate the dichroic bleaching effect in a magnetic material in Figure 5.2. For example, the pump pulse can excite only a spin-down electron because it does not have resonance with spin-up channel, shown in Figure 5.2 (a). Then, there are holes in only the minority channel before any spin-flipping happens (b). However, if one measures the MO response of the modified band structure as a function of the frequency, an important modification would be observed. The imaginary part of $\epsilon$ changes to a Lorentzian shape, which causes an artifact in MO response. Koopmans et al. performed an experiment by using oppositely chirped pulses and observed profound differences in MO response, Figure 5.1 (e). The polarization rotation gives totally opposite signal for the

positively and negatively chirped pump pulses. This artifact is illustrated in Figure 5.1 (f) for the positively chirped pump. Therefore, this suggests that using similar wavelengths for the pump-probe experiment results in an unavoidable dichroic bleaching artifact [41].

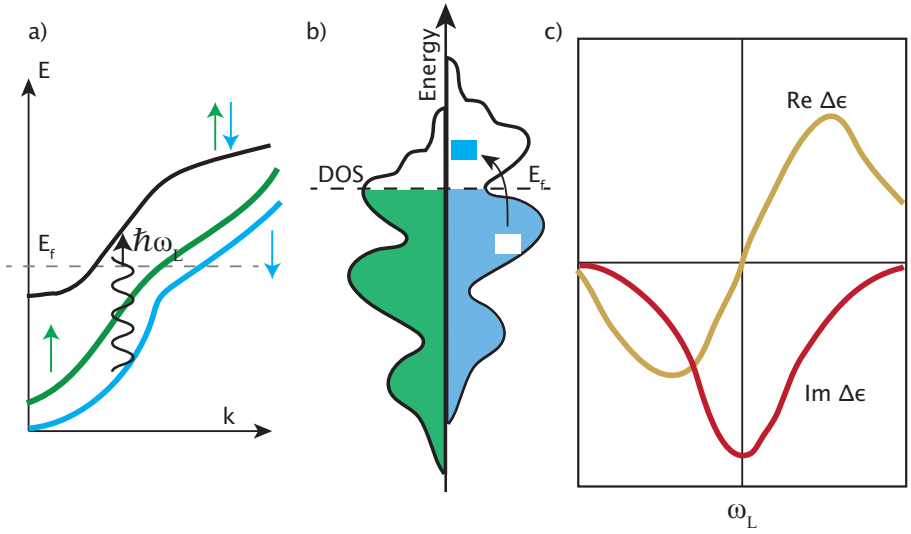


Figure 5.2: Illustration of the dichroic bleaching. (a) I assume that there is one possible excitation channel in the spin-down band and (b) the pump pulse excites only from the minority band and none from the majority band. (c) The modification in the real and imaginary parts of the off-diagonal elements of the dielectric tensor is shown while absence of demagnetization [41].

(6) The sixth and last example is about the dependency of MO signal to the crystalline orientation of a material. Koopmans et al. performed an experiment on magnetization dynamics of Ni film deposited on (111) and (001) Cu substrate [41]. Within the 400 fs, they see similar discrepancies in $\Delta\epsilon/\epsilon$ and $\Delta\theta/\theta$ in two samples as mentioned in the first example, Figure 5.1 (g). Surprisingly, even after one ps, these transient magnetization curves do not get together for two samples, because the excitation builds an uniaxial stress in the Ni layer which gives non-magnetic signal in the MOKE signal. Therefore, $F(t)$ contributes in MO signal even until 10 ps.

## 5.2 Electronic and Magnetic Contribution in XUV T-MOKE

Having many reports on the non-magnetic contributions in the MO response brings doubt also about the time resolved T-MOKE experiment probed via XUV photons. One crucial difference is that all reports mentioned above were performed with the optical pump-probe techniques. The wavelengths of the pump and probe beams are close to each other. After above reports, Zhang et al. showed that if one uses photons above 2 eV energy, the optical and magnetic coupling in MO response dies out [94]. Shortly later, Carva et al. showed the conclusion made by Zhang et al. is not true [18], and whatever wavelength used to probe magnetization in the optical range (probing conduction band with conduction band electrons) is going to give a non-magnetic contribution in the MO response. After all these controversies, we test whether the XUV T-MOKE experiments are artifact free or not. To find any artifact in MO response in T-MOKE experiment, I revisit the origin of the magnetic asymmetry term from Chapter 2. The s- and p-polarized reflected intensities were given

$$I_s = I_0 \left| \frac{\cos\theta_j - n\cos\theta_{j+1}}{\cos\theta_j + n\cos\theta_{j+1}} \right|^2, \tag{5.5}$$

$$I_p^{\pm} = I_0 \left| \frac{n\cos\theta_j - \cos\theta_{j+1}}{n\cos\theta_j + \cos\theta_{j+1}} \pm \frac{2iQ\sin\theta\cos\theta}{(n\cos\theta_j + \cos\theta_{j+1})^2} \right|^2, \tag{5.6}$$

respectively. Then, the magnetic asymmetry term was defined as

$$\mathbf{A} = \frac{I_p^+ - I_p^-}{I_p^+ + I_p^-} = 2\mathsf{Re}\left[ \frac{\sin 2\theta \epsilon_{xy}}{n^4\cos^2\theta - n^2 + \sin^2\theta} \right], \tag{5.7}$$

where $n$ is the refractive index, $\epsilon_{xy}$ is the MO constant or the off-diagonal element of the dielectric tensor, $\theta$ is the angle of incidence. We notice two important parameters that could effect the time resolved response in the magnetic asymmetry term: (1) is the refractive index $n$, (2) is the MO constant $\epsilon_{xy}$. Therefore, any change in $A$ would be associated with $n$ and $\epsilon_{xy}$ as

$$\frac{\Delta A(t)}{A_0} = \Delta\epsilon_{xy}\frac{\partial A}{\partial \epsilon_{xy}} + \Delta n \frac{\partial A}{\partial n}, \tag{5.8}$$

where the first term is proportional to the change in the magnetization and the second term gives the optical response or the optical artifact in the magnetic asymmetry term. If the second

term is zero or negligible, we can claim that XUV T-MOKE experiment is artifact free and it probes only the magnetic moment of a sample. In order to claim this, we must find out the change in the refractive index after an ultrafast excitation. Indeed, we essentially perform resonant-transient reflectivity experiments with the s-polarized XUV light. Beauty of the T-MOKE is that while we are sensitive to the magnetization and charge dynamics with p-polarized light, the s-polarized light gives only charge dynamics and optical response, as formulated in Equations 5.5 and 5.6. By finding the transient changes in the s-polarized light, we correlate this with a change in the refractive index,

$$\Delta I_s = \Delta n \, \frac{\partial I_s}{\partial n}. \tag{5.9}$$

After determining the change in the refractive index $n$, I use the Equation 5.8 to find the optical artifact in the magnetic asymmetry term. In Figure 5.3, I show the experimental results of transient reflectivity measurements with the s-polarized XUV light. Because HHG produces an ultra-broadband XUV spectrum that spans from 35 to 72 eV, we extract the dynamics at the $M_{2,3}$ absorption edge of Ni and other dynamics happening further away from this edge. After the pump beam arrives, the electronic system is excited and a non-equilibrium state gives rise to an increase in the reflectivity. At off-resonance, because XUV photons can not probe the conduction band of Ni, instead they probe the lattice response like an expansion in the lattice. The open-triangle symbols show this lattice response and start to raise after 1 ps which is much after electron-lattice relaxation starts. However, on-resonance XUV photons have a capability to probe conduction band of Ni and give the electronic and lattice dynamics together. The open-green squares show this combined responses which start right after the pump pulse. The increase in the green curve in the first ps is originated from purely electronic dynamics which does not show up in the off-resonance probe.

The total change in the reflectivity is around 0.2% within the first ps which is the time range we are interested in magnetization dynamics. To find the corresponding change in the refractive index, I plot the dependence of the s-polarized reflected intensity ($I_s$) as a function of $\delta$ and $\beta$, where $n = 1 - \delta - i\beta$, Figure 5.4. Approximately 0.1% variation in the $\beta$ results in 0.2% change

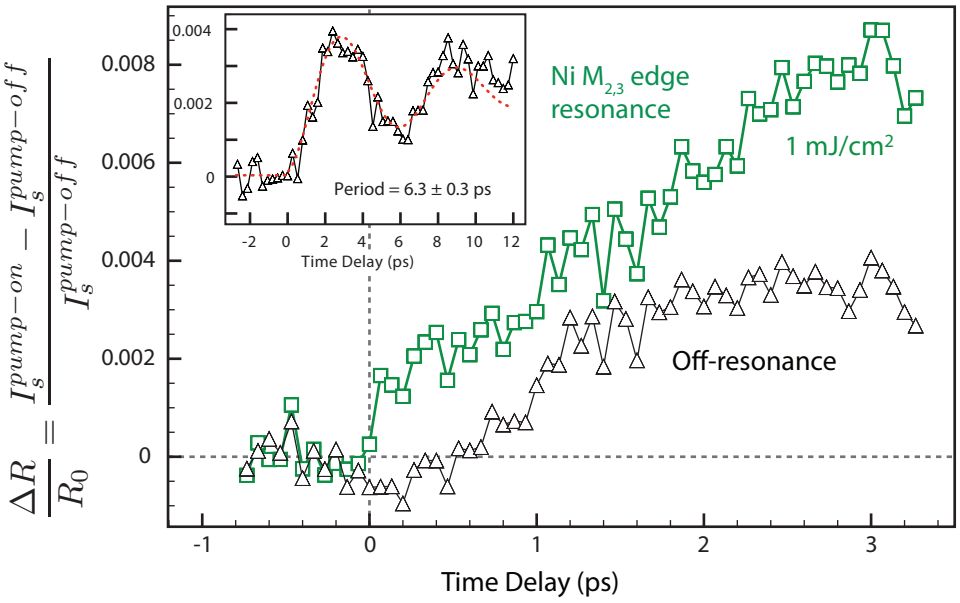


Figure 5.3: Transient reflectivity measurements of Ni film with s-polarized XUV light. White diamonds show the lattice dynamics used off-resonance photons and the lattice dynamics are relatively slow with respect to the electrons. However, on-resonance photons shown by the green shapes allow us to probe the electronic dynamics within the first ps that could give an artifact to the magnetic asymmetry. However, the amplitude of this electronic response is 0.2% which is two orders of magnitude smaller than the real magnetic response.

in the $I_s$. If I plot the same graph for $\delta$, which means finding the corresponding 0.2% change, the variation in $\delta$ would be 4%. Here, I show only for the $\beta$ because it is more related to the reflectivity. The refractive index is $1-\delta-i\beta$, so that the 4% change in the $\delta$ corresponds to $0.04 \times \frac{\delta}{1-\delta}$ change in the real part of $n$. At 67.7 eV M-edge of Ni $\delta \approx 0.01$, hence the transient change in the refractive index equals to 0.04%. Finally, the second term in the Equation 5.8 is not more than 0.1% and I show this non-magnetic variation in the asymmetry term in the case of $\Delta\epsilon_{xy} = 0$ by the purple squares in Figure 5.5. In addition to the s-polarized transient measurements, we performed four magnetization dynamics experiments with p-polarized light for four-different pump fluences. I show these results also in Figure 5.5 by the green, orange, blue and red curves for 0.3, 0.6, 1.6 and 2.4 mJ/cm$^2$ pump fluences, respectively. The deviation of purple squares from the unity is around 0.002 and clearly negligibly small. We also measured the magnetic asymmetry parameter with s-polarized light after the laser excitation and observed no variation shown by the black dots [47].

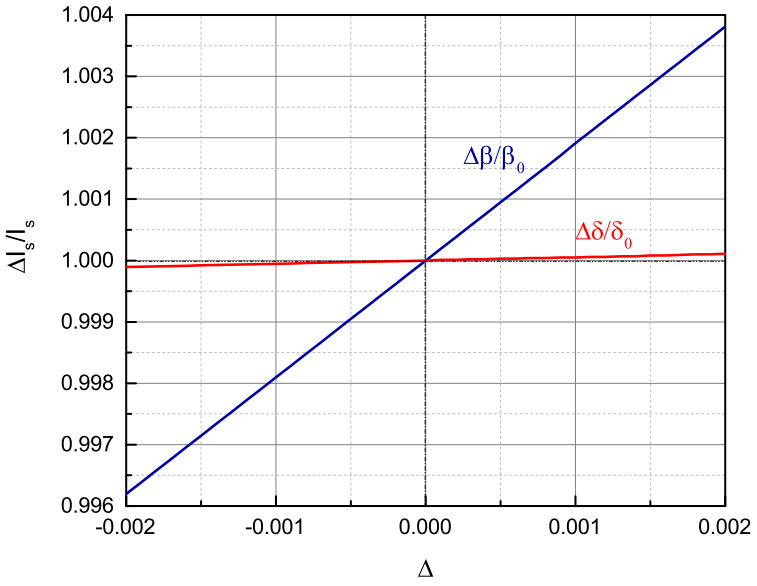


Figure 5.4: Theoretical calculation of the relationship between s-polarized reflectivity and the refractive index. Any 0.2% change in the s-polarized reflectivity can be result from 0.1% change in the imaginary part of $n$ or very large change in the real part of the $n$. We use $\Delta\beta$ which is more related to the reflectivity.

In conclusion, the MO response of the XUV T-MOKE experiment has an approximately 0.2% non-magnetic contribution in the 'magnetic asymmetry' term. This means that our method is perfect for probing ultrafast magnetization dynamics with a negligible optical artifact. In addition to the optical artifact investigation, we found another interesting physics in transient measurements. We scan the time delay between the pump and probe pulses upto 12 ps, then observe an oscillating dynamic as in the inset of Figure 5.3. First, this dynamic was unclear, but after analyzing the period of the oscillation, we find out the reason that is the generated acoustic waves by ultrafast excitation propagate in the grating structure and bounce back from the substrate. The propagation direction is longitudinal and these waves are called longitudinal acoustic waves (LAWs). I use exponentially raising and sinusoidally oscillating function to fit the experimental curve. The fitted period of the oscillation is found 6.3 $\pm$ 0.3 ps. Theoretically, one can also calculate the period by using the velocity of sounds in Fe and Ni gratings. The capping 3-nm-Ta layer on the Fe layers is taken into

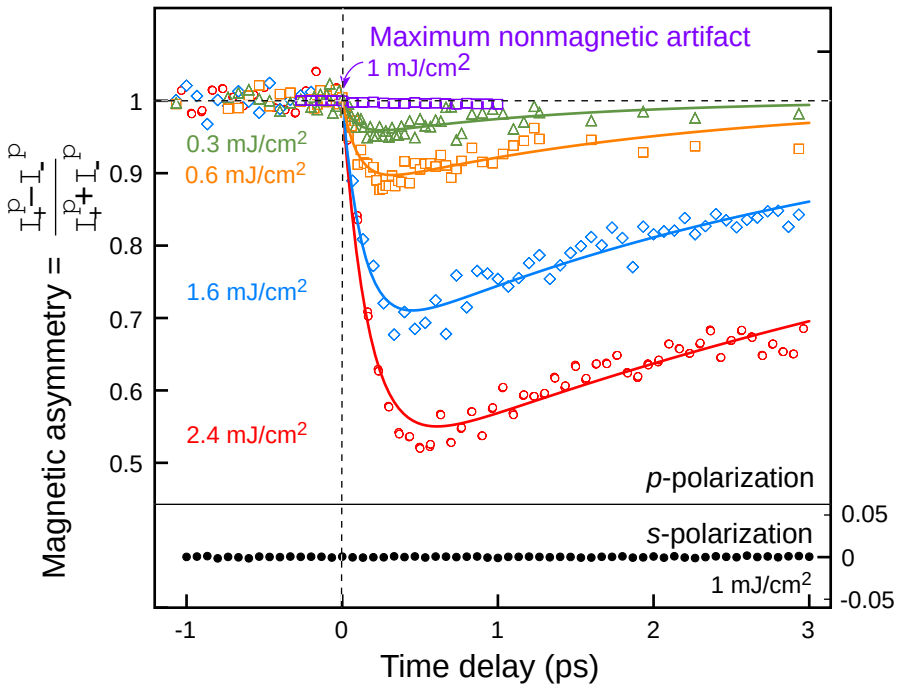


Figure 5.5: Magnetization dynamics at four-different pump fluences and non-magnetic artifact in the magnetic asymmetry. The green, orange, blue, and red curves show the ultrafast demagnetization dynamics for 0.3, 0.6, 1.6, and 2.4 mJ/cm$^2$ pump fluences. We also performed the magnetic asymmetry measurements with s-polarized XUV light which gives zero signal shown by the black squares. By using the extracted change in the refractive index from the 5.3, we find the contribution in the magnetic asymmetry. The purple curve shows this negligible optical contribution in the magnetization dynamics.

account. The longitudinal sound velocities in Ni, Fe and Ta are 5489 m/s, 5960 m/s and 3956 m/s, respectively. A round-trip of a LAW takes approximately 5.16 ps in the Fe grating and 6.16 ps in Ni grating. After assuming some oxide layers on the top, these numbers are in a good agreement with the experimental findings. Moreover, the determination of the period of LAW in a ultrathin films turns out very precise with our technique and this opens new experimental possibilities to characterize ultrathin films without distortion or damaging.

Thus far I experimentally show that a non-magnetic contribution in the magnetic asymmetry is not more than 0.2%. However, we missed one mathematically phenomenological fact in the above calculation which is pointed out by Vodunghbo et al. [87] and published as a comment to our [47].

I represent the Equation 5.9 numerically in the Figure 5.4 for specific energy point and the

refractive index. If one calculates the Equation 5.9 analytically, finds

$$\frac{\partial I_s}{\partial n} = \frac{\partial}{\partial n}(EE^*) = \frac{\partial E}{\partial n}\left(E^* + E\frac{\partial E^*}{\partial E}\right), \tag{5.10}$$

where $E$ is the electric field of the s-polarized light and $E^*$ is the complex conjugate of this field. Mathematically, $\frac{\partial E^*}{\partial E}$ is not valid. Hence, $\frac{\partial I_s}{\partial n}$ term can be very complicated and in some scenarios it could be zero and infinite amount of change in the $n$ results in zero change in $I_s$. In other words, the $\delta$ and $\beta$ terms in the refractive index can vary in such a way that the magnetic asymmetry deviates extremely but the s-polarized reflectivity remains unaffected. I call these unaffected reflectivity values as isoreflectivity curves in $\delta\beta$ space. Of course, this argument is purely mathematical and by plugging the right material and experimental values into, one reaches similar conclusions as in [47]. However, we are experimentalists and we prove the stuff with the real measurable-physical things, instead of speculations.

The first idea to disprove this argument is to measure the transient reflectivity with p-polarized XUV light. If we find how the first nonmagnetic Fresnel term in the Equation 5.6, we can confine the $\delta\beta$ space from two dimensions and disprove the argument. Because, the confinement of $\delta\beta$ space with only $I_s$ measurements in [47] was only in one dimension, but $\delta$ and $\beta$ can vary in other dimension. By measuring $\Delta I_p$, the another constrain would be placed and the phenomenological argument by Vodungbo invalidates. One experimental challenge in this solution is that the reflected p-polarized XUV always has a magnetic contribution because of the second term in the 5.6. We try a different experimental manner, but the second and higher order terms of $\epsilon_{xy}$ would survive and give a magnetic contribution in the transient measurements. Actually, this is a interesting point to further investigation. Thus far, an optical artifact in MO signal have been studied, but nobody has done an investigation on magnetic artifact in the optical signal. This is not the scope of my thesis and leave for other studies and I continue for the disprove to comment of Vodungbo et. al. [87].

However, there is a simpler and even direct answer to the argument. There is one more parameter we have not mentioned in the Equation 5.7 that is the angle of incidence $\theta$. By varying

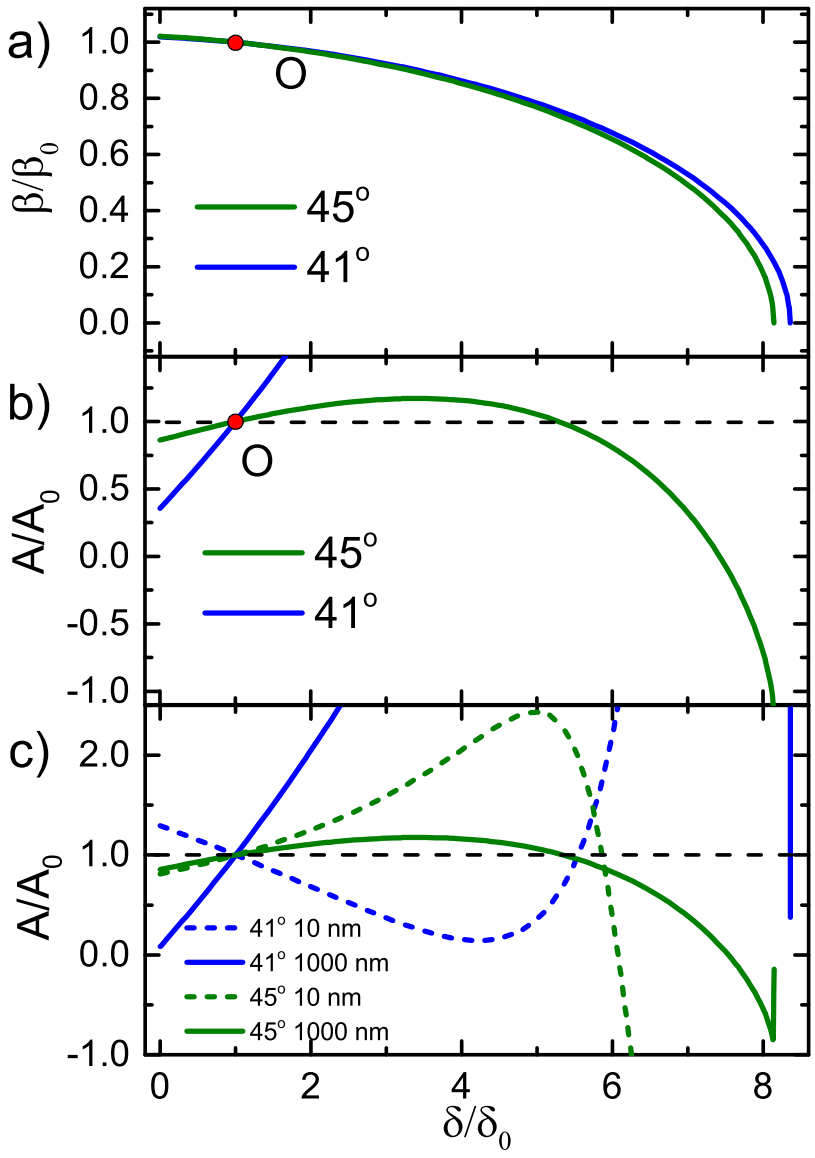


Figure 5.6: Theoretical calculations of the reflected s-polarized and magnetic asymmetry in case of phenomenological change in the refractive index. a) Iso-reflectivity curves for angle of incidences 41° and 45° as a function of $\delta$ and $\beta$. b) An artificial asymmetry dynamics for variation of $\delta$ and $\beta$ as in (a) without changing $\epsilon_{xy}$. The comment claims that remaining constant of the s-polarized reflectivity does necessarily not mean that the electronic artifact is negligible at 45°. However, this claim can be disproved by measuring magnetization dynamics at a different angle. c) Similar calculation as in (b), but for a 10-nm and 1000-nm thich Ni samples. The asymmetry behavior changes quantitatively, nonetheless the green and blue curves still qualitatively differ a lot.

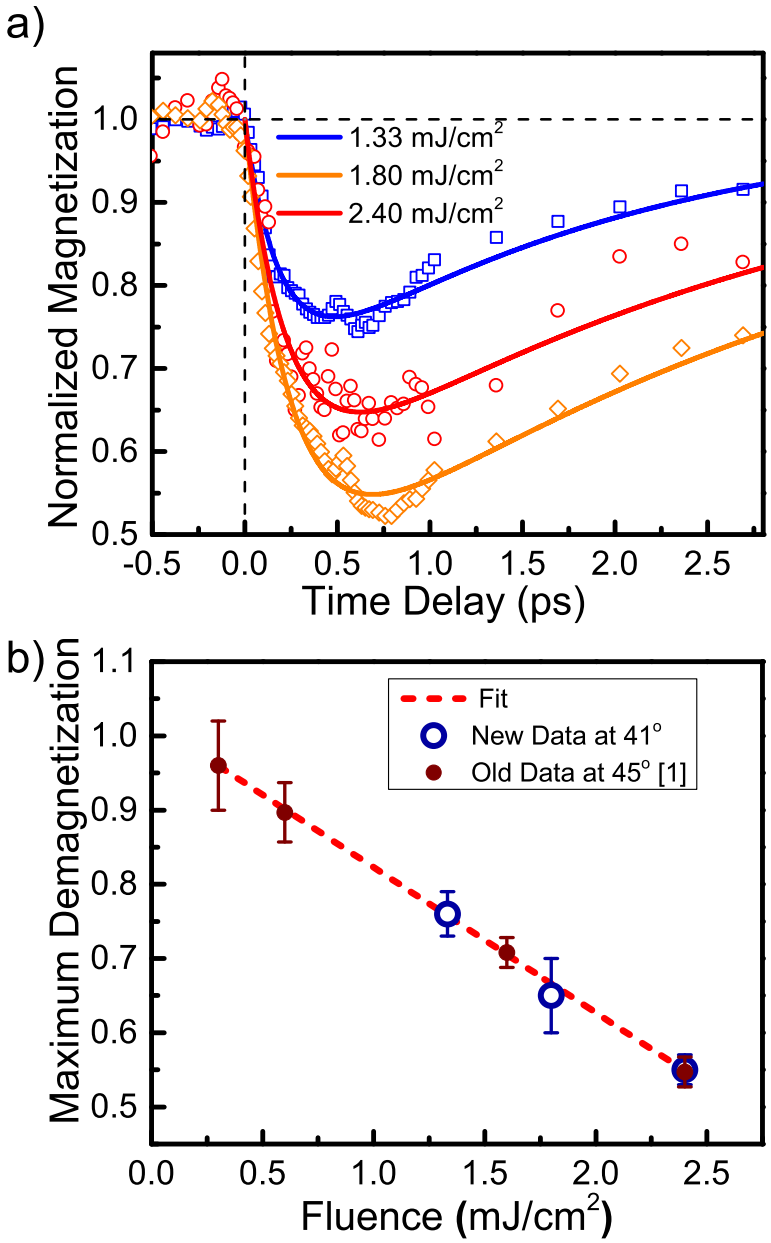


Figure 5.7: Magnetization dynamics of Ni at an agnle of incidence 41° with different pump fluences. a) Normalized magnetization dynamics show an exponential decay after an ultrashort laser excitation. b) Maximum demagnetization is proportional to the pump fluence independent of the angle of incidence. This disproves the comment by Vodungbo et al. [87] and our conclusion of the original paper remains unaffected [47] [82].

the angle of incidence from 45° to 41°, we disprove the argument pointed out by Vodungbo et al. and publish as a reply [82]. I show the theoretical calculations and additional experimental results in Figure 5.6 and 5.7, respectively. As I mentioned before, a variation in $\beta$ and $\delta$ in a specific trajectory shown by the green curve in Figure 5.6 a) for the 45° without changing the $I_s$. But the magnetic asymmetry would change as in b) again shown by the green curves. Nonetheless, I can calculate similar trajectories for an angle of incidence 41°. Surprisingly, the similar trajectory in $\beta$ and $\delta$ that requires to keep $I_s$ constant results in completely different the magnetic asymmetry shown by the blue curves in a) and b) at 41°. In these calculations, the changes in the $A/A_0$ is originating only from $\delta$ and $\beta$ variation but $\epsilon_{xy}$ stays constant. If these behaviors shown in Figure 5.6 a) and b) were true as argued by Vodungbo, time resolved magnetic asymmetry dynamics at 41° should stay on the blue curve in the Figure 5.6 b). On the other hand, the experimental results completely rule out the argument as shown in Figure 5.7. The demagnetization curves at three different pump fluences at 41° are shown by the orange, red and blue symbols with guide to eye curves. In contrary to the argument, the demagnetization amount is very similar to the ones at 45°. I compare the new demagnetization amounts as well as the previous amounts and plot as a function of pump fluence, in Figure 5.7 b). The demagnetization amounts are fitted smoothly by a line which means that the change in the magnetic asymmetry is proportional to the excitation energy. In other words, the magnetic asymmetry term is linearly proportional to the $\epsilon_{xy}$, not the the refractive index nor $\delta$ nor $\beta$. This means that such a complicated dependence of the magnetic asymmetry to the $\delta$ and $\beta$ could not give such a linear behavior with the excitation energy. It is only possible and makes sense, if the magnetic asymmetry is only proportional to the $\epsilon_{xy}$ or the magnetization of a sample. Non-magnetic artifact in the MO response of XUV T-MOKE experiments is to be less than 1% which is the uncertainty of experimental determination of the demagnetization amount. In other words, the speculated optical contribution in magnetic signal is smaller than the noise level of the magnetic-asymmetry measurements.

The last point to mention is that Vodungbo et al. additionally mentioned the Equation 5.7 is only valid for the semi-infinite magnetic media not for the sample used in the experiment. I simulate

similar isoreflectivity and magnetic-asymmetry variation in $\beta\delta$ space, the asymmetries at 41° and 45° would behave quite differently for a 10-nm-Ni thin film shown in Figure 5.6 c). Vodungbo et al. noticed an oversimplification of the magnetic asymmetry term; however, the assumption made by semi-infinite sample would not change the conclusion of our paper, only a matter of mathematical procedure.

## 5.3 Conclusion

In summary, I first give six-example investigations performed on possible optical artifacts in the MO response during the ultrafast demagnetization dynamics. The major shortage of the optical pump-probe experiments is coming from the use of similar wavelengths of light for the pump and probe beams. Fortunately in our experiment, I use XUV photons to probe magnetization and infrared pulses to excite the samples, which gives an enormous advantage. Second, I examine the XUV T-MOKE technique experimentally and theoretically whether there is any optical or electronic artifact in the magnetic asymmetry. I studied the transient reflectivity dynamics with the s-polarized light and time-resolved magnetic asymmetry dynamics at a different angle of incidence. Consequently, after all careful analysis, we report that T-MOKE geometry by employing high-harmonic generation probes only the magnetic state of a material in addition to ultrafast-temporal and nanoscale-spatial resolution on a tabletop.

# Chapter 6

# Ultrafast Magnetization Enhancement in Multilayers by Spin Currents

## 6.1 Introduction

Complication of correlated electron dynamics in ferromagnets and unanswered questions about ultrafast demagnetization process attracted many researchers. Having one of the best magnetization probes allows us to study comprehensive dynamics at different samples with very precise temporal resolution. After proving our technique is artifact-free, we studied element selective ultrafast dynamics in the permalloy ($Ni_{80}Fe_{20}$). We probed the strong exchange interaction between Ni and Fe atoms by distinguishing demagnetization in Ni and Fe, for the first time. We also controlled this exchange interaction by diluting the permalloy with Cu that results in different demagnetization dynamics. While, Ni demagnetization lags behind the Fe demagnetization about 12 fs in the pure Py, this lag increases to the 60 fs for the PyCu [49].

Next, we investigate magnetic multilayers because of remarkable technological impacts of multilayers in data-storage devices. Studies of magnetic multilayers triggered to discovery of giant-magneto resistance (GMR) which is heavily used in data storage and spintronics applications [31]. GMR is governed by the large resistivity difference of a multilayer structure depending on the alignment of magnetic layers. Furthermore, the alignment of magnetic layers is originating from an interlayer exchange interaction between the magnetic layers. Before I report our experimental results, I explain magnetic multilayers and interaction in them.

### 6.1.1 Interlayer exchange

In 1955, Ruderman, Kittel, Kasuya, and Yosida showed an oscillation of spin polarization by the conduction electrons as a function of distance which survives even for large distances relative to the lattice constant. Later, this nature of spin was called RKKY interaction and successfully explained the direct-exchange magnetization in $4f$ metals, Figure 6.1a. The RKKY exchange also is very useful to understand interlayer-exchange interaction in magnetic multilayers [31, 78]. Advancing in material fabrication methods allows production of ultrathin multilayers with high-quality to study exchange interactions in very small lateral spaces. For example, when two ferromagnetic layer are separated by a non-magnetic metal spacer (NiFe/Ru/NiFe), exchange coupling of ferromagnetic layers oscillates and decays as a function the thickness of the non-magnetic spacer layer as in

$$J_{12}(z) = J_0 \frac{d^2}{z^2} \sin(2k_F z). \tag{6.1}$$

I show this induced-spin density waves in Figure 6.1b for NiFe/Ru/NiFe multilayers [78]. When the ferromagnetic layer are close to each other, the exchange energy $J_{12}$ is negative and favor of antiferromagnetic alignment. Depending on spacer material and magnetic moments of ferromagnetic layers, the wavevector $k_F$ determines ferromagnetic coupling for certain thicknesses. As increase in the thickness, the coupling oscillates between antiferromagnetic and ferromagnetic states[57].

After studying direct exchange in permalloy, we investigate ultrafast magnetization dynamics in multilayer which would be very promising in technological applications[65].

## 6.2 Multilayer fabrication and characterization

Our samples are made of Al(3 nm)/Ni(5 nm)/Ru(x)/Fe(4 nm)/Ta(3 nm) layers, where the Ni/Ru/Fe trilayer exhibit an interlayer exchange- coupled magnetic system, as shown in Figure 6.2 (top). The top Si3N4 grating structure serves as a grating spectrometer as explained in Section 3. We carefully characterize the magnetism in our samples using a superconducting quantum

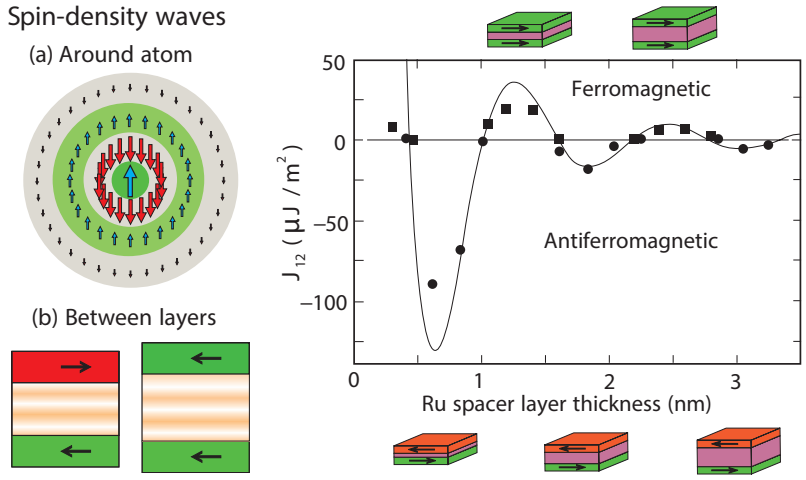


Figure 6.1: Representation off spin waves around an atom and between magnetic layers, taken from [78]. a) Polarized spin waves in an atom oscillate in space and decay at relatively long distances. This long-distance interaction explains the direct-exchange magnetization in $4f$ metals. b) This wave nature of spins also occurs in magnetic layers. For instance, thickness-varied Ru layer is sandwiched by NiFe magnetic layers and the orientation of NiFe layers measured. Hence, the relative alignment and the strength of the coupling of magnetic layers show a decaying oscillation trend as a function of thickness of Ru layer.

interference device (SQUID) magnetometer. These data show the effect of the thickness of Ru spacer layer on the interlayer exchange-coupling between Ni and Fe ferromagnetic layers: a 1 nm thick Ru layer results in a ferromagnetic alignment of Ni and Fe, which alters to antiferromagnetic alignment for a 1.5 nm Ru layer thickness.

## 6.3 Static Magnetic Asymmetry

The magneto-optical response of our trilayers is measured via the transverse magnetooptical Kerr effect (T-MOKE) in XUV spectral range. The magnetic asymmetry was defined in 2 Equation 2.21. The resonantly enhanced static magnetic asymmetry at the Fe and Ni 3p absorption edges (52 and 66 eV, respectively) is assigned to the magnetic state of the Fe and Ni layers, Figure 6.2 (bottom). For our Ni/Ru/Fe trilayer, the amplitude of the magnetic asymmetry is around 10% at the Fe absorption edge and 20% at the Ni 3p edge. By adjusting the external magnetic field, we can tune the trilayers into two well-defined magnetic states: (1) parallel orientation of the Ni and Fe layers shown by the pink asymmetry curve, and (2) antiparallel orientation shown by the orange asymmetry curve. A comparison of the magnetic asymmetries corresponding to the two states shows that the relative sign of the Ni and Fe asymmetries reverses in these two cases.

## 6.4 Magnetization Dynamics

We capture spin transport and magnetization dynamics in our multilayer sample, after the sample is excited with ultrashort pump laser pulses of 1.6 eV photon energy. The magnetization in the each individual layer was then probed simultaneously by monitoring the amplitude of the T-MOKE magnetic asymmetry as a function of time delay between the pump and probe pulses. We estimate the amount of the pump light reaching the individual layers by a self-consistent 2× 2 matrix calculation. Then, we find that the Al cap and Ni layer together absorb ¿58% of the incident light. This is 2.5 times as much as the Fe layer does.

The layer-selective time traces of the magnetic asymmetries at the 3p absorption edges of Fe and Ni, at fluencies of F $\approx$ 2 $mJ/cm^2$, are plotted in Figure 6.3. Similar to earlier experiments

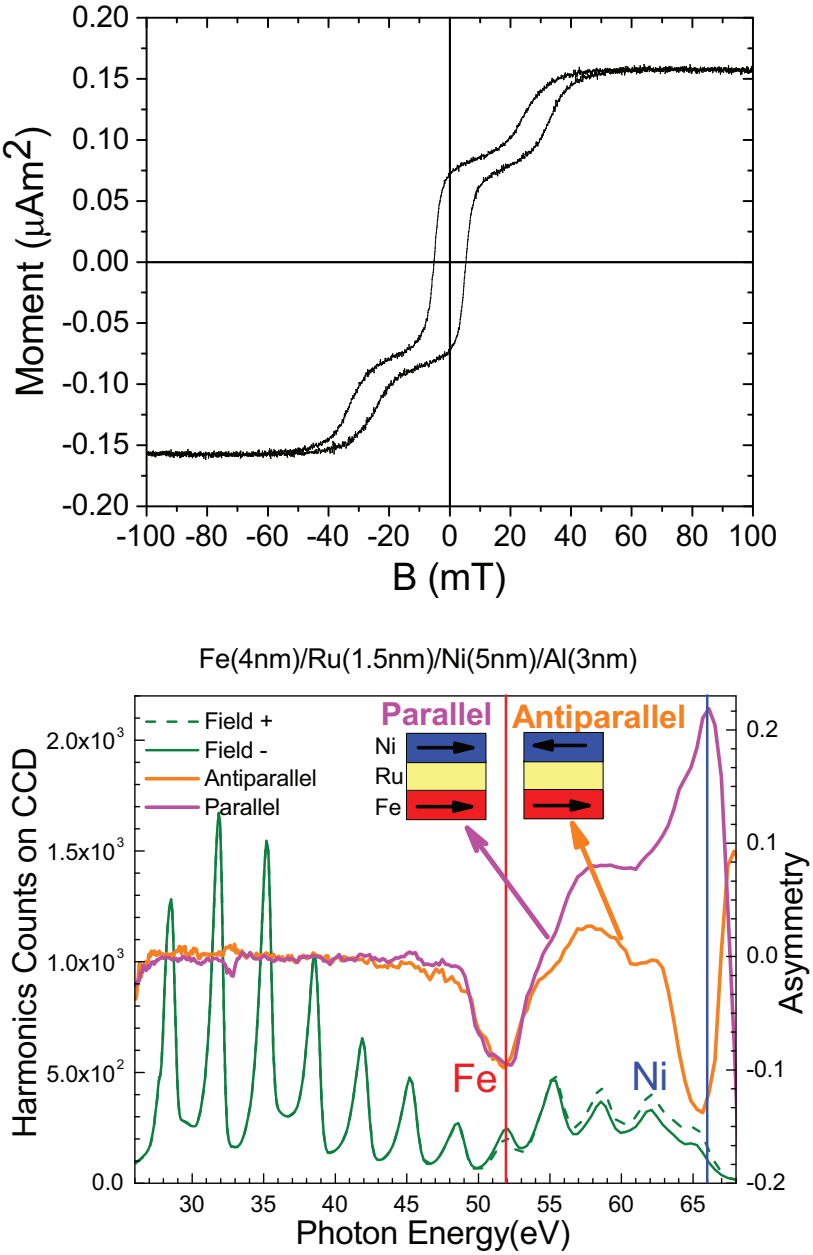


Figure 6.2: Static-magnetization profile of Fe/Ru/Ni multilayer. (Top) A superconducting quantum interference device (SQUID) magnetometer used to measure the total magnetic moment and the hysteresis of the sample. At the saturation magnetic field two layers are aligned parallel, while they are antiparallel around 20 mT magnetic field. (Bottom) These two alignments are also observed with our T-MOKE setup by magnetic asymmetry. When a strong or weak magnetic field is applied, two layers are parallel or antiparallel, shown by the violet and the orange curves, respectively. The magnetic asymmetry has opposite peaks for the parallel alignment which might mislead to antiparallel alignment. However, the magneto-optical signal of multilayer structure could be very complicated, and give unexpected static asymmetries.

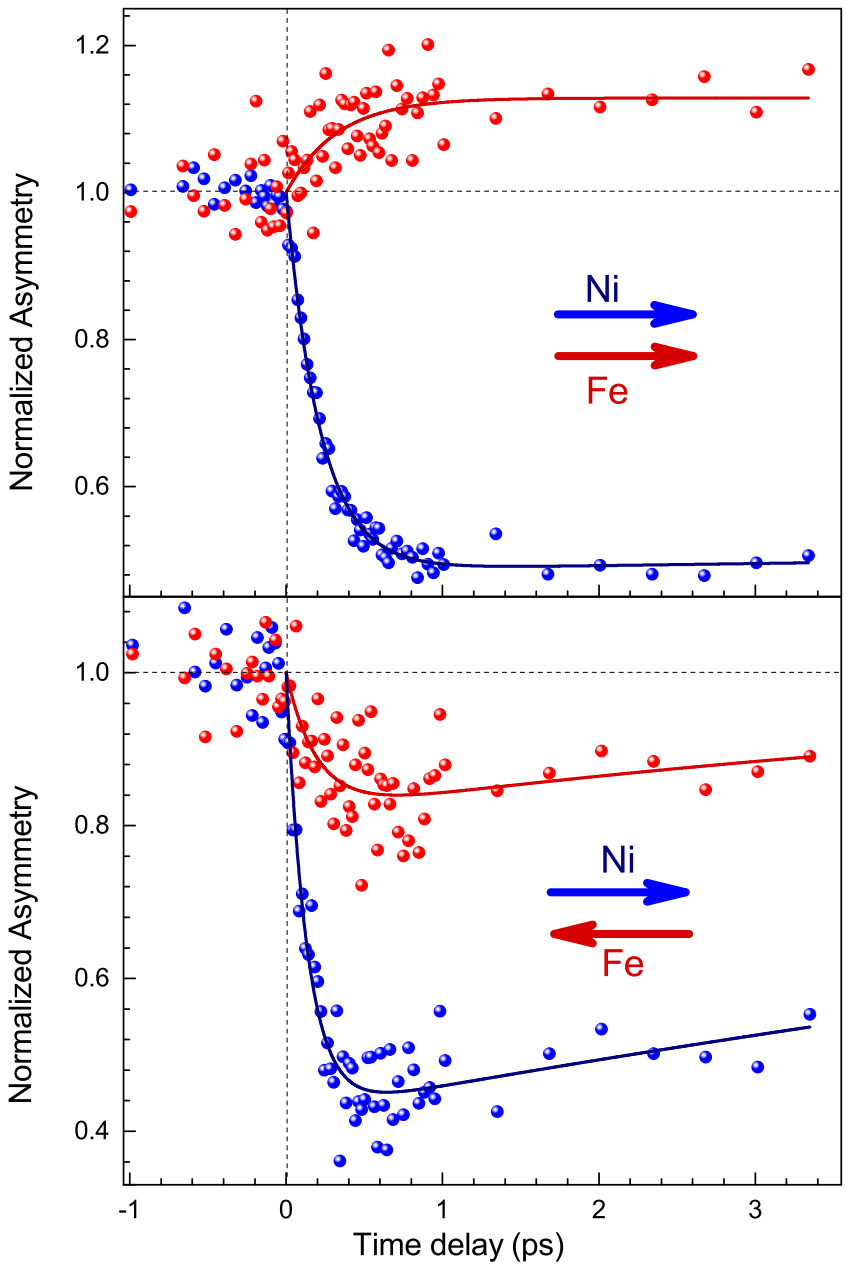


Figure 6.3: Ultrafast magnetization curves of Ni and Fe as a function of pump-probe time delay. Surprisingly, Fe magnetization increases while Ni demagnetizes for the parallel alignment (top). On the other hand, Fe magnetization dynamic differs quite a bit when the layers are antiparallel, while Ni demagnetize as in the top. This distinct difference is a strong sign of a spin transport from the top-Ni layer into the bottom-Fe layer.

[46, 47], we observe a demagnetization in the Ni layer. Surprisingly, we also observe either an enhancement or reduction of the Fe magnetization depending on the relative magnetization orientation of the Ni and Fe layers (see Figure 6.3): if the Fe and Ni layers are initially oriented antiparallel, then the magnetization of both Ni and Fe decreases. On the other hand, if the two layers are oriented parallel by an external magnetic field, we observe that the Fe magnetization increases 15% above its equilibrium value on a similar timescale.

## 6.5 Superdiffusive spin transport

This first observation of an ultrafast magnetization enhancement in the Fe layer can be explained by superdiffusive spin transport [7, 6], which takes place on timescales comparable to the demagnetization processes explored in earlier works [9]. The mechanism we propose for enhancement of the magnetization is based on filling of majority spin states above the Fermi energy in the Fe layer by majority spins coming from Ni. This leads to a transient magnetization increase in the Fe layer, above its maximum value. The increase in the magnetic signal from the Fe layer is a result of a strong asymmetry in the spin-dependent hot-electron lifetimes in magnetic materials as explained in Section 4.4.3 superdiffusive spin currents. Hence, the transport properties of the hot majority and minority spin carriers within the Ni and Fe layers [97, 96]. Excited minority spin electrons originating in the optical excitation in both the Al and Ni layers have much shorter lifetimes when passing via superdiffusion through the Ni layer, and are therefore stopped before they can reach the Fe layer. In contrast, majority-spin electrons have much longer lifetimes in Ni and are able to reach the Fe layer by superdiffusion.

Next, we solve the superdiffusion spin-transport equation (section 4.4.3) for electrons excited by a laser pulse of 25 fs and 1.6 eV photon energy in the Al, Ni and Fe layers. Then, we predict the transient, layer-specific, normalized magnetizations shown in Figure 6.4. The transient response of the Fe layer depends on the initial relative alignment of the Ni and Fe layers: for antiparallel configuration, the stream of spin-majority electrons decreases the net magnetization in the Fe layer by increasing the amount of spin-minority electrons in Fe. In contrast, for parallel configuration,

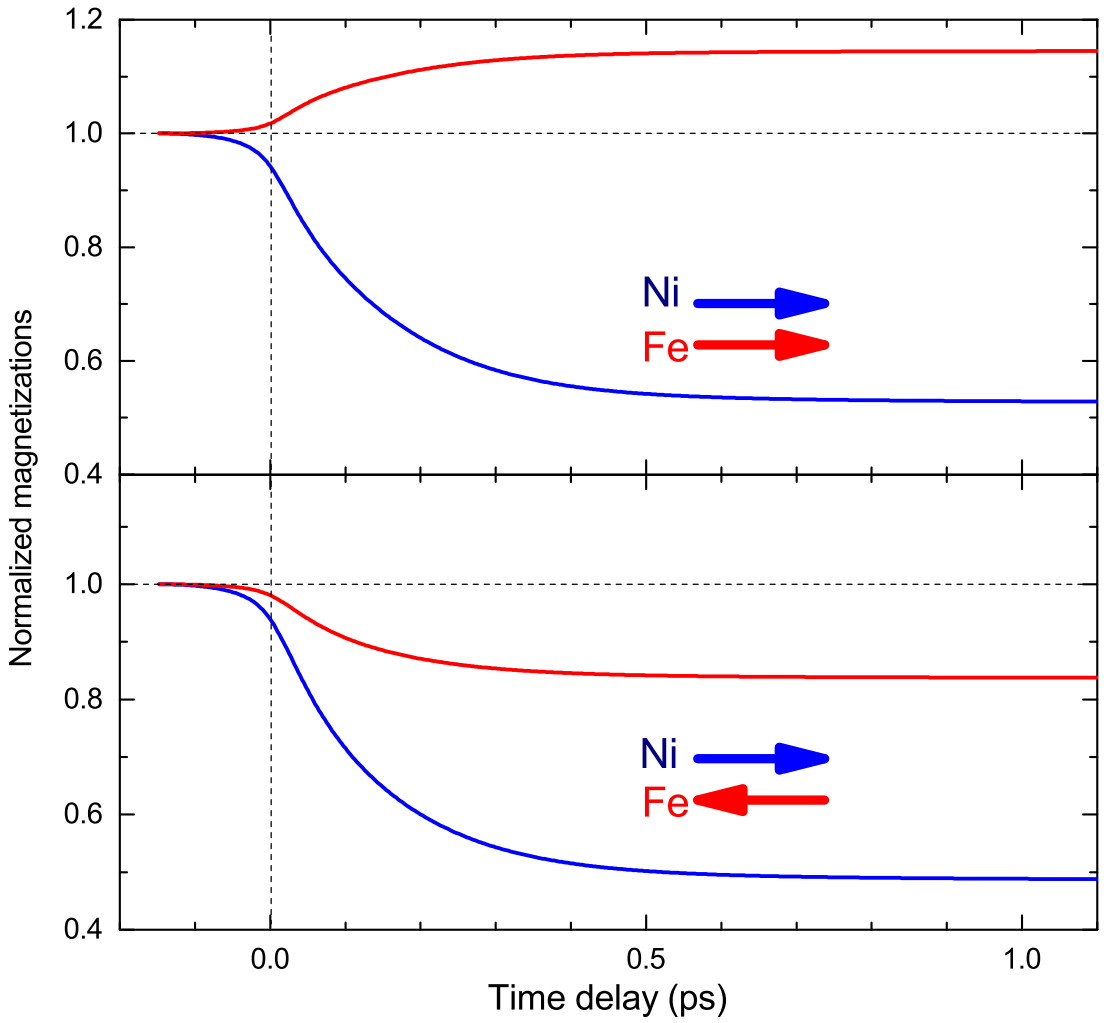


Figure 6.4: Calculation of spin currents between Ni and Fe layer for our experimental parameters, but neglecting a spacer layer. These magnetization dynamics agree very well with the experimental measurements. These effective 'net' spin currents result from the asymmetry in spin dependent-lifetimes in Ni as shown in Figure 4.7

the superdiffusive spin current of spin majority electrons through the interface increases the number of spin-majority electrons in Fe, thus enhance the Fe magnetization and causing opposite polarities in the femtosecond magnetization response of Ni and Fe layers.

## 6.6 Discussion

Several competing processes have been proposed for ultrafast magnetization dynamics [39, 36, 17, 93, 6, 11, 1, 50]. For the trilayer systems explored here, we find that the observed magnetization dynamics in the Ni and buried Fe layer is consistent with superdiffusion of excited spin-majority electrons that originate in the Al and Ni layers. The experimental data (Figure 6.3) agree well with theoretical predictions of superdiffusive spin transport (Figure 6.4)both in terms of the timescales as well as the magnitudes of the demagnetization ( 15% for Fe and 50% for Ni) and anomalous magnetization increase in Fe ( 15%). We note that we have not included spin dissipation channels such as electron-phonon and electron-electron spin-flip scattering in our model. This excellent agreement between theory and experiment thus shows that superdiffusion is the dominant process for the observed spin dynamics in the Ni and Fe layers under the chosen experimental conditions.

The anomalous enhancement of the Fe magnetization is most prominent at relatively low excitation fluence, below F $\approx 2.0 mJ/cm^2$. We find that at higher fluence, direct optical excitation of the Fe layer becomes the dominant source of demagnetization, that is, by increasing the excitation fluence to F $\approx 2.7 mJ/cm^2$, we observe the Fe magnetization to decrease after the excitation, even when the Ni and Fe magnetizations are parallel, as shown in Figure 6.5. This observation confirms that there has to be untold story about spin currents and it is not one and only mechanism at ultrafast demagnetization. In contrast, when we reduce the pump fluence to F $\approx 1.3 mJ/cm^2$, we again observe an increase or decrease of magnetization in Fe due to superdiffusive spin transfer.

## 6.7 Conclusion

In summary, we are able to elucidate the contribution of spin superdiffusion to the process of ultrafast spin dynamics. Spin superdiffusion leads to a remarkable and counterintuitive mag-

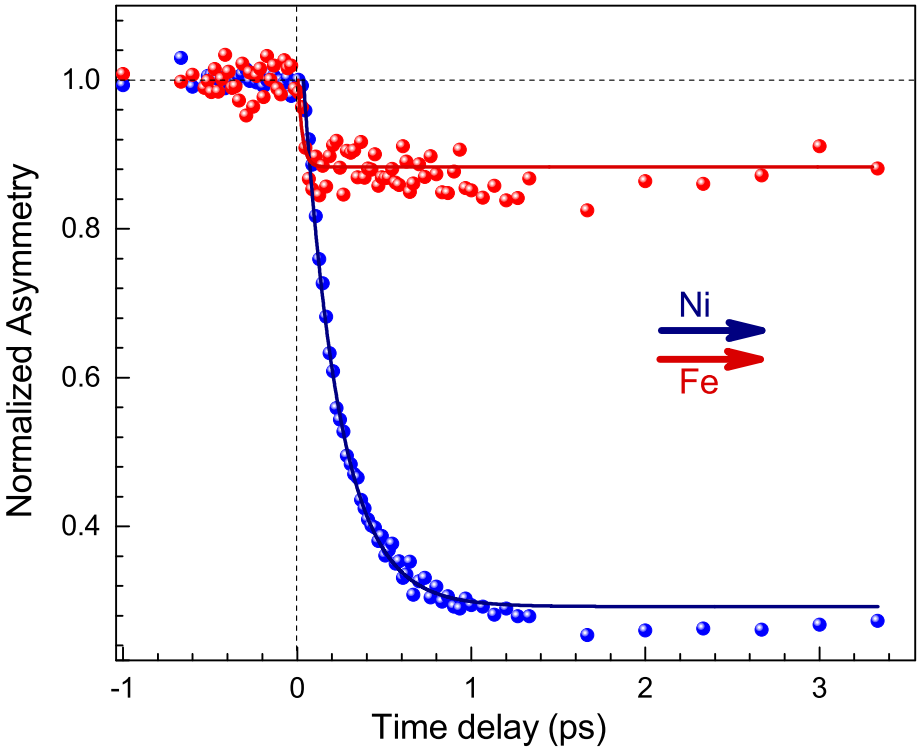


Figure 6.5: Ultrafast magnetization dynamics of Fe/Ru/Ni multilayer in the case of high-pump fluence. In contrast to Figure 6.3, Fe demagnetizes after the ultrashort laser pulse. This indicates that the spin currents are not dominant anymore and the spin-flip scattering mechanisms take place more.

netization enhancement in Fe in response to optical pumping when the Ni and Fe magnetizations are initially parallel. Our discovery provides fundamental insight into spin dynamics on femtosecond timescales, and is relevant for identifying the mechanisms underlying ultrafast spin dynamics. We note that our data demonstrate an ultrafast transfer of angular momentum of longitudinal spin through a spin current on subpicosecond timescales. In contrast, previous works demonstrated spin-transfer torque, that is, a transfer of transverse angular momentum between noncollinear spins and a magnetic moment at microwave frequencies [54], leading to important innovations such as spintorque magnetic random access memory (RAM) for data storage, spintorque oscillators for

frequency-agile telecommunications, and spinwave interconnects for spin-based logic. Similarly, we anticipate that superdiffusive spin transfer, which has a considerably larger magnetic moment, can find applications in moving domain walls, switching magnetic nano-elements on subpicosecond timescales or in spin-based electronics operating in the Terahertz frequency range.

# Chapter 7

# Moderation of Ultrafast Spin Current Propagation

## 7.1 Introduction

In the previous chapter, superdiffusive spin currents explain two magnetization dynamics in Fe/Ru/Ni multilayers. However, I also show that the ultrafast spin currents fail to explain dynamics in high-fluence pump data, Figure 6.5. Furthermore, spin-flip scattering has been studied for two decades with a great success and can not be disregarded.

To investigate more about spin currents, in this chapter, I use multilayers of Fe and Ni with different metals and insulators as the spacer material to conclusively show that both optically induced demagnetization, due to spin scattering processes, and spin-currents contribute simultaneously to ultrafast dynamics in magnetic materials. Moreover, I can control the competition between these two processes, and in some cases completely suppress interlayer spin currents as a sample undergoes rapid demagnetization. Finally, by reversing the order of the Fe/Ni layers, I experimentally show that spin-currents are directional in our samples, predominantly flowing from the top to the bottom layer [83].

## 7.2 Samples

The multilayer samples consist of substrate/Ta(3 nm)/Fe(4 nm)/X/Ni(5 nm)/$Si_3N_4$, where X is the spacer layer. The $Si_3N_4$ is used as a capping layer to prevent oxidation of the top layer. The spacer layer X is either a spin transmitter (Ru), a spin scatterer (Ta or W), or an insulator ($Si_3N_4$) [52, 3]. Samples are fabricated on a $SiO_2$ substrate by dc-magnetron sputter deposition.

The Ta adhesion layer promotes a uniform texture of the multilayers. The $Si_3N_4$ diffraction grating ($\approx$ 12 nm) is lithographically patterned on top of the multilayers in order to spectrally disperse the XUV harmonics, which are focused by a toroidal mirror onto a charge-coupled device (CCD) camera. The element-specific T-MOKE signals of both Fe and Ni were simultaneously detected and are clearly distinguished (Figure 7.1) allowing for layer-selective investigation of multilayer stacks in the XUV.

## 7.3 Results

When optically pumped, the observed magnetization dynamics depend critically on the spacer layer. With 1.7 nm of Ru, there is an abrupt reduction of $68 \pm 1\%$ in the Ni asymmetry, Figure 7.2. Such demagnetization is typical of optically excited magnetic systems, as has been extensively studied for two decades. In contrast, the Fe asymmetry increases, by $16 \pm 1\%$, indicative of a magnetization enhancement as shown in the previous chapter.

To experimentally explore the contributions of spin-flip scattering and spin transport processes to optically induced demagnetization, we fabricated multilayer samples with Ta and W spacers, which have spin diffusion lengths ($l_s$) of only a few nanometers [3, 52] (in contrast to $l_s = 14$ nm for Ru [23]). Then, to strongly suppress the contribution of spin diffusion to the dynamic magnetic response, I used an insulating spacer of $Si_3N_4$. (I note that reported values for $l_s$ are measured at the Fermi energy $E_F$. While it is not yet known how the $l_s$ depends on energy above $E_F$, I expect a weak dependence of $l_s$ on energy under the assumption that spin-flip is due to Elliot-Yafet scattering from defects with large spin-orbit coupling.) These samples with different spacer materials permit us to distinguish between the ultrafast spin-transport and spin-flip scattering mechanisms; I expect a weaker or absent enhancement of the Fe magnetization when a spin scatterer or insulator is placed between the Ni and Fe layers.

Figure 7.2 show the measurement results for these samples in the case of parallel Ni and Fe magnetizations and nearly identical pump fluences. For all three samples, the magnetization of Ni decreases by $\approx 50\%$ at similar rates, while the magnetization of the Fe layer decreases by $13 \pm 1\%$

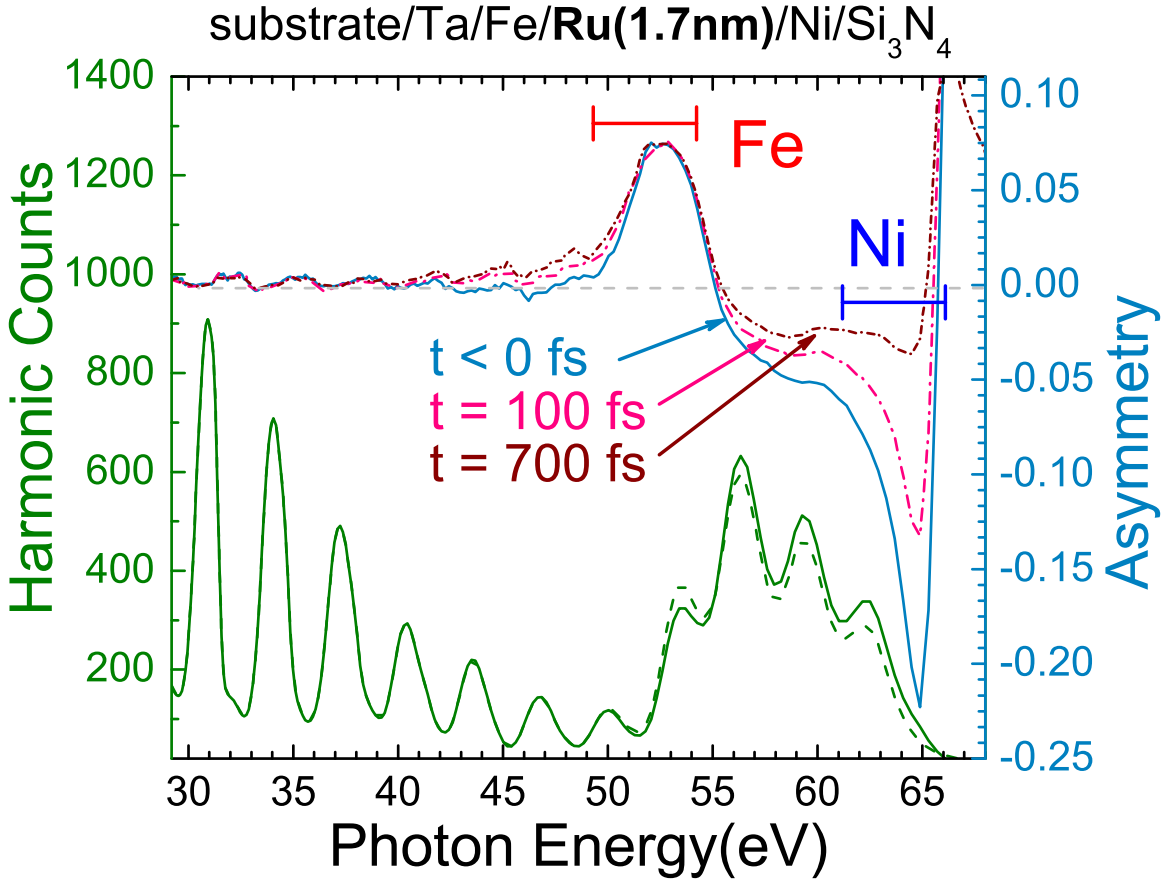


Figure 7.1: Temporal evolution of the magnetic asymmetry and the reflected XUV spectrum of a substrate/Ta(3 nm)/Fe(4 nm)/Ru(1.7 nm)/Ni(5 nm)/$Si_3N_4$(6 nm) multilayer. The solid and dashed green curves represent the reflected XUV intensities upon reversal of the external magnetic field. The light blue curve denotes the derived static (no pump) magnetic asymmetry, which is maximum at the $M_{2,3}$ absorption edges of Fe (red bar) and Ni (blue bar) and linearly proportional to the magnetization. The pink and the brown curves show the magnetic asymmetry after excitation by a laser pump pulse at a pump-probe delay of +100 fs and +700 fs, respectively.

| Substrate/.../spacer/.../capping | Absorption ratios of the pump beam (%) | | |
|---|---|---|---|
| | Fe(bottom layer) | Spacer layer | Ni(top layer) |
| Fe(4 nm)/Ru(1.7 nm)/Ni(5 nm) | 15.9 | 11.7 | 19.3 |
| Fe(4 nm)/Ta(2 nm)/Ni(5 nm) | 19 | 3.2 | 23.5 |
| Fe(4 nm)/W(2 nm)/Ni(5 nm) | 18.9 | 5.4 | 23.1 |
| Fe(4 nm)/$Si_3N_4$(3 nm)/Ni(5 nm) | 21.5 | 0 | 26.4 |
| | Ni(bottom layer) | Spacer layer | Fe(top layer) |
| Ni(5 nm)/Ru(1.7 nm)/Fe(4 nm) | 18.5 | 12 | 17.1 |

Table 7.1: Calculated absorption ratios of the pump beam by each layer in terms of the percentage of the incident pump beam as calculated according to [59].

and $5 \pm 1\%$ for 2 nm Ta and W, respectively, and $23 \pm 1\%$ for 3 nm $Si_3N_4$. Note that the large Fe demagnetization in the case of a $Si_3N_4$ spacer is not strictly the result of obstructed spin-current flow between Ni and Fe; spin-flip demagnetization of Fe is larger because $Si_3N_4$ is more transparent. Indeed, optical matrix calculations show that the absorbance of the Fe layer is 15 % larger for the $Si_3N_4$ spacer (Table 7.1).

Comparison of the data for samples with different spacer layer materials indicates that interlayer spin-current propagation is not the only operative mechanism for ultrafast demagnetization. By using materials with a short spin lifetime as the spacer, spin transport between Ni and Fe should be reduced or even eliminated; however, we find that both the Ni and the Fe layers still demagnetize. I emphasize that our technique is sensitive to the average magnetization within a given layer, not the gradient of the spin accumulation that might result from intralayer spin-currents, in contrast to what was suggested in Ref. [5] in regard to T-MOKE experiments with optically thick magnetic layers. Given that I observe demagnetization in both the top Ni layer and buried Fe layer, I confirm that spin-flip scattering must necessarily contribute to the dynamics. This is in contrast to recent theoretical and experimental works on superdiffusive spin currents, [6, 5, 26], which claim spin transport as the only relevant process, and are not in accordance with two decades of experimental and theoretical work on spin-flip scattering in femtomagnetism. Note that although spin-transport and spin-flip scattering represent two very different microscopic interactions, their induced magnetization dynamics clearly evolve on identical timescales (Figure 7.2). This is why it was so challenging until now to disentangle their contributions using other measurement techniques.

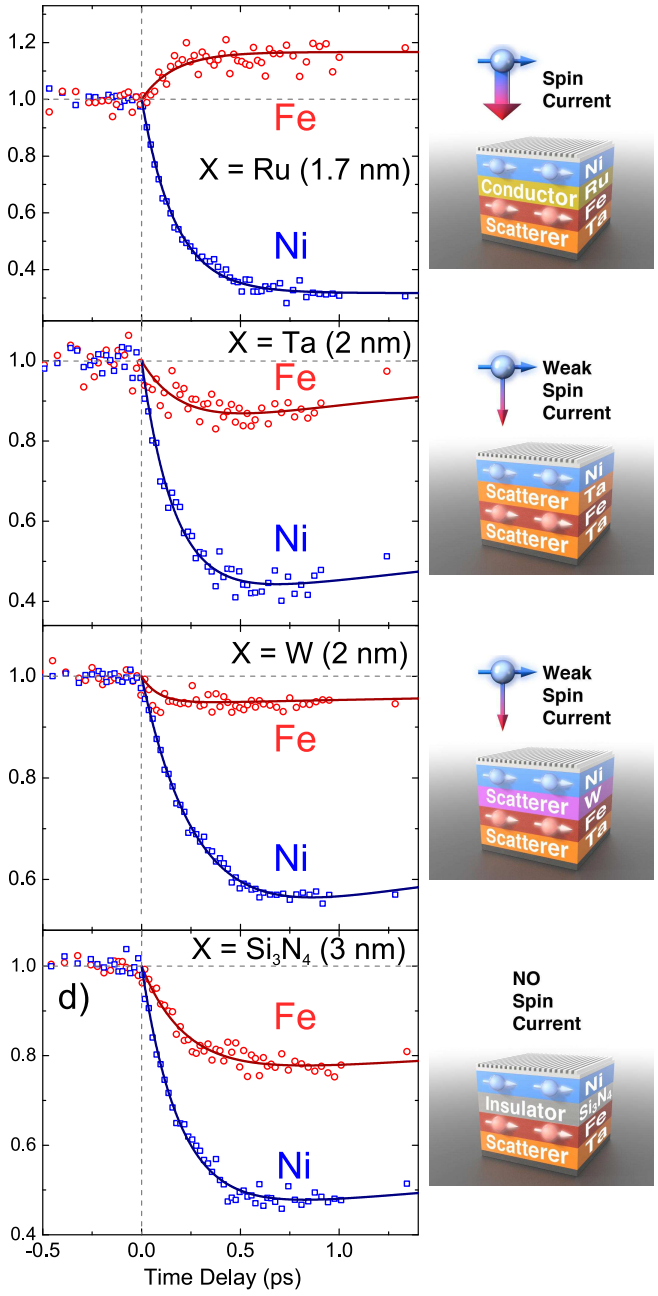


Figure 7.2: Layer-selective magnetization dynamics in substrate/Ta(3 nm)/Fe(4 nm)/X/Ni(5 nm)/$Si_3N_4$(6 nm) multilayers with different spacer layers. In a), clear enhancement in the magnetization of the Fe layer is observed in the presence of good spin transport across the 1.7 nm Ru spacer layer. In b) and c), no enhancement of the magnetization of the Fe layer is observed when spin scattering spacer layers of Ta (2 nm) and W (2 nm) are used. In d), spin currents are fully suppressed by inserting a 3 nm insulating $Si_3N_4$ layer.

In all of the sample systems considered so far, there is a preferential flow of majority spins from Ni to Fe. This has been explained in terms of the large spin transport asymmetry of hot electrons for Ni in comparison to Fe [64]. If this were indeed the case, the inversion of Ni and Fe in the multilayer stack should still result in majority spin-current flow from Ni to Fe, given that the optical absorbance of the Ni and Fe layers is only weakly dependent on their order in the stack (Table 7.1). Thus, I would expect that the magnetization change in Fe would still show a strong dependence on the relative orientation of the magnetization in the two layers. Surprisingly however, when we repeated our measurements for a sample where Fe is on top (substrate/Ta(3 nm)/Ni(5 nm)/Ru(1.7 nm)/Fe(4 nm)/$Si_3N_4$(6 nm)) only the Ni layer shows any significant dependence of the demagnetization amplitude on the relative orientation, as shown in Figure 7.3. The demagnetization of Ni is $38 \pm 1\%$ and $56 \pm 4\%$ for parallel and antiparallel alignments, respectively, while the magnetization of Fe is only slightly affected by the relative orientation. We infer from the data that the Fe majority spins are now flowing from Fe to Ni, in spite of the fact that the optical absorbance of the two ultrathin layers is virtually unchanged. One plausible explanation for the apparent inversion of spin-current flow direction is that the Ta seed layer acts as a strong spin scatterer, substantially reducing the majority spin-current emitted by the buried layer, whether it be Ni or Fe. The spin current from the top layer will be stronger in the downward direction into the multilayer due to the presence of the surface, while the spin current from the bottom layer upwards will be weaker due to scattering of downward-propagating spin current in the Ta seed layer. Another possible explanation might be related to calorimetric processes, induced by the gradient of the laser light absorption within the layers.

The data of Figure 7.3 are consistent with a simultaneous occurrence of interlayer spin-current flow and spin-flip demagnetization processes. It is generally known that the optically driven demagnetization of a single Fe layer is weaker than that of Ni under identical pump fluence. I also know that the buried Fe layer absorbs marginally less light than when it is on the top of the stack. In that case, the magnetization change of the buried Fe layer is primarily driven by interlayer spin-current transport, and only secondarily by intrinsic spin-flip processes. On the other hand,

when Fe is on top, the Fe-majority spin-current now flows into the Ni as explained above, but since spin-flip demagnetization processes are much stronger in Ni, the amount of demagnetization in Ni for parallel orientation is reduced. The effect of ultrafast spin-currents from the Fe into the Ni is not sufficient to induce an overall magnetization enhancement, in contrast to the case when Ni is on the top.

Finally, quantitative accounting of the magnetization change in the Ni and Fe layers can be used to show that both spin-flip processes and intralayer spin-currents are simultaneously present. Taking the atomic magnetic moments ($0.65\mu_B$ for Ni and $2.2\mu_B$ for Fe) and atomic concentrations ($9.14 \times 10^{28}\ m^{-3}$ for Ni and $8.50 \times 10^{28}\ m^{-3}$ for Fe) into account [78], a lossless transfer of spin between Fe and Ni should result in an approximately $3\times$ larger change in the magnetization of Ni compared to Fe. Thus, a 48 % reduction of the Ni magnetization is required to enhance the Fe magnetization by $16 \pm 1\%$, as observed in Figure 7.2a, under the assumption that the spin-current consists primarily of Ni majority spins, and that the magnetization change in Fe is primarily due to interlayer spin-currents (as seen before in the previous chapter). However, the Ni demagnetization in Figure 7.2a is $68 \pm 1\%$, suggestive that spin-flip processes account for roughly a third of the Ni demagnetization when Ni is the top layer. Similarly, the observed Ni demagnetization in Figure 7.3 of $38 \pm 1\%$ and $56 \pm 1\%$ for parallel and antiparallel alignment, respectively, requires a minimum demagnetization of 3 % for Fe. Again, this is approximately half as large as the Fe demagnetization shown in Figure 7.3, consistent with a hypothesis that half of the Fe demagnetization is the result of intrinsic spin-flip processes. Note that hot spin-polarized electrons that are lost due to ultrafast spin transport into another layer will influence the hot-electron spin-flip scattering rate inside the original layer. It is therefore not straightforward to compare demagnetization amplitudes between the different material systems. First, a theoretical picture including both processes needs to be developed.

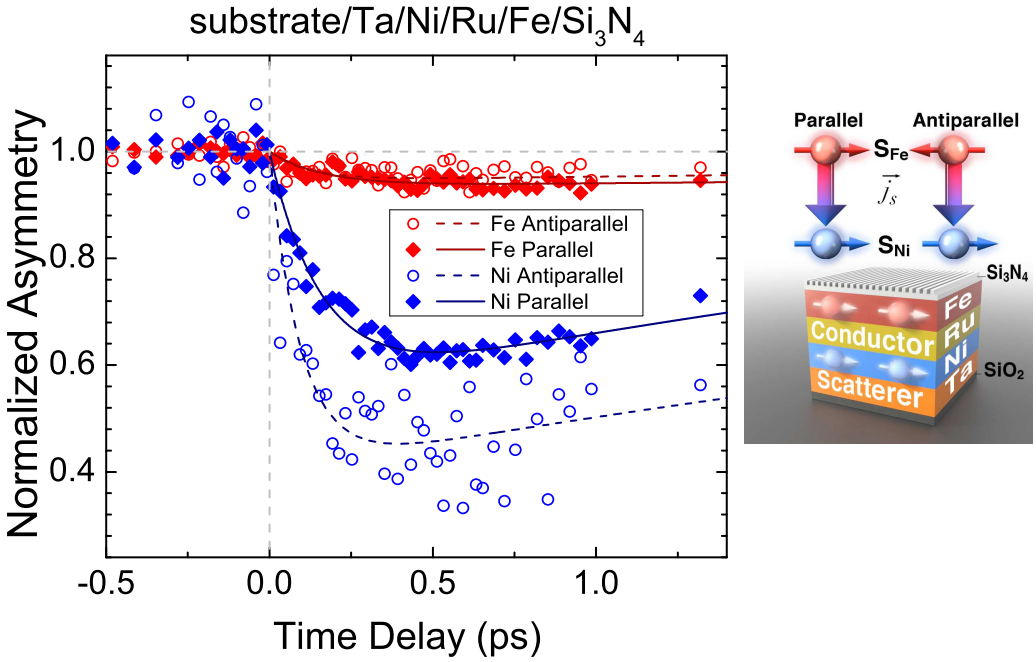


Figure 7.3: Magnetization dynamics of a substrate/Ta(3 nm)/Ni(5 nm)/Ru(1.7 nm)/Fe(4 nm)/$Si_3N_4$(6 nm) multilayer. Parallel and antiparallel alignments of the Ni and Fe layers are respectively obtained by using a strong (±40 mT) and weak (±10 mT) external magnetic field. The observed demagnetization in the Fe layer does not change as a function of the relative magnetic orientation. In contrast, demagnetization in the Ni layer increases from $\approx 38 \pm 1\%$ to $56 \pm 4\%$ for antiparallel orientation, because spin currents from the top (Fe) layer to the bottom (Ni) layer favor spin-flip scattering processes.

## 7.4 Conclusion

In summary, I show that both interlayer spin-currents and intrinsic spin-flip processes play an important role in optically driven ultrafast magnetization dynamics for the case of magnetic multilayers, depending critically on the composition of the investigated system. Both phenomena are comparable in magnitude for the samples studied here, and thus, a complete theory for ultrafast magnetization dynamics should include both mechanisms. Moreover, their respective strengths can be controlled by changing the design of the sample, which can also influence the directional flow of spin current.

# Chapter 8

# Outlook: Magnetic Imaging and Circularly Polarized Harmonics

## 8.1 Introduction

In this chapter, I give very recent exciting developments and results on ultrafast magnetization probing with high-harmonic generation (HHG). First, we demonstrate magnetic small-angle scattering patterns from FeGd samples, which is a great step in magnetic imaging. Second, we are able to generate circularly polarized harmonics and demonstrate x-ray magnetic circular dichroism (XMCD) for the first time on a tabletop. These two advancing promise that HHG from a tabletop source not only provides perfect temporal resolution, but also allows to image nanometer resolutions and study topologically modified-condensed matter systems by using circularly polarized light.

## 8.2 Magnetic Imaging

In the previous chapter, I explain how HHG allows to have element specificity and ultrafast time resolution on a tabletop, which is great advantages for probing ultrafast demagnetization. In addition to these two advantages, we also take advantage of high spatial resolution imaging with high harmonics. This is resulting from the short wavelengths of EUV photons. Future technological advances also require shrinking magnetic domains and transistor in addition to increasing their speed.

Previously, the coherent diffraction imaging has been heavily studied by Kapteyn-Murnane research group. A diffraction method needs to be used to image nano-objects, because there is no proper lens for the EUV region of the spectrum. In our imaging experiments specially fabricated

multilayer mirrors are used to focus EUV photons on a sample, and the diffraction pattern scattered by the sample is collected by a large-CCD camera. Since the CCD camera records only intensity of the diffracted photons, the phase information is lost. Then, special iterative algorithms are used to retrieve the lost-phase information of the diffraction pattern by a computer [51, 92, 73, 67, 68, 66]. Last record in the resolution at transmission geometry obtained by our tabletop high-harmonic source is 22 nm [73]. Very recently, it is also now possible reflection mode imaging of a nano-objects with remarkable height sensitivity[72].

Another important method used in our group is Fourier transform holography (FTH). Instead of iterative algorithms, a reference hole next to nano-object is used to create the hologram of the object on the camera. Then, one can use anti-correlation function to reconstruct the image of the sample. This technique is more straightforward in terms of experimental procedure and data analysis. However, the resolution of the extracted image is limited by the size of the reference hole. I show the benchmark study of FTH on a magnetic-domain images in Figure 8.1 taken from [24].

One important requirement of the coherent diffraction imaging is high photon flux. The diffraction is based on scattering of a photon from a magnetic impurity which has very small scattering rate. This makes magnetic imaging challenging on a tabletop because of lower photon fluxes with respect to a synchrotron or x-ray free electron laser.

The first step through magnetic imaging is small angle scattering experiments of magnetic samples. When one shines x-ray photons that resonance with magnetic sample, scattering rings from magnetic domain walls can be observed on a CCD camera. It is not possible to reconstruct the image of domains, but dynamics in domains and domain walls can be extracted by carefully analyzing scattering rings [58, 86]. Here we demonstrated small angle scattering from FeGd magnetic multilayers from HHG table top source as well as synchrotron radiation. I show these results in Figure 8.2. At the right, we use 713 eV soft x-ray photons from DESY synchrotron facility and record scattered x-ray photons. We can see the first and the third order rings with only 1s exposure time. At the left image, we use output of HHG at 55.5 eV after a monochrometer. We can see only the first order ring after 20 minute exposure time.

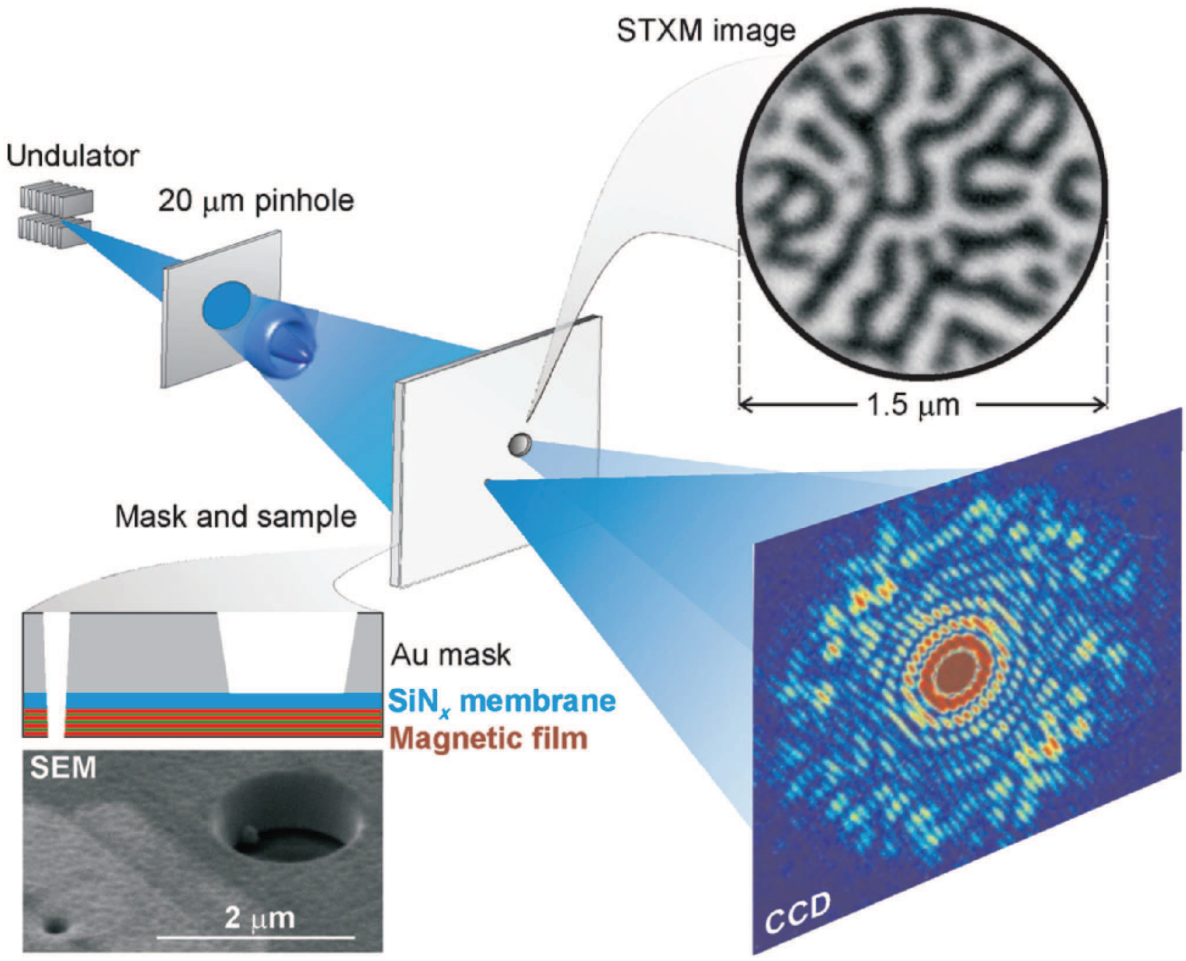


Figure 8.1: One of the earliest example of Fourier transform holography imaging of magnetic domains, taken from [24].

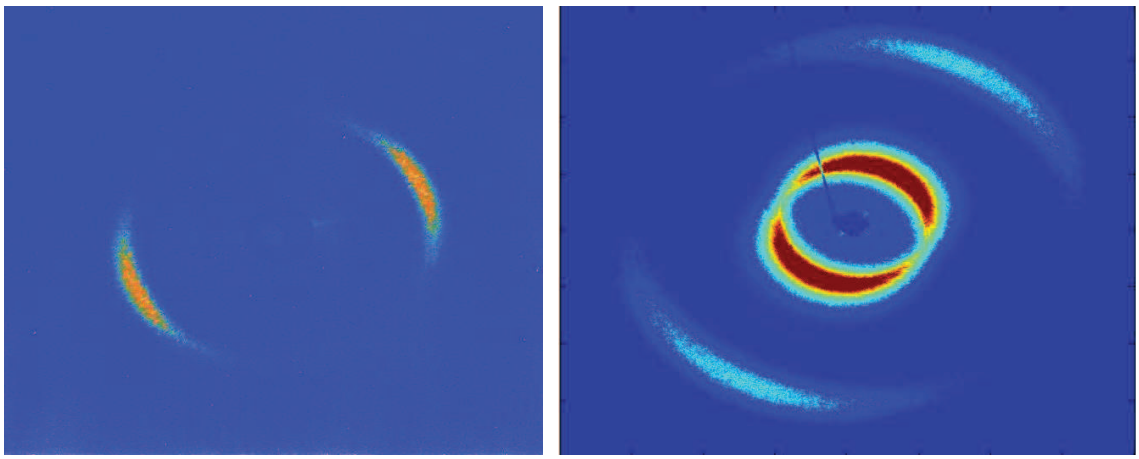


Figure 8.2: Small angle scattering results of FeGd magnetic multilayers from HHG and a synchrotron source. The left image is recorded by our in-home HHG source with a monochrometer for 55.5 eV at M edge of Fe. The right image is obtained by DESY synchrotron facility at 713 eV L edge of Fe. While we have only the first order at the left, we are able to see the first and the third order rings because of high photon flux, although the exposure time is 1200 times less.

Currently, we are working to improve the quality of images and implement new ptychography technique which uses many combined diffracted images to improve reconstruction resolution and image larger areas. Although, the magnetic imaging is promising to understand spatial dynamics in magnetic systems, high demands in laser specifications in magnetic imaging experiment make us to purse more ultrafast demagnetization studies with T-MOKE geometry.

## 8.3 Bright Circularly Polarized Harmonics

Maybe more exciting than magnetic imaging, we recently demonstrate generation of bright circularly polarized harmonics and XMCD on a tabletop. There have been many efforts to generate

circularly polarized high harmonics on a tabletop by quarter waveplates and other techniques, however these techniques result in very low photon flux and make impossible to use in any application. The technique we implemented was discussed in 1995, nonetheless because of the lack of optical and laser techniques it was not paid attention. Very recently, Fleischer et al. from the Technion University study this technique and accomplish to generate circularly polarized harmonics [29]. The idea behind the technique is simple but also very remarkable. Fleischer et al. combine two color ultrashort laser pulse with opposite hellicities and resulting electric field has flower-leaf like profile which allows to electron to recombine its parent atom, Figure 8.3. Since the recombination process also rotates by the laser frequency, the resulting x-ray field gains angular momentum and circularity. Here, we generate the second harmonics of fundamental output of Ti:Sp and combine these two colors after rotating the polarization to the left and right circularity, respectively. Then, the combined laser pulse is focused in a gas-filled fiber where circularly polarized harmonics are generated. Because the recombination occurs three times in a cycle, every third harmonics (3n) are suppressed because of three-fold symmetry. The 3n+1 harmonics follow the hellicity of the red, and the 3n-1 harmonics follow the hellicity of the blue light [29, 35].

First experiment we perform with the circularly polarized harmonics is XMCD, which is a dependence of absorption of x-ray photons by a magnetic sample on the hellicity of the incoming x-ray photon with respect to the magnetization direction. As we flip the magnetization of a Ni foil 'up' to 'down', the transmitted intensity of x-ray photons changes. The raw spectrum of circularly polarized harmonics and this change in XMCD are recorded by our CCD camera after a spectrometer, shown in Figure 8.4. Top, I show the raw spectrum of circularly polarized harmonics for generated in different gas medium. EUV harmonics cover the entire absorption edges of Fe, Co and Ni, when He is used. Because of three-fold symmetry, we see suppression of $3n$ harmonics, and different intensities of 3n+1 and 3n-1 harmonics. This difference results from different phase matching of these harmonics because the circularly polarized driven field creates different phase matching condition. At the bottom the Figure 8.4, I show transmitted intensities after a 50-nm-thick Ni foil upon the flipping the magnetization and normalized difference of these intensities

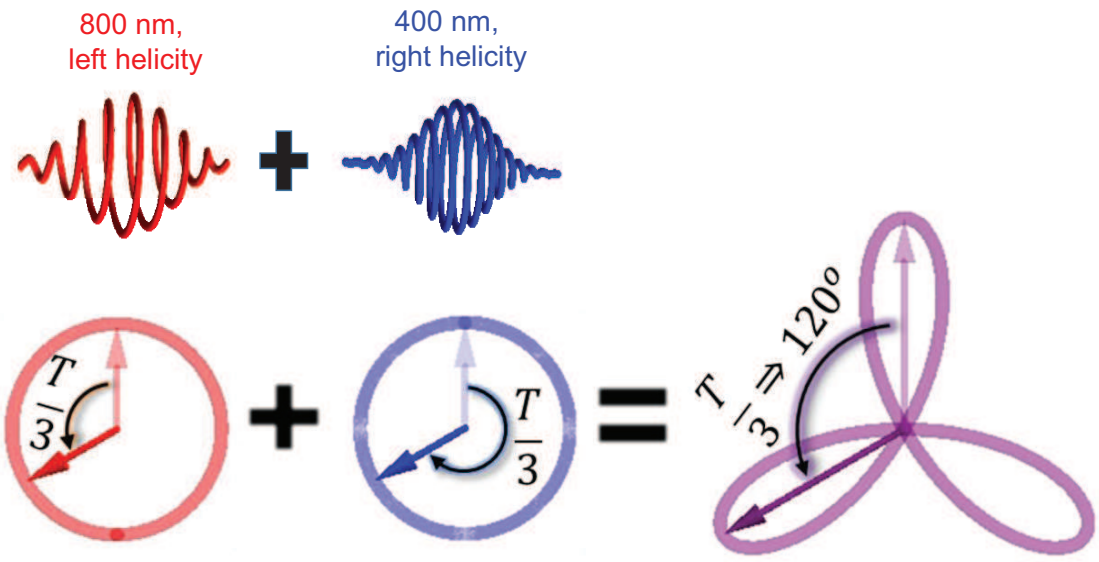


Figure 8.3: Sketch of circularly polarized harmonic generation. We combine 800 nm and 400 nm of wavelength ultrashort laser pulses with opposite hellicities. The resulting electric field looks like a flower-leaf. This electric field profile is very efficient for recombination process during HHG.

known as magnetic asymmetry, which was discussed in Chapter 2. The blue and red curves show the peaks of harmonics after the flipping the external magnetic field. The magnetic asymmetry is also shown by the black curve in the lower graph. Because the adjacent harmonics have opposite hellicities and 3n harmonics are suppressed, the magnetic asymmetry has a '0', '+', '–' sequence profile that corresponds 3n, 3n+1 and 3n+2(3n-1) harmonics, respectively.

Our data proves that a broad spectrum of bright circularly-polarized harmonics are generated, and consecutive harmonics exhibit opposite helicity. High transmission output after 50-nm-thick Ni shows that phase matching consideration are robust and efficiency as high as in T-MOKE geometry. This study removes a major drawback to date - that the polarization of bright high harmonics sources is limited to linear polarization - and thus breaks ground for ultrafast circular dichroic

studies of chiral molecules and nanostructures, and magnetism. This advancing also enables the exploration of coupled spin, charge and structural dynamics in magnetic domains with good spatial and temporal resolution. We also propose that tabletop circularly polarized harmonics for seeding x-ray free electron lasers to enhance the efficiency and reduce the complexity [55].

## 8.4 Conclusion

Since these two continuing projects are under development and have not been optimized or not studied carefully yet, I briefly mention and leave them for next studies. Nevertheless, the magnetic imaging is very important to understand spatial formations and dynamics in magnetic systems, which is crucial for technical applications. More importantly, the circularly polarized harmonics is very remarkable development in our experiment because this allows us to study different correlated systems such as topological insulators and high-Tc superconductors by making use of time-reversal symmetry property of the circularly polarized x-rays.

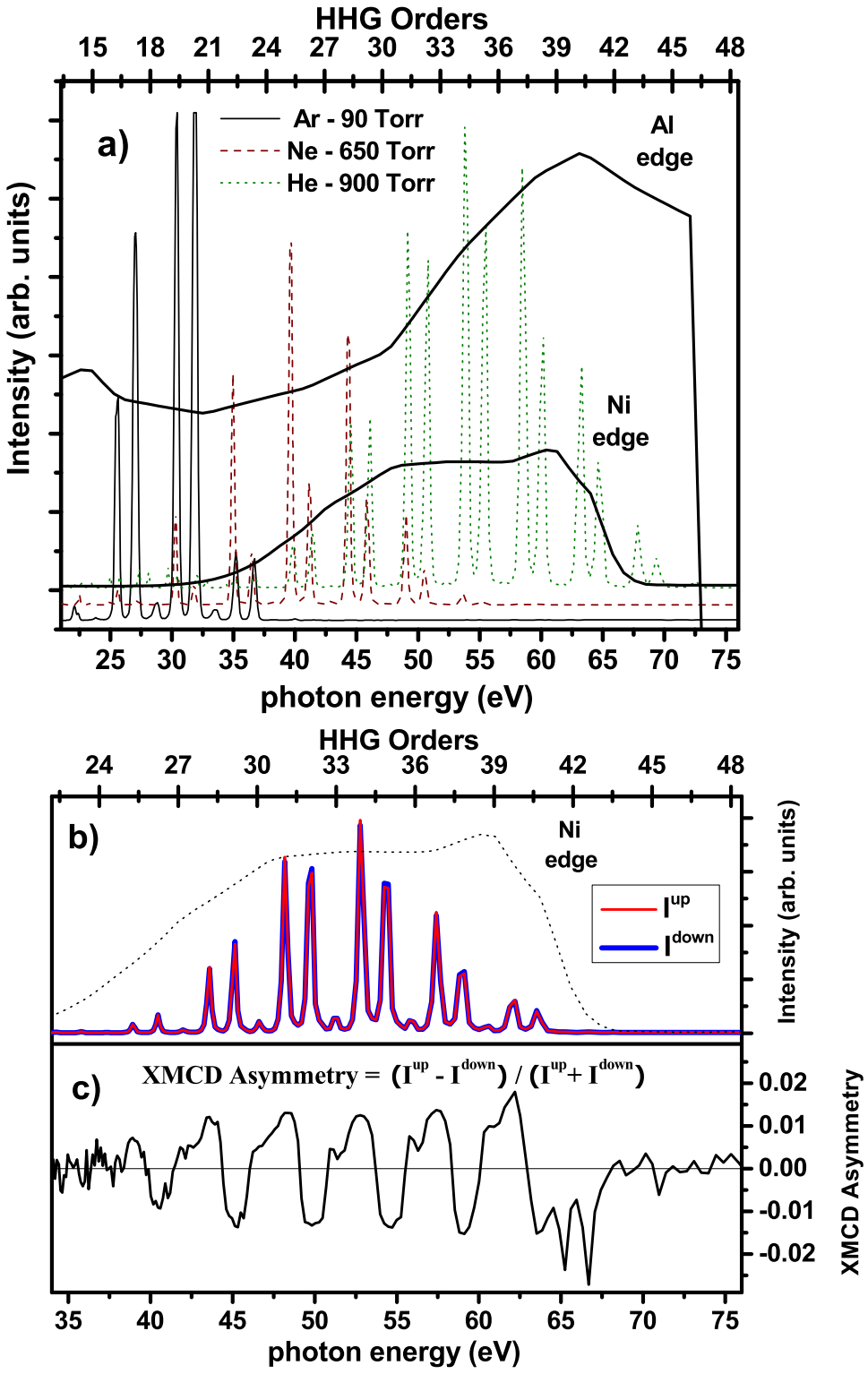


Figure 8.4: The raw spectrum of circularly polarized harmonics and transmitted intensities of high harmonics after a 50-nm-thick Ni foil. (top) Generated circularly polarized high-harmonics from Ar, Ne and He gases. We can cover the entire absorption edges of Fe, Co and Ni to study XMCD. (bottom) The magnetization of the foil is flipped from the up to the down in order to create a magnetic dichroic signal shown by the red and blue curves. The normalized difference of these intensities are plotted at the lower graph. The $3n$ harmonics are suppressed and the adjacent harmonics are oppositely polarized as explained in the text. Hence, the magnetic asymmetry has a sequence of '0', '+', '–'.

# Chapter 9

# Conclusion

In this thesis, I report on the experimental study of ultrafast magnetization dynamics on magnetic multilayers using element-selective ultrafast extreme-ultraviolet light on a tabletop. I present background information about our experimental techniques and three important findings with two additional continuing work. In the previous chapters,

- I discuss the magneto-optical response in different magnetic systems and at different geometries in Chapter 2. I extend the theoretical treatment into magnetic multilayers successfully.

- I explain our experimental setup that is unique today, to our best knowledge, to probe magnetization dynamics element selectively with few-femtosecond temporal resolution. The crucial feature in our setup is high-harmonic generation which produces ultra-broadband extreme-ultraviolet photons to probe different elements in an alloy or a multilayer simultaneously and separately that is not possible with another source. I also theoretically discuss how a pump beam excites our magnetic multilayer samples. Then, I introduce other equipment including the CCD camera, the toroidal mirror, the iron-yoke magnet, and grating samples that work as spectrometer.

- I review previous investigations on non-magnetic artifacts in magneto-optical response in ultrafast dynamics originating from other electronic dynamics. I also question our experimental technique for any existence of non-magnetic artifact. I experimentally challenge this question and find out that transverse magneto-optical Kerr effect via extreme-ultraviolet

light is a perfect technique for ultrafast magnetization probing without any artifact in magneto-optical response.

- I present experimental and theoretical studies on ultrafast magnetization dynamics in Ni/Ru/Fe magnetic multilayers. Surprisingly, we observe the first ultrafast magnetization enhancement following an ultrafast laser-pulse excitation. This behavior is well explained by ultrafast superdiffusive spin-currents which results from different itinerant characteristics of spin-up and spin-down electrons in Ni and Fe layers. We conclude that ultrafast spin-currents are dominant in certain sample geometry.

- I follow-up the study on Ni/Fe multilayers by changing the spacer layer to an insulating or a spin-scatterer one, and we can fully control ultrafast spin-currents. With our systematic studies via engineering the sample systems, we show that ultrafast spin-currents and spin-flip scattering mechanisms both contribute during ultrafast demagnetization and future theories must include both.

- I finally show two very promising continuing work under development. First one is coherent resonant-magnetic scattering imaging with extreme-ultraviolet light to understand nanoscale magnetism. Second one is x-ray magnetic circular dichroism on a tabletop that is only possible by generating circularly polarized high-harmonics. These two ongoing studies will make possible cutting-edge experimental findings and solve puzzles about magnetism as well as ultrafast magnetism via high-harmonic generation light sources.

## Bibliography


[1] U. Atxitia and O. Chubykalo-Fesenko. Evidence for thermal mechanisms in laser-induced femtosecond spin dynamics. Physical Review B, 81(17):174401, May 2010.

[2] U. Atxitia and O. Chubykalo-Fesenko. Ultrafast magnetization dynamics rates within the Landau-Lifshitz-Bloch model. Physical Review B, 84(14):144414, October 2011.

[3] Jack Bass and William P Pratt. Spin-diffusion lengths in metals and alloys, and spin-flipping at metal/metal interfaces: an experimentalists critical review. Journal of Physics: Condensed Matter, 19(18):183201, May 2007.

[4] F Batallan, I Rosenman, and CB Sommers. Band structure and Fermi surface of hcp ferromagnetic cobalt. Physical Review B, 11(1), 1975.

[5] M. Battiato, G. Barbalinardo, K. Carva, and P. M. Oppeneer. Beyond linear response theory for intensive light-matter interactions: Order formalism and ultrafast transient dynamics. Physical Review B, 85(4):1–16, January 2012.

[6] M. Battiato, K. Carva, and P. Oppeneer. Superdiffusive Spin Transport as a Mechanism of Ultrafast Demagnetization. Physical Review Letters, 105(2):027203, July 2010.

[7] M. Battiato, K. Carva, and P. Oppeneer. Theory of laser-induced ultrafast superdiffusive spin transport in layered heterostructures. Physical Review B, 86(2):024404, July 2012.

[8] Marco Battiato. Superdiffusive Spin Transport and Ultrafast Magnetization Dynamics. PhD thesis, 2013.

[9] E Beaurepaire, J Merle, a Daunois, and J Bigot. Ultrafast spin dynamics in ferromagnetic nickel. Physical review letters, 76(22):4250–4253, May 1996.

[10] Hernert S Bennett and Edward A Stern. Faraday Effect in Solids. Physical Review, 137(2):A 448, 1965.

[11] Jean-Yves Bigot, Mircea Vomir, and Eric Beaurepaire. Coherent ultrafast magnetism induced by femtosecond laser pulses. Nature Physics, 5(7):515–520, May 2009.

[12] VW Biricik. Transverse Kerr magnetooptic response of a multilayer stack containing magnetic layers. Applied optics, 28(8):1501–1503, 1989.

[13] C Brombacher, M Grobis, J Lee, J Fidler, T Eriksson, T Werner, O Hellwig, and M Albrecht. L1 FePtCu bit patterned media. Nanotechnology, 23(2):025301, January 2012.

[14] C. Bunce, J. Wu, G. Ju, B. Lu, D. Hinzke, N. Kazantseva, U. Nowak, and R. W. Chantrell. Laser-induced magnetization switching in films with perpendicular anisotropy: A comparison between measurements and a multi-macrospin model. Physical Review B, 81(17):174428, May 2010.

[15] E. Carpene, E. Mancini, C. Dallera, M. Brenna, E. Puppin, and S. De Silvestri. Dynamics of electron-magnon interaction and ultrafast demagnetization in thin iron films. Physical Review B, 78(17):174422, November 2008.

[16] K. Carva, M. Battiato, D. Legut, and P. M. Oppeneer. Ab initio theory of electron-phonon mediated ultrafast spin relaxation of laser-excited hot electrons in transition-metal ferromagnets. Physical Review B, 87(18):184425, May 2013.

[17] K. Carva, M. Battiato, and P. Oppeneer. Ab Initio Investigation of the Elliott-Yafet Electron-Phonon Mechanism in Laser-Induced Ultrafast Demagnetization. Physical Review Letters, 107(20):1–5, November 2011.

[18] Karel Carva, Marco Battiato, and Peter M. Oppeneer. Is the controversy over femtosecond magneto-optics really solved? Nature Physics, 7(9):665–665, September 2011.

[19] Zenghu Chang, Andy Rundquist, Haiwen Wang, M.M. Murnane, and H.C. Kapteyn. Generation of coherent soft X rays at 2.7 nm using high harmonics. Physical Review Letters, 79(16):2967–2970, October 1997.

[20] M.-C. Chen, P. Arpin, T. Popmintchev, M. Gerrity, B. Zhang, M. Seaberg, D. Popmintchev, M. M. Murnane, and H. C. Kapteyn. Bright, Coherent, Ultrafast Soft X-Ray Harmonics Spanning the Water Window from a Tabletop Light Source. Physical Review Letters, 105(17):173901, October 2010.

[21] M. Cinchetti, M. Sánchez Albaneda, D. Hoffmann, T. Roth, J.-P. Wüstenberg, M. Krauß, O. Andreyev, H. C. Schneider, M. Bauer, and M. Aeschlimann. Spin-Flip Processes and Ultrafast Magnetization Dynamics in Co: Unifying the Microscopic and Macroscopic View of Femtosecond Magnetism. Physical Review Letters, 97(17):177201, October 2006.

[22] F. Dalla Longa. Laser-induced magnetization dynamics. PhD thesis, 2008.

[23] K. Eid, R. Fonck, M. AlHaj Darwish, W. P. Pratt, and J. Bass. Current-perpendicular-to-plane-magnetoresistance properties of Ru and Co/Ru interfaces. Journal of Applied Physics, 91(10):8102, 2002.

[24] S Eisebitt, J Lüning, WF Schlotter, and M Lörgen. Lensless imaging of magnetic nanostructures by X-ray spectro-holography. Nature, 432(December):885–888, 2004.

[25] JL Erskine and EA Stern. Calculation of the m2,3 magneto-optical absorption spectrum of ferromagnetic nickel. Physical Review B, 12:5016–5024, 1975.

[26] A Eschenlohr, M Battiato, P Maldonado, N Pontius, T Kachel, K Holldack, R Mitzner, A Föhlisch, P M Oppeneer, and C Stamm. Ultrafast spin transport as key to femtosecond demagnetization. Nature Materials, 12(2):1–5, January 2013.

[27] Sven Essert and Hans Christian Schneider. Electron-phonon scattering dynamics in ferromagnets on ultrafast timescales: Influence of the phonon temperature. Journal of Applied Physics, 111(7):07C514, 2012.

[28] WS Fann, R Storz, HWK Tom, and J Bokor. Direct measurement of nonequilibrium electron-energy distributions in subpicosecond laser-heated gold films. Physical review letters, 68(18):2834–2837, 1992.

[29] Avner Fleischer, Ofer Kfir, Tzvi Diskin, Pavel Sidorenko, and Oren Cohen. Does high harmonic generation conserve angular momentum? http://arxiv.org/abs/1310.1206.

[30] D. a. Garanin. Fokker-Planck and Landau-Lifshitz-Bloch equations for classical ferromagnets. Physical Review B, 55(5):3050–3057, February 1997.

[31] Mathias Getzlaff. Fundamentals of magnetism. 2008.

[32] BL Henke, EM Gullikson, and JC Davis. Atomic data and nuclear data tables. 1993.

[33] Hartmut Hochst, Dennis Rioux, Dai Zhao, and David L. Huber. Magnetic linear dichroism effects in reflection spectroscopy: A case study at the Fe M2,3 edge. Journal of Applied Physics, 81(11):7584, 1997.

[34] T. Kampfrath, R. Ulbrich, F. Leuenberger, M. Münzenberg, B. Sass, and W. Felsch. Ultrafast magneto-optical response of iron thin films. Physical Review B, 65(10):104429, February 2002.

[35] Ofer Kfir, Patrik Grychtol, Emrah Turgut, and Ronny Knut. Generation of bright circularly-polarized extreme ultraviolet high harmonics for magnetic circular dichroism spectroscopy. arxiv.org/abs/1401.4101, pages 1–12, 2014.

[36] Andrei Kirilyuk, Alexey Kimel, and Theo Rasing. Ultrafast optical manipulation of magnetic order. Reviews of Modern Physics, 82(3):2731–2784, September 2010.

[37] B. Koopmans, H.H.J.E. Kicken, M. van Kampen, and W.J.M. de Jonge. Microscopic model for femtosecond magnetization dynamics. Journal of Magnetism and Magnetic Materials, 286:271–275, February 2005.

[38] B Koopmans, van Kampen M, Jt Kohlhepp, and de Jonge WJ. Ultrafast magneto-optics in nickel: magnetism or optics? Physical review letters, 85(4):844–7, July 2000.

[39] B Koopmans, G Malinowski, F. Dalla Longa, D Steiauf, M. Fahnle, T Roth, M Cinchetti, and M Aeschlimann. Explaining the paradoxical diversity of ultrafast laser-induced demagnetization. Nature Materials, 9(3):259–265, 2010.

[40] B. Koopmans, J. Ruigrok, F. Longa, and W. de Jonge. Unifying Ultrafast Magnetization Dynamics. Physical Review Letters, 95(26):1–4, December 2005.

[41] B Koopmans, M. van Kampen, and W.J.M. de Jonge. Experimental access to femtosecond spin dynamics. Journal of Physics: Condensed Matter, 15:S723–S736, 2003.

[42] JB Kortright and SK Kim. Resonant magneto-optical properties of Fe near its 2p levels: Measurement and applications. Physical Review B, 62(18):216–228, 2000.

[43] Michael Krauß, Tobias Roth, Sabine Alebrand, Daniel Steil, Mirko Cinchetti, Martin Aeschlimann, and Hans Schneider. Ultrafast demagnetization of ferromagnetic transition metals: The role of the Coulomb interaction. Physical Review B, 80(18):1–4, November 2009.

[44] MH Kryder and EC Gage. Heat assisted magnetic recording. Proceedings of the IEEE, 96(11), 2008.

[45] Chan La-o vorakiat. Element-Selective Ultrafast Magnetization Dynamics with a Tabletop Light Source. PhD thesis, 2011.

[46] Chan La-O-Vorakiat, Mark Siemens, Margaret M. Murnane, Henry C. Kapteyn, Stefan Mathias, Martin Aeschlimann, Patrik Grychtol, Roman Adam, Claus M. Schneider, Justin M. Shaw, Hans Nembach, and T. J. Silva. Ultrafast Demagnetization Dynamics at the M Edges of Magnetic Elements Observed Using a Tabletop High-Harmonic Soft X-Ray Source. Physical Review Letters, 103(25):257402, December 2009.

[47] Chan La-O-Vorakiat, Emrah Turgut, Carson Teale, Henry Kapteyn, Margaret Murnane, Stefan Mathias, Martin Aeschlimann, Claus Schneider, Justin Shaw, Hans Nembach, and T. Silva. Ultrafast Demagnetization Measurements Using Extreme Ultraviolet Light: Comparison of Electronic and Magnetic Contributions. Physical Review X, 2(1):011005, January 2012.

[48] G. Malinowski, F. Dalla Longa, J. H. H. Rietjens, P. V. Paluskar, R. Huijink, H. J. M. Swagten, and B. Koopmans. Control of speed and efficiency of ultrafast demagnetization by direct transfer of spin angular momentum. Nature Physics, 4(11):855–858, September 2008.

[49] Stefan Mathias, Chan La-O-Vorakiat, Patrik Grychtol, Patrik Granitzka, Emrah Turgut, Justin M. Shaw, Roman Adam, Hans Nembach, Mark Siemens, S Eich, Claus M. Schneider, T. J. Silva, Martin Aeschlimann, Margaret M. Murnane, and Henry C. Kapteyn. Probing the timescale of the exchange interaction in a ferromagnetic alloy. Proceedings of the National Academy of Sciences of the United States of America, 109(13):4792, 2012.

[50] Alexey Melnikov, Ilya Razdolski, Tim Wehling, Evangelos Papaioannou, Vladimir Roddatis, Paul Fumagalli, Oleg Aktsipetrov, Alexander Lichtenstein, and Uwe Bovensiepen. Ultrafast Transport of Laser-Excited Spin-Polarized Carriers in Au/Fe/MgO(001). Physical Review Letters, 107(7):076601, August 2011.

[51] Jianwei Miao, Pambos Charalambous, Janos Kirz, and David Sayre. Extending the methodology of X-ray crystallography to allow imaging of micrometre-sized non-crystalline specimens. Nature, 400(July):342–344, 1999.

[52] M. Morota, Y. Niimi, K. Ohnishi, D. Wei, T. Tanaka, H. Kontani, T. Kimura, and Y. Otani. Indication of intrinsic spin Hall effect in 4d and 5d transition metals. Physical Review B, 83(17):174405, May 2011.

[53] B Y Mueller, T Roth, M Cinchetti, M Aeschlimann, and B Rethfeld. Driving force of ultrafast magnetization dynamics. New Journal of Physics, 13(12):123010, December 2011.

[54] E. B. Myers. Current-Induced Switching of Domains in Magnetic Multilayer Devices. Science, 285(5429):867–870, August 1999.

[55] E Oliva, M Fajardo, L Li, M Pittman, and TTT et al. Le. A proposal for multi-tens of GW fully coherent femtosecond soft X-ray lasers. Nature ..., 6(October):764–767, 2012.

[56] P.M. Oppeneer. Magneto-optical Kerr spectra. In K. H. J. Buschow, editor, Handbook of Magnetic Materials, pages 229–422. Elsevier Amsterdam, 2011, 2001.

[57] SSP Parkin and D Mauri. Spin engineering: Direct determination of the Ruderman-Kittel-Kasuya-Yosida far-field range function in ruthenium. Physical Review B, 44(13):7131–7134, 1991.

[58] B. Pfau, S. Schaffert, L. Müller, C. Gutt, a. Al-Shemmary, F. Büttner, R. Delaunay, S. Düsterer, S. Flewett, R. Frömter, J. Geilhufe, E. Guehrs, C.M. Günther, R. Hawaldar, M. Hille, N. Jaouen, a. Kobs, K. Li, J. Mohanty, H. Redlin, W.F. Schlotter, D. Stickler, R. Treusch, B. Vodungbo, M. Kläui, H.P. Oepen, J. Lüning, G. Grübel, and S. Eisebitt. Ultrafast optical demagnetization manipulates nanoscale spin structure in domain walls. Nature Communications, 3:1100, October 2012.

[59] Pochi Yeh. Optical waves in layerd media. Wiley Interscience, New York, 2nd edition, 2005.

[60] T. Popmintchev, M.-C. Chen, D. Popmintchev, P. Arpin, S. Brown, S. Alisauskas, G. Andriukaitis, T. Balciunas, O. D. Mucke, A. Pugzlys, A. Baltuska, B. Shim, S. E. Schrauth, A. Gaeta, C. Hernandez-Garcia, L. Plaja, A. Becker, Jaron-Becker, M. M. Murnane, and H. C. Kapteyn. Bright Coherent Ultrahigh Harmonics in the keV X-ray Regime from Mid-Infrared Femtosecond Lasers. Science, 336(6086):1287–1291, June 2012.

[61] Tenio Popmintchev, Ming-Chang Chen, Paul Arpin, Margaret M. Murnane, and Henry C. Kapteyn. The attosecond nonlinear optics of bright coherent X-ray generation. Nature Photonics, 4(12):822–832, December 2010.

[62] I. Radu, K. Vahaplar, C. Stamm, T. Kachel, N. Pontius, H. a. Dürr, T. a. Ostler, J. Barker, R. F. L. Evans, R. W. Chantrell, a. Tsukamoto, a. Itoh, a. Kirilyuk, Th. Rasing, and a. V. Kimel. Transient ferromagnetic-like state mediating ultrafast reversal of antiferromagnetically coupled spins. Nature, pages 5–9, March 2011.

[63] H. Regensburger, R. Vollmer, and J. Kirschner. Time-resolved magnetization-induced second-harmonic generation from the Ni(110) surface. Physical Review B, 61(21):14716–14722, June 2000.

[64] Denis Rudolf. Femtosecond Spin Dynamics in Magnetic Multilayers Employing High Harmonics of Laser Rad PhD thesis, 2013.

[65] Dennis Rudolf, Chan La-O-Vorakiat, Marco Battiato, Roman Adam, Justin M. Shaw, Emrah Turgut, Pablo Maldonado, Stefan Mathias, Patrik Grychtol, Hans T. Nembach, Thomas J. Silva, Martin Aeschlimann, Henry C. Kapteyn, Margaret M. Murnane, Claus M. Schneider, and Peter M. Oppeneer. Ultrafast magnetization enhancement in metallic multilayers driven by superdiffusive spin current. Nature Communications, 3:1037, September 2012.

[66] R L Sandberg, D a Raymondson, C La-O-Vorakiat, a Paul, K S Raines, J Miao, M M Murnane, H C Kapteyn, and W F Schlotter. Tabletop soft-x-ray Fourier transform holography with 50 nm resolution. Optics letters, 34(11):1618–20, June 2009.

[67] Richard Sandberg, Ariel Paul, Daisy Raymondson, Steffen Hädrich, David Gaudiosi, Jim Holtsnider, Raanan Tobey, Oren Cohen, Margaret Murnane, Henry Kapteyn, Changyong Song, Jianwei Miao, Yanwei Liu, and Farhad Salmassi. Lensless Diffractive Imaging Using Tabletop

Coherent High-Harmonic Soft-X-Ray Beams. Physical Review Letters, 99(9):098103, August 2007.

[68] Richard L Sandberg, Changyong Song, Przemyslaw W Wachulak, Daisy a Raymondson, Ariel Paul, Bagrat Amirbekian, Edwin Lee, Anne E Sakdinawat, Chan La-O-Vorakiat, Mario C Marconi, Carmen S Menoni, Margaret M Murnane, Jorge J Rocca, Henry C Kapteyn, and Jianwei Miao. High numerical aperture tabletop soft x-ray diffraction microscopy with 70-nm resolution. Proceedings of the National Academy of Sciences of the United States of America, 105(1):24–7, January 2008.

[69] A. B. Schmidt, M. Pickel, M. Donath, P. Buczek, A. Ernst, V. Zhukov, P. Echenique, L. Sandratskii, E. Chulkov, and M. Weinelt. Ultrafast Magnon Generation in an Fe Film on Cu(100). Physical Review Letters, 105(19):197401, November 2010.

[70] A. Scholl, L. Baumgarten, R. Jacquemin, and W. Eberhardt. Ultrafast Spin Dynamics of Ferromagnetic Thin Films Observed by fs Spin-Resolved Two-Photon Photoemission. Physical Review Letters, 79(25):5146–5149, December 1997.

[71] M. Schroeder. Magnetooptic Kerr Effect in VUV for Iron. PhD thesis, 2000.

[72] M. D. Seaberg, Bosheng Zhang, Dennis F. Gardner, Elisabeth R. Shanblatt, Margaret M. Murnane, Henry C. Kapteyn, and Daniel E. Adams. Tabletop Nanometer Extreme Ultraviolet Imaging in an Extended Reflection Mode using Coherent Fresnel Ptychography. arXiv:1312.2049v1, pages 1–9, 2013.

[73] Matthew D. Seaberg, Daniel E. Adams, Ethan L. Townsend, Daisy A. Raymondson, William F. Schlotter, Yanwei Liu, Carmen S. Menoni, Lu Rong, Chien-Chun Chen, Jianwei Miao, Henry C. Kapteyn, and Margaret M. Murnane. Ultrahigh 22 nm resolution coherent diffractive imaging using a desktop 13 nm high harmonic source. Optics Express, 19(23):22470, October 2011.

[74] C. Spielmann. Generation of Coherent X-rays in the Water Window Using 5-Femtosecond Laser Pulses. Science, 278(5338):661–664, October 1997.

[75] C Stamm, T Kachel, N Pontius, R Mitzner, T Quast, K Holldack, S Khan, C Lupulescu, E F Aziz, M Wietstruk, H a Dürr, and W Eberhardt. Femtosecond modification of electron localization and transfer of angular momentum in nickel. Nature materials, 6(10):740–3, October 2007.

[76] C. Stanciu, F. Hansteen, a. Kimel, a. Kirilyuk, a. Tsukamoto, a. Itoh, and Th. Rasing. All-Optical Magnetic Recording with Circularly Polarized Light. Physical Review Letters, 99(4):1–4, July 2007.

[77] Claudiu Daniel Stanciu. Laser-Induced Femtosecond magnetic Recording. PhD thesis, Radboud University Nijmegen, 2008.

[78] J. Stöhr and H. C. Siegmann. Magnetism: From Fundamentals to Nanoscale Dynamics. Springer, 2006.

[79] Muhammad Sultan. Ultrafast Magnetization Dynamics of Lanthanide Metals and Alloys. PhD thesis, 2012.

[80] Muhammad Sultan, Unai Atxitia, Alexey Melnikov, Oksana Chubykalo-Fesenko, and Uwe Bovensiepen. Electron- and phonon-mediated ultrafast magnetization dynamics of Gd(0001). Physical Review B, 85(18):184407, May 2012.

[81] Muhammad Sultan, Alexey Melnikov, and Uwe Bovensiepen. Ultrafast magnetization dynamics of Gd(0001): Bulk versus surface. Physica Status Solidi (B), 248(10):2323–2329, October 2011.

[82] Emrah Turgut, Patrik Grychtol, Chan La-O-Vorakiat, Daniel E. Adams, Henry C. Kapteyn, Margaret M. Murnane, Stefan Mathias, Martin Aeschlimann, Claus M. Schneider, Justin M. Shaw, Hans T. Nembach, and Thomas J. Silva. Reply to Comment on Ultrafast Demagnetization Measurements Using Extreme Ultraviolet Light: Comparison of Electronic and Magnetic Contributions . Physical Review X, 3(3):038002, September 2013.

[83] Emrah Turgut, Chan La-o vorakiat, Justin M Shaw, Patrik Grychtol, Hans T Nembach, Dennis Rudolf, Roman Adam, Martin Aeschlimann, Claus M Schneider, Thomas J Silva, Margaret M Murnane, Henry C Kapteyn, and Stefan Mathias. Controlling the Competition between Optically Induced Ultrafast Spin-Flip Scattering and Spin Transport in Magnetic Multilayers. Physical Review Letters, 110(May):197201, 2013.

[84] S Valencia, a Gaupp, W Gudat, H-Ch Mertins, P M Oppeneer, D Abramsohn, and C M Schneider. Faraday rotation spectra at shallow core levels: 3 p edges of Fe, Co, and Ni. New Journal of Physics, 8(10):254–254, October 2006.

[85] A. Vaterlaus, D. Guarisco, M. Lutz, M. Aeschlimann, M. Stampanoni, and F. Meier. Different spin and lattice temperatures observed by spin-polarized photoemission with picosecond laser pulses. Journal of Applied Physics, 67(9):5661, 1990.

[86] Boris Vodungbo, Julien Gautier, Guillaume Lambert, Anna Barszczak Sardinha, Magali Lozano, Stéphane Sebban, Mathieu Ducousso, Willem Boutu, Kaigong Li, Bharati Tudu, Marina Tortarolo, Ranjit Hawaldar, Renaud Delaunay, Victor López-Flores, Jacek Arabski, Christine Boeglin, Hamed Merdji, Philippe Zeitoun, and Jan Lüning. Laser-induced ultrafast demagnetization in the presence of a nanoscale magnetic domain network. Nature Communications, 3:999, August 2012.

[87] Boris Vodungbo, Julien Gautier, Guillaume Lambert, Philippe Zeitoun, and Jan Lüning. Comment on Ultrafast Demagnetization Measurements Using Extreme Ultraviolet Light: Comparison of Electronic and Magnetic Contributions. Physical Review X, 3(3):038001, September 2013.

[88] Hélène Vonesch and Jean-Yves Bigot. Ultrafast spin-photon interaction investigated with coherent magneto-optics. Physical Review B, 85(18):180407, May 2012.

[89] J. Walowski, G. Müller, M. Djordjevic, M. Münzenberg, M. Kläui, C. Vaz, and J. Bland. Energy Equilibration Processes of Electrons, Magnons, and Phonons at the Femtosecond Time Scale. Physical Review Letters, 101(23):237401, December 2008.

[90] T Wang, D Zhu, B Wu, and C et al. Graves. Femtosecond single-shot imaging of nanoscale ferromagnetic order in Co/Pd multilayers using resonant x-ray holography. Physical Review Letters, 267403(June):1–6, 2012.

[91] Z. J. Yang and M. R. Scheinfein. Combined three-axis surface magneto-optical Kerr effects in the study of surface and ultrathin-film magnetism. Journal of Applied Physics, 74(11):6810, 1993.

[92] Bosheng Zhang, MD Seaberg, DE Adams, Dennis F Gardner, Elisabeth Shanblatt, Justin M. Shaw, Weilun Chao, Erik M Gullikson, Farhad Salmassi, Henry C. Kapteyn, and Margaret M. Murnane. Full field tabletop EUV coherent diffractive imaging in a transmission geometry. Optics Express, 21(19):839–843, 2013.

[93] G P Zhang and W Hübner. Laser-induced ultrafast demagnetization in ferromagnetic metals. Physical review letters, 85(14):3025–8, October 2000.

[94] G. P. Zhang, W. Hübner, Georgios Lefkidis, Yihua Bai, and Thomas F. George. Paradigm of the time-resolved magneto-optical Kerr effect for femtosecond magnetism. Nature Physics, 5(7):499–502, June 2009.

[95] Guoping Zhang, W. Hubner, E. Beaurepaire, and J.Y. Bigot. Laser-Induced Ultrafast Demagnetization: Femtomagnetism, a New Frontier? Spin Dynamics in Confined Magnetic Structures I, 290:245–289, 2002.

[96] V. Zhukov, E. Chulkov, and P. Echenique. GW+T theory of excited electron lifetimes in metals. Physical Review B, 72(15):1–14, October 2005.

[97] V. Zhukov, E. Chulkov, and P. Echenique. Lifetimes and inelastic mean free path of low-energy excited electrons in Fe, Ni, Pt, and Au: Ab initio GW+T calculations. Physical Review B, 73(12):125105, March 2006.

# Appendix A

## Magnetic Asymmetry Expansion

Here I will explain how the magnetic asymmetry term is expanded and simplified as a linear function of the real and imaginary part of the magneto optical constant [**?**]. The magnetic asymmetry is obtained in Chapter 2 as

$$A = \frac{I_+^p - I_-^p}{I_+^p + I_-^p} \cong 2Re\left[\frac{\sin 2\theta\ \epsilon_{xy}}{n^4\cos^2\theta - n^2 + \sin^2\theta}\right], \tag{A.1}$$

$$= 2Re\left[\frac{\sin 2\theta\ \epsilon_{xy}}{(n^2-1)(n^2+1)\cos^2\theta - (n^2-1)}\right]. \tag{A.2}$$

I plug $n = 1 - \delta + i\beta$ in and expand the denominator as

$$A = 2Re\left[\frac{\sin 2\theta\ \epsilon_{xy}}{1-(1+i\beta-\delta)^2 + (-1+(1+i\beta-\delta)^2)\,(1+(1+i\beta-\delta)^2)\cos^2\theta}\right] \tag{A.3}$$

$$= 2Re[\frac{\epsilon_{xy}\big(\beta^2-(-2+\delta)\delta+\big(\beta^4-6\beta^2(-1+\delta)^2+(-2+\delta)\delta(2+(-2+\delta)\delta)\big)\cos^2\theta\big)\sin 2\theta}{\big(\beta^2+(\delta-2)^2\big)\big(\beta^2+\delta^2\big)\big(1+2\big(\beta^2-2-(\delta-2)\delta\big)\cos^2\theta+(2+(\beta-2)\beta+(\delta-2)\delta)(2+\beta(2+\beta)+(\delta-2)\delta)\cos^4\theta\big)} \tag{A.4}$$

$$+i\frac{\epsilon_{xy}\beta(-1+\delta)\big(-8\big(\beta^2-(-2+\delta)\delta\big)\cos^3\theta\sin\theta+\sin 4\theta\big)}{\big(\beta^2+(\delta-2)^2\big)\big(\beta^2+\delta^2\big)\big(1+2\big(\beta^2-2-(\delta-2)\delta\big)\cos^2\theta+(2+(\beta-2)\beta+(\delta-2)\delta)(2+\beta(2+\beta)+(\delta-2)\delta)\cos^4\theta\big)}] \tag{A.5}$$

Now, I expand again both the denominator and numerator until the third order of $\delta$ or $\beta$. Then, the denominator becomes

$$= 4\left((1-2\cos^2\theta)^2(\delta^2+\beta^2) + (-12\cos^4\theta + 8\cos^2\theta - 1)(\delta^3 + \delta\beta^2)\right), \tag{A.6}$$

$$= 4\left((1-2\cos^2\theta)^2(\delta^2+\beta^2) + (1-2\cos^2\theta)(-1+6\cos^2\theta)(\delta^2+\beta^2)\delta\right); \tag{A.7}$$

and the numerator of the real part becomes

$$= (2\sin 2\theta - 4\cos^2\theta\sin 2\theta)\delta + (\sin 2\theta - 6\cos^2\theta\sin 2\theta)(\beta^2 - \delta^2), \tag{A.8}$$

$$= 2\sin 2\theta\left(1-2\cos^2\theta\right)\delta + \sin 2\theta(1-6\cos^2\theta)(\beta^2-\delta^2); \tag{A.9}$$

and finally the numerator of the imaginary part becomes

$$-\sin 4\theta\beta + (16\cos^2\theta\sin\theta + \sin 4\theta)\delta\beta \tag{A.10}$$

Then, I take the asymmetry term out of the Re function

$$\begin{aligned} A &\cong Re[\epsilon_{xy}]\frac{2\sin 2\theta\left(1-2\cos^2\theta\right)\delta + \sin 2\theta(1-6\cos^2\theta)(\beta^2-\delta^2)}{2\left((1-2\cos^2\theta)^2(\delta^2+\beta^2)+(1-2\cos^2\theta)(-1+6\cos^2\theta)(\delta^2+\beta^2)\delta\right)} && \text{(A.11)} \\ &- Im[\epsilon_{xy}]\frac{\left(-\sin 4\theta\beta + (16\cos^2\theta\sin\theta+\sin 4\theta)\delta\beta\right)}{2\left((1-2\cos^2\theta)^2(\delta^2+\beta^2)+(1-2\cos^2\theta)(-1+6\cos^2\theta)(\delta^2+\beta^2)\delta\right)}. && \text{(A.12)} \end{aligned}$$

To simplify more, I start to neglect the second order terms of $\delta$ and $\beta$ in the numerators and the third order terms in the denominator. I also replace $-\sin 4\theta$ by $-2\sin 2\theta(2\cos^2\theta-1)$, then the asymmetry reads

$$A \cong \frac{\sin 2\theta}{(1-2\cos^2\theta)}\left[\frac{\delta Re[\epsilon_{xy}]-\beta Im[\epsilon_{xy}]}{\delta^2+\beta^2}\right]. \tag{A.13}$$

When $\theta = 45°$, the above expansion is not valid. However, the original asymmetry term in Equation A.2 becomes very simple;

$$\begin{aligned} A &= 2Re\left[\frac{\sin 2\theta\ \epsilon_{xy}}{n^4\cos^2\theta - n^2 + \sin^2\theta}\right], && \text{(A.14)} \\ &= 4Re\left[\frac{\epsilon_{xy}}{(n^2-1)^2}\right], && \text{(A.15)} \\ &= 4Re\left[\frac{\epsilon_{xy}}{-4\beta^2+\beta^4+12\beta^2\delta+4\delta^2-6\beta^2\delta^2-4\delta^3+\delta^4+i\left(-4\beta^3-8\beta\delta+4\beta^3\delta+12\beta\delta^2-4\beta\delta^3\right)}\right], && \text{(A.16)} \\ &= 4Re[\epsilon_{xy}]\frac{\beta^4+(\delta-2)^2\delta^2-2\beta^2(2+3(\delta-2)\delta)}{\left(\beta^2+(-2+\delta)^2\right)^2\left(\beta^2+\delta^2\right)^2} + 4Im[\epsilon_{xy}]\frac{4\beta(\delta-1)\left(\beta^2-(\delta-2)\delta\right)}{\left(\beta^2+(\delta-2)^2\right)^2\left(\beta^2+\delta^2\right)^2}. && \text{(A.17)} \end{aligned}$$

Now it is time to neglect the fourth order of $\delta$ and $\beta$, as below

$$\begin{aligned} A &\cong 16Re[\epsilon_{xy}]\frac{\delta^2-\beta^2+3\beta^2\delta-\delta^3}{\left(\beta^2+(-2+\delta)^2\right)^2\left(\beta^2+\delta^2\right)^2} + 16Im[\epsilon_{xy}]\frac{2\delta\beta-3\beta\delta^2+\beta^3}{\left(\beta^2+(\delta-2)^2\right)^2\left(\beta^2+\delta^2\right)^2}, && \text{(A.18)} \\ &= Re[\epsilon_{xy}]\frac{\delta^2-\beta^2+3\beta^2\delta-\delta^3}{(1-2\delta)\left(\beta^2+\delta^2\right)^2} + Im[\epsilon_{xy}]\frac{2\delta\beta-3\beta\delta^2+\beta^3}{(1-2\delta)\left(\beta^2+\delta^2\right)^2} && \text{(A.19)} \end{aligned}$$

Equation A.15 looks more convenient for numeric calculations. If Re function is a problem for analytic calculations, A.19 becomes more useful. Now, I extend further by understanding the magnitudes of $\delta$ and $\beta$. At the absorption edge of elements, $\delta$ becomes much smaller than $\beta$. For

example, $\delta = 0.01$ and $\beta = 0.1$ for Ni around 67 eV which is M-edge. As a result, the asymmetry can be simplified even more,

$$A \cong \frac{-Re[\epsilon_{xy}]\beta^2 + Im[\epsilon_{xy}]\beta(2\delta + \beta^2)}{\beta^4} \cong -Re[\epsilon_{xy}]/\beta^2. \tag{A.20}$$

# Appendix B

## Multilayer T-MOKE Simulation and Experimental Spectrum

I presented the theoretical framework of T-MOKE spectra for magnetic multilayers in Chapter 2. Then, experimental results on these multilayer samples with different spacer layers were presented in Chapter 6 and 7. Here, I compare magnetic asymmetry calculations with nine experimental spectrum in Figure B. Multilayer composition for each sample is written above each graph and red and black curves show simulated and experimental results, respectively. Agreement between experiments and calculations is not impressive. There are four main factors that prevent having reliable simulation results:

- The refractive indices of materials in EUV energy region are not well studied. Main drawback is the lack of sources at this energy region. Synchrotron sources usually are interest of high energies rather than EUV and tabletop EUV sources are not well established for calibration and standardization of the refractive indices.

- The magneto-optical constants of magnetic materials are also not well studied and there is a lack of literature. Existing values of the magneto-optical constants depend on the used technique as well.

- The simulation results are strongly dependent on thicknesses of layers. Even small variations in thickness of seeding or capping layers result in large variations in magnetic asymmetries.

- Grating we fabricated on samples to use as a spectrometer is not a perfect laminar grat-

ing. It has some height variation and not sharp edges that affect the shape of magnetic asymmetry.

These sources of discrepancies prevent us to investigate further on the multilayer T-MOKE simulation but encourage us to understand more about pure-elemental demagnetization dynamics by extracting magneto-optical constants.

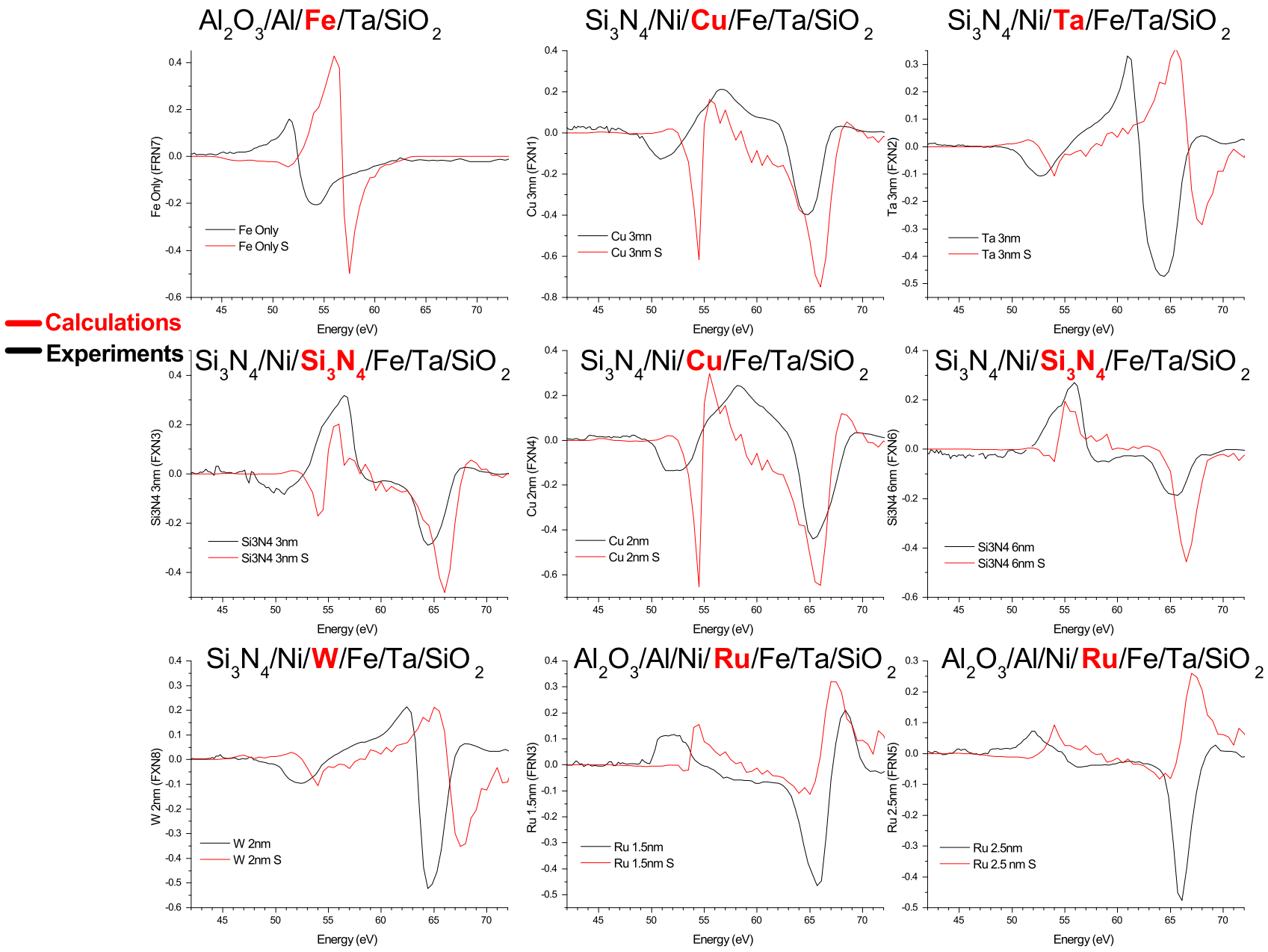


Figure B.1: Comparison between nine experimental spectrum and theoretical calculation of magnetic asymmetries as a function of energy. Agreement between the calculation and experiment is not great because of lack information about refractive indices.

# Appendix C

## Intensity vs Poynting's vector

Here I would like to clarify the discussion about the difference between Poynting's vector and intensity which mentioned in the Chapter 2. For semi infinite systems or very thick layers, both give same results but when there are many thin layers, the backward propagating waves give very different results. Because of this fact, one must be careful to use right method and software. This issue basically appeared in [26] which claimed about dominant effect of superdiffusive spin currents but made mistake in absorption calculations which makes big difference in the conclusion of the paper. Lets start with forward and backward propagating waves in $z$ direction.

$$E = E_+ e^{-ikz} + E_- e^{ikz}, \tag{C.1}$$

where $k$ is complex propagation vector and defined $k = \alpha - i\beta$. The intensity is given by

$$I = \frac{c\epsilon_0 n}{2}|E|^2, \tag{C.2}$$

where $c$ is the speed of light, $n$ is the refractive index of the medium. If we plug the electric field with the components of $k$, the intensity becomes,

$$I = \frac{c\epsilon_0 n}{2}(E_+ e^{-i\alpha z}e^{-\beta z} + E_- e^{i\alpha z}e^{\beta z})(E_+^* e^{i\alpha z}e^{-\beta z} + E_-^* e^{-i\alpha z}e^{\beta z}) \tag{C.3}$$

$$= \frac{c\epsilon_0 n}{2}\left[|E_+|^2 e^{-2\beta z} + |E_-|^2 e^{2\beta z} + E_+ E_-^* e^{-2i\alpha z} + E_- E_+^* e^{2i\alpha z}\right] \tag{C.4}$$

Now lets calculate the Poynting's vector for the above electric fields.

$$P = \frac{1}{2}Re[E \times H^*]; Hi\omega\mu = \frac{\partial}{\partial z}\hat{z} \times E. \tag{C.5}$$

After plugging the $H$ in the Equation C.5, $P$ becomes

$$P = \frac{1}{2}Re\left[(E_+e^{-ikz} + E_-e^{ikz}) \times \frac{k^*}{\omega\mu}(E_+^*e^{i\alpha z}e^{-\beta z} - E_-^*e^{-i\alpha z}e^{\beta z})\right] \quad \text{(C.6)}$$

$$= \frac{1}{2}Re\left[\frac{k^*}{\omega\mu}\left(|E_+|^2e^{-2\beta z} - |E_-|^2e^{2\beta z} - E_+E_-^*e^{-2i\alpha z} + E_-E_+^*e^{2i\alpha z}\right)\right] \quad \text{(C.7)}$$

As shown in the Equations C.4 and C.7, I emphasize the signs of the second and third terms by red color. This sign differences can result in very different values for the intensity and Poynting's vector.

Now, the crucial question is which one is right for multilayer systems. This confusion is coming from concept confusion. The intensity term is commonly used for simple cases such as thick layers to calculate absorptions, because Poynting's vector is more complicated and gives same results at the end. However, if there is a thin multilayer system with a backward propagating waves having comparable amplitudes to the forward propagating ones, the intensity term is not valid and Poynting's vector is right method for absorption calculations. Indeed, intensity is an overused term which one think that it always gives intensity profile in every system, but it does not.